

**3D PRINTING OF SOFT ELECTROMECHANICAL TRANSDUCERS AND
THEIR APPLICATION IN DEVELOPMENT OF PATIENT-SPECIFIC
ORGAN MODELS**

A DISSERTATION
SUBMITTED TO THE FACULTY OF THE
UNIVERSITY OF MINNESOTA
BY

Ghazaleh Haghiashtiani

IN PARTIAL FULFILLMENT OF THE REQUIREMENTS
FOR THE DEGREE OF
DOCTOR OF PHILOSOPHY

Adviser: Professor Michael C. McAlpine

January 2020

Acknowledgements

“Gratitude is the memory of the heart.”

– Jean-Baptiste Massieu

My heart has been filled with a load of memories over the past five years and I would like to take this opportunity to express my immense appreciation to the people who played a role in creating them.

First and foremost, I would like to thank my adviser, Prof. Michael McAlpine for his guidance, patience, and the vast opportunities he entrusted me with. I would have not been where I am today if it was not for his support and encouragement during the past years.

I would like to appreciate my examining committee, Prof. Rajesh Rajamani, Prof. Suhasa Kodandaramaiah, and Prof. Paul Iaizzo for the time they put in reviewing my dissertation and their insightful comments.

I am also very grateful to all the current and past postdocs and my peer graduate students at the McAlpine research group. Indeed, their support and company made this journey a much pleasant one.

I would like to express my appreciation to my academic and industrial collaborators and coauthors who I had the great opportunity of working with over the course of my PhD study: Dr. Kaiyan Qiu, Dr. Ed Habtour, Dr. Frank Gardea, Prof. Paul Iaizzo, Jorge Zhingre Sanchez, Dr. Priya Nair, and Dr. Sarah Ahlberg.

In addition, I would like to extend my gratitude to those who provided technical support or helpful suggestions during my experiments: Prof. S. J. Koester and S. K. Chaganti for assistance with dielectric characterizations, Dr. D. Giles from the UMN

Polymer Characterization Facility for mechanical and rheological tests support, C. Frethem for assistance with SEM carried out in the UMN Characterization Facility, Visible Heart[®] Laboratories of UMN for providing the tissue samples, and Prof. S. Kodandaramaiah and L. Ghanbari for their assistance and allowing me to fabricate my test fixtures using their equipment.

I would also like to acknowledge the funding support from the graduate school of the University of Minnesota (UMN 2017–18 Interdisciplinary Doctoral Fellowship and UMN 2018–19 Doctoral Dissertation Fellowship).

Finally, I would like to greatly thank my family and friends for their unconditional love, support, and motivation during my PhD journey.

Abstract

The ability to mimic nature and biological systems has revolutionized various fields and has inspired a plethora of scientific discoveries to solve human problems. Medicine is among the areas that has vastly benefited from bio-inspired innovations, such as the gecko-inspired adhesive and parasitic worm-inspired microneedle. Driven by the fact that medical errors are among the leading causes of death, several efforts have been focused to create phantoms that mimic the actual patients' organ with the main purpose of enhancing preoperational planning and surgical outcomes, as well as reducing the risk of intraoperative errors and postoperative complications.

Over the past decade, 3D printing technologies have played an important role in fabrication of patient-specific organ phantoms, however, despite being anatomically correct, these 3D printed organ models mostly lack the precise mimicry of the sense and mechanical properties of the biological tissue of interest. In addition, they lack advanced functionalities, such as tactile sensing, to provide quantitative feedback during organ handling which can be a valuable metric in different surgical interventions or for training purposes.

This dissertation aims at addressing these two limitations by conducting an investigation at the intersection of soft biomimicking electroactive, and tissue-like material systems and electromechanical transducer design coupled with multi-material, extrusion-based 3D printing process, for primary applications in development of smart, patient-specific organ models. Specifically, the design and development of (i) a tunable silicone-based material system with tissue-like mechanical properties compatible with direct ink

writing 3D printing process, (ii) soft electromechanical actuators and sensors based on the biomimicking hydrogel-elastomer hybrid material system, and (iii) coalescence of these concepts for fabrication of patient-specific organ models with integrated functionalities were presented.

It is envisioned that these organ models can augment the current practices in a gamut of medical applications, including preoperative planning, clinical training, patient education, and development of next-generation medical devices with the end goal of enhancing surgical outcomes, reducing medical errors, and improving patient safety. In addition, on a long-term basis, the outcomes of this work could contribute to the incorporation of cell-seeded structures into the organ models, thus setting the stage for development of dynamic bionic organs.

Table of Contents

| | |
|--|-------------|
| Acknowledgements | i |
| Abstract | iii |
| List of Tables | vii |
| List of Figures | viii |
| Chapter 1: Introduction | 1 |
| 1.1. Motivation and Objectives | 2 |
| 1.2. Background | 4 |
| 1.2.1. 3D Printed Organ Models Using Commercial Materials | 4 |
| 1.2.1.1. 3D Printed Organ Models Using Rigid-Plastic Materials | 6 |
| 1.2.1.2. 3D Printed Organ Models Using Elastomeric (Rubber-Like) Materials | 11 |
| 1.2.1.3. 3D Printed Organ Models Using Powder-Based Materials | 15 |
| 1.2.2. Prior Work on Organ Models with Integrated Functionalities | 16 |
| 1.2.3. Dielectric Elastomers for Soft Electromechanical Devices | 18 |
| 1.3. Dissertation Overview | 21 |
| Chapter 2: Development of Tissue-Mimicking Inks for 3D Printing Patient-Specific Organ Models | 23 |
| 2.1. Introduction | 24 |
| 2.2. Development of Tunable 3D Printable Polymeric Materials with Patient-Specific Physical Properties | 27 |
| 2.3. Proof of Concept Demonstration: 3D Printed Patient-Specific Prostate Model..... | 32 |
| 2.4. Conclusion..... | 37 |
| Chapter 3: 3D Printing Soft Electromechanical Transducers | 39 |
| 3.1. Introduction | 40 |
| 3.2. Mechanism of Actuation in DEAs Based on Ionic Hydrogel-Elastomer Hybrids | 42 |
| 3.3. Optimization of Ink Formulations for 3D Printing | 44 |
| 3.4. Materials Characterization | 46 |
| 3.5. Overcoming Materials Incompatibilities and Device Fabrication | 49 |
| 3.6. DEA Performance Analytical and Finite Element Modeling | 52 |
| 3.7. DEA Performance Experimental Characterization..... | 56 |
| 3.8. Ionic Hydrogel-Elastomer Hybrids as Sensors..... | 61 |
| 3.9. Proof of Concept Demonstration: Integrated DE Sensor on 3D Printed Prostate Model | 64 |
| 3.10. Development of Planar Sensor Array | 67 |
| 3.11. Conclusion..... | 72 |
| Chapter 4: Functional 3D Printed Aortic Root Models with Internal Sensors for Minimally Invasive Applications | 74 |
| 4.1. Introduction | 75 |
| 4.2. Material Selection and Model Fabrication | 78 |
| 4.3. Model Fidelity Analyses Compared to Patient's Data | 82 |
| 4.4. <i>In Vitro</i> Hemodynamic Studies | 84 |
| 4.5. Visualization of Applied Pressures via Internally Integrated Sensor Arrays | 90 |
| 4.6. Conclusion..... | 95 |
| Chapter 5: Conclusions and Future Directions | 98 |

| | | |
|--|--|------------|
| 5.1. | Conclusions | 99 |
| 5.2. | Future Directions | 102 |
| Bibliography | | 105 |
| Appendix A: Supplementary Information for Chapter 2 | | 122 |
| A.1. | 3D Printing Materials Formulation and Preparation | 123 |
| A.2. | Mechanical Characterization of the Customized Polymeric Materials | 123 |
| A.3. | Sol-Gel and Stability Tests of the Customized Polymeric Materials in Hexane, Glycerol-Water, and Air | 123 |
| A.4. | Rheological Characterization of the Customized Polymeric Inks | 124 |
| A.5. | Mechanical Characterization of Prostate Tissue and Customized Polymeric Inks | 125 |
| A.6. | 3D Printing of Patient-Specific Prostate Model | 125 |
| A.7. | 3D Registration for Investigating the Anatomical Fidelity | 126 |
| A.8. | Endoscopy and Suturing Practices on the 3D Printed Prostate Model | 127 |
| Appendix B: Supplementary Information for Chapter 3 | | 128 |
| B.1. | Materials Preparation for 3D Printing | 129 |
| B.2. | 3D Printing of DEAs | 130 |
| B.3. | Materials Mechanical Characterization | 131 |
| B.4. | Materials Rheological Characterization | 131 |
| B.5. | Shear Rate Calculation During Extrusion | 132 |
| B.6. | Materials Electrical Characterization | 132 |
| B.7. | DEA Testing | 133 |
| B.8. | DEA Actuation Video Analysis | 134 |
| B.9. | Analytical Model for DEA | 135 |
| B.10. | Finite Element Method (FEM) for Characterization of DEA Performance | 142 |
| | References | 144 |
| Appendix C: Supplementary Information for Chapter 4 | | 146 |
| C.1. | 3D Printing Materials Formulation and Preparation | 147 |
| C.2. | Preparation and Characterization of Tissue and Polymer Samples | 147 |
| C.3. | Fourier Transform Infrared Spectroscopy (FTIR) | 149 |
| C.4. | Processing of STL Models | 149 |
| C.5. | 3D Printing of Aortic Root Models | 150 |
| C.6. | Model Fidelity Analysis | 151 |
| C.7. | Frame Analysis of the Implanted Valve in the 3D Printed Aortic Root Model | 151 |
| C.8. | Calculation of Parameters for <i>In Vitro</i> Hemodynamic Testing | 152 |
| C.9. | Preparation of Models with Internally Integrated Sensor Array | 153 |
| C.10. | Calibration of the Sensor Array | 154 |
| C.11. | Testing of Models with Internally Integrated Sensor Array | 156 |

List of Tables

| | |
|--|-----|
| Table B.1. Printing parameters for different inks used in fabrication of DEAs..... | 131 |
| Table B.2. FEM and analytical model parameters used in modeling DEA performance | 144 |
| Table C.1. Estimated elastic modulus of examples of tissue and custom-formulated polymer samples at different strains and comparison with the reported values in literature | 148 |
| Table C.2. Calibration equations for the 9 sensing elements of the sensor array | 155 |

List of Figures

| | |
|--|----|
| Figure 1.1. Examples of 3D printed organ models using rigid-plastic materials with applications in cardiology and urology..... | 9 |
| Figure 1.2. Examples of 3D printed organ models using rigid-plastic materials with applications in neurology and hepatology | 11 |
| Figure 1.3. Examples of 3D printed organ models using elastomeric (rubber-like) materials with applications in cardiology | 13 |
| Figure 1.4. Examples of 3D printed organ models using elastomeric (rubber-like) materials with applications in urology, neurology and pulmonology..... | 15 |
| Figure 1.5. Examples of 3D printed organ models using powder-based materials with applications in cardiology and neurology..... | 16 |
| Figure 1.6. Organ models or simulators with integrated functions..... | 18 |
| Figure 1.7. Principle of operation of a dielectric elastomer actuator | 19 |
| | |
| Figure 2.1. Design and development of customized polymeric materials | 28 |
| Figure 2.2. Sol-gel fraction analysis of the customized polymeric materials in hexane.. | 29 |
| Figure 2.3. Stability of the customized polymeric materials in different test environments | 30 |
| Figure 2.4. Rheological characterization of custom-formulated polymeric inks..... | 31 |
| Figure 2.5. Comparison of Young’s modulus of biological tissues with different materials including customized polymeric ink, tissue-mimicking materials, commercial 3D printing materials | 32 |
| Figure 2.6. Comparison of mechanical properties of the custom-formulated polymeric materials with prostate tissue specimens | 34 |
| Figure 2.7. 3D printing of patient-specific prostate model..... | 35 |
| Figure 2.8. Anatomical fidelity analysis of the 3D printed model in comparison with patient’s prostate | 36 |
| Figure 2.9. Examples of potential application of the tissue-mimicking prostate model in surgical rehearsal and training | 37 |
| | |
| Figure 3.1. Mechanism of actuation in DEAs based on ionic hydrogel-elastomer hybrids | 43 |
| Figure 3.2. DEA structure and components in unimorph configuration..... | 43 |
| Figure 3.3. Materials characterization..... | 48 |
| Figure 3.4. Surface treatment and 3D printing of ionic hydrogel on underlying silicone-based surface | 50 |
| Figure 3.5. Step by step fabrication process and 3D printing of the unimorph DEA. | 51 |
| Figure 3.6. Final 3D printed DEA..... | 52 |
| Figure 3.7. Characterization of device actuation performance in response to applied ramp-up voltage input | 57 |
| Figure 3.8. Characterization of the time- and frequency-dependent performance of the DEAs..... | 59 |

| | |
|---|-----|
| Figure 3.9. Effect of changing the DE thickness on device actuation performance | 60 |
| Figure 3.10. Characterization of DEA performance in response to applied tip masses .. | 61 |
| Figure 3.11. Structure and fabrication process of the 3D printed soft capacitive tactile sensor based on ionic hydrogel-elastomer hybrids | 63 |
| Figure 3.12. Characterization of the 3D printed capacitive sensor in response to applied pressures..... | 64 |
| Figure 3.13. Proof-of-concept demonstrations with integration of the soft capacitive sensor on the outer surface of the 3D printed prostate model..... | 66 |
| Figure 3.14. Proof-of-concept demonstrations with integration of the soft capacitive sensor on the urethra surface of the 3D printed prostate model | 67 |
| Figure 3.15. Design and structure of the sensor array | 69 |
| Figure 3.16. Calibration of the sensor array..... | 70 |
| Figure 3.17. Investigating the crosstalk between adjacent elements in the sensor array. | 71 |
| Figure 3.18. Object detection experiments with the 3 × 3 sensor array | 72 |
| | |
| Figure 4.1. Schematic of the heart and its conduction pathway with implanted TAVR prosthesis in the aortic root region | 76 |
| Figure 4.2. Process for generating the G-Code for 3D printing of the patient-specific aortic root model | 79 |
| Figure 4.3. Different components of the aortic root model | 79 |
| Figure 4.4. Stress-strain plots of custom-formulated polymeric materials and tissue specimens..... | 81 |
| Figure 4.5. FTIR plot of the calcification material | 81 |
| Figure 4.6. Anatomical fidelity analysis of the 3D printed aortic root model with respect to patient’s data..... | 82 |
| Figure 4.7. Analysis of the deflection of the valve’s frame implanted in the 3D printed model and comparison with patient’s postoperative data..... | 83 |
| Figure 4.8. Models used for <i>in vitro</i> hemodynamic studies..... | 85 |
| Figure 4.9. Test setup for <i>in vitro</i> hemodynamic studies..... | 86 |
| Figure 4.10. Comparison of compliance of models in set 1 and set 2 (without and with calcification, respectively) | 88 |
| Figure 4.11. Comparison of pressure gradient between left ventricle and aorta in models with and without calcification..... | 89 |
| Figure 4.12. Detection of potential paravalvular leak sites in the 3D printed aortic root model with implanted valve and corresponding color Doppler echocardiographs..... | 90 |
| Figure 4.13. Step-by-step 3D printing of the aortic root model with internally integrated sensor array | 91 |
| Figure 4.14. Final 3D printed aortic root model with internal sensor array | 92 |
| Figure 4.15. Calibration of the sensor array..... | 93 |
| Figure 4.16. Visualization of applied pressures for different cases of valve implantation height..... | 94 |
| Figure 4.17. Visualization of applied pressures for different cases of valve sizing | 95 |
| | |
| Figure B.1. Circuit setup for high voltage application and testing of DEAs. | 134 |

Figure B.2. General schematic of the beam-like device and notations used in the modeling and cross section of the device 137

Figure C.1. Implantation of the prosthetic valve in the 3D printed aortic root model .. 152

Figure C.2. Heatmaps of normalized capacitance changes for different cases of valve implantation height and sizing 157

CHAPTER 1[†]

Introduction

[†] The work reported in this chapter is partly based on the following original publication: K. Qiu, G. Haghiashtiani, & M. C. McAlpine, 3D Printed Organ Models for Surgical Applications. *Annual Review of Analytical Chemistry* 11, 287-306 (2018).

1.1. Motivation and Objectives

The use of anatomical models and simulators in medicine traces back to centuries ago when clay and stone models were utilized to replicate disease conditions (1, 2). Over the years, the emphasis on decreasing patient mortality, surgical complications and operation time – accompanied by increased surgical training outside of operating rooms – have driven the evolution of different techniques for surgical planning and training (3, 4). Despite these efforts, one recent study has suggested that “medical errors” lead to a mean death rate of more than 250,000 patients each year, which would result in a rank as the third most prominent cause of death in the United States after heart disease and cancer (5). Indeed, over 4,000 incidents of surgical “never events” (events that should never happen) are estimated to occur annually in the United States alone (6). Hence, effective clinical training and preoperative planning could play a vital role in mitigating these incidents.

Conventionally, different imaging techniques, including computed tomography (CT) and magnetic resonance imaging (MRI) have been used to extract the required information regarding patients’ anatomical structure for diagnosis and preoperational planning. However, a precise recognition of orientation and dimension may be obscured in these 2D images, which increases the dependency on surgeon’s experience and skills, hence increasing the risk of the misinterpretation, intraoperative errors and on-site improvisation (7). Advances in imaging technology have facilitated the generation of virtual 3D representations of anatomical structures from the aforementioned methods. Although these 3D images have significantly improved the spatial visualization and comprehension of interrelationships of anatomical structures, they are intangible and cannot be used to

effectively adjust the application of surgical tools in preoperative planning (8). In addition, the virtual 3D images may suffer from the potential loss of orientation and misinterpretation of object dimensions due to zoom effects (7). Developing physical organ models with anatomically accurate features could significantly improve the comprehension of surgical target areas in diagnosis, procedural planning, clinical training, and even can be used for educating patients. In recent years, rapid prototyping methods, such as 3D printing, coupled with 3D imaging techniques have made the production of such vital models feasible.

Today, the application of 3D printing goes well beyond the conventional rapid prototyping of parts for design optimization. In 2016, medical applications comprised approximately 15.1% of the 3D printing market, making it the third largest market share after consumer products and motor vehicles, and it has been estimated that this number will increase to 16.8% by 2021 (9). Specifically, several efforts have been focused on utilizing commercial 3D printers to create customized organ models based on patients' anatomical data that were used for diagnosis and preoperative planning (8), patient education on their medical condition and treatment plan (10), clinical training (11), and new surgical instrument and medical device development (12).

Although these 3D printed organ models have been useful for surgical planning and rehearsal, their efficacy for applications as advanced surgical aids suffers from two main issues:

1. Despite representing the correct anatomy, these 3D printed organ models are often incapable of precisely mimicking the physical properties of organ tissue (13), including

tactile sensation and mechanical properties. This issue limits their effectiveness in preoperative planning, rehearsal with surgical tools, and other tasks such as pressing, suturing, cutting, clipping, and dissecting (13, 14). This also hampers the ability of 3D printed organ models to accurately predict and replicate organ physical behavior during surgical handling.

2. These 3D printed organ models lack the functionality to provide quantitative feedback resulting from organ and tissue handling. This function can be an important add-on for surgical trainers or simulators, to aid medical professionals in assessing and controlling their performed tasks quantitatively, such as the amount of pressure applied to the organs via diagnostic and surgical tools.

The integration of quantitative feedback, along with the use of custom-formulated materials with mechanical properties close to those of biological tissues could significantly enhance the effectiveness of organ models for the discussed purposes. To this end, the objective of this dissertation is to combine the recent advancements of 3D printing techniques with developments of soft, biomimicking electromechanical transducers and tissue-mimicking materials, to investigate the fabrication of organ models with integrated functionalities.

1.2. Background

1.2.1. 3D Printed Organ Models Using Commercial Materials

The process of 3D printing patient-specific organ models starts with obtaining the anatomical information of the patient's organ of interest via different imaging modalities, such as CT or MRI scans. These images are normally in a Digital Imaging and

Communications in Medicine (DICOM) format, which cannot be directly utilized by 3D printers. Therefore, the acquired images need to be post-processed to first identify the region of interest of the organ via proper segmentation of its volumetric dataset (using software such as Vitrea[®] and Mimics), and then generate a STereoLithography (.STL) file for the 3D printing process (15, 16). In some cases, this STL file needs to be further refined using computer aided design (CAD) software packages to rectify the imperfections in the STL model (such as closing the gaps between segments of the model) and optimize its 3D printing (15, 16). The final STL model is then sliced into horizontal layers using 3D slicing software (such as Slic3r) to generate the G-code, which defines the printing pathways to create the 3D printed organ model.

In 3D printing processes, parts are manifested layer-by-layer from a 3D representation of the object in a CAD program. Since the emergence of stereolithography (SLA) in the 1980s as one of the early 3D printing processes, various techniques have been developed to broaden the application of this technology (17). These 3D printing techniques can be classified into four main categories (18): 1. Processes based on photopolymerization of liquid polymers or epoxy resins, either by focusing a light source in a predefined pattern on a bath of the liquid photosensitive material (such as stereolithography (SLA), direct light processing (DLP), two-photon polymerization (TPP), and continuous liquid interface production (CLIP)), or by jetting droplets of the liquid photopolymer followed by curing via an ultraviolet (UV) light source (material jetting or PolyJet); 2. Processes that involve extruding a thermoplastic filament (fused deposition modeling (FDM)) or viscoelastic materials (direct write assembly (DWA), direct ink writing (DIW) or robocasting); 3.

Processes that create a 3D object from powdered materials via laser sintering, fusion, or use of a binder component, such as selective laser sintering (SLS), selective laser melting (SLM), electron beam melting (EBM), direct metal laser sintering (DMLS), and binder jetting (powder bed-based inkjet 3D printing); and 4. Processes that work based on laminating and layering sheet materials, such as laminated object manufacturing (LOM), and selective deposition lamination (SDL).

Most of the reported 3D printed organ models are fabricated based on FDM, PolyJet, SLA, or inkjet 3D printing technologies, and by using commercially available materials (13, 16, 19-22), which can be broadly categorized into rigid-plastic materials, elastomeric (rubber-like) materials, and powder-based materials such as starch/cellulose and plaster.

In the following sections, the use of 3D printing for creating patient-specific organ models with an emphasis on the material systems that can be used in the fabrication process have been discussed. For this purpose, the use of commercial materials, including rigid-plastic, elastomeric (rubber-like), and powder-based materials for 3D printing organ models and their efficacy in different fields, including but not limited to cardiology, neurology, urology, pulmonology and hepatology, have been discussed.

1.2.1.1. 3D Printed Organ Models Using Rigid-Plastic Materials

The early 3D printed organ models were mainly fabricated using a limited selection of commercial rigid-plastics, primarily involving acrylonitrile butadiene styrene (ABS) and polylactic acid (PLA) thermoplastic filaments for FDM printing, or rigid photopolymers and resins for PolyJet technology (such as the Vero™ family of photopolymers from Stratasys). Such models are still popular due to their accuracy in representing patients'

anatomy at a relatively low cost (21). The term rigid-plastic is used here for polymers that have high crosslinking densities and/or high molecular weights with glass transition temperatures (T_g) above room temperature. These are mechanically rigid materials with high-impact strength and hardness (23). The Young's moduli for most rigid-plastic materials are close to or within the GPa range, i.e., at least three orders of magnitude higher than the modulus of soft organ tissue. This discrepancy in the materials' elastic properties relative to the organs themselves limits the direct application and realism of these models for surgical rehearsal (14). Even so, these organ models have demonstrated utility in a variety of medical fields, including cardiology (24-26), urology (10, 27-29), neurology (14, 30, 31), and hepatology (32, 33).

In the field of cardiology, Farooqi *et al.* (24, 25), 3D printed cardiac models (Figures 1.1 (a, b)) via an FDM process using ABS filaments. These models accurately replicated the detailed anatomy of a healthy heart (Figure 1.1 (a)) and cases with different congenital heart disease, such as dextro-Transposition of the great arteries after performing the Mustard procedure for defect correction (Figure 1.1 (b)). Specifically, it was speculated that the latter model (Figure 1.1 (b)) could have been utilized for optimizing the position of the inflow cannula in the ventricular assist device implantation procedure required for the patient's case (25). In another example, Schievano *et al.* (26) created 3D printed models for the right ventricular outflow tract and pulmonary trunk using a thermoplastic polyester resin (P1500 Polyester, Stratasys) via an FDM process. Due to the anatomical accuracy, the models were used to assist two cardiologists participating in the study for more accurate selection of patients for percutaneous pulmonary valve implantation. It was shown that by

using the 3D printed models, the accuracy of the selections made by the two cardiologists increased by 8% and 25%, compared to only using MRI scans to make the decisions (26).

In the field of urology, Wake *et al.* (27) and Kusaka *et al.* (28) created 3D printed prostate (Figure 1.1 (c)) and kidney models (Figure 1.1 (d)), respectively, via the PolyJet process using the rigid Vero™ family of photopolymers (Stratasys). These commercial materials are available in a variety of colors, including clear, magenta and cyan, and can be used to distinguish different printed sections and anatomical details of the organ models (21, 27, 28). The 3D printed models in both works were found to be helpful for recognizing the anatomical features of the organs in the corresponding operations. Komai *et al.* (29) also fabricated a patient-specific, full-scale 3D printed kidney model via the PolyJet process. The model included a removable tumor combined with its margin, which enabled both the surgeons as well as the patients to envision the kidney before and after tumor resection. It was further confirmed during surgery that the model could be used to help surgeons perform minimally invasive off-clamp partial nephrectomy, because the 3D printed model provided the surgeons with tactile sensation and aided in effectively determining the incision line and angle. In addition, Bernhard *et al.* (10), created a 3D model of kidney and tumor anatomies via the PolyJet process for patient education. Specifically, a survey that was conducted in the work indicated that after showing the organ models to the patients, their understanding in the categories of kidney physiology, kidney anatomy, tumor characteristics, and the planned surgical procedure increased by 16.7%, 50%, 39.3%, and 44.6%, respectively.

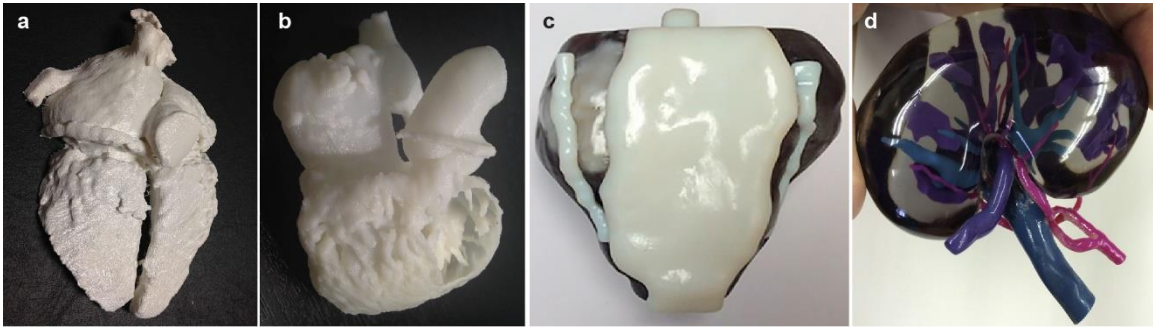


Figure 1.1. Examples of 3D printed organ models using rigid-plastic materials with applications in cardiology and urology. (a) A 3D printed cardiac model without congenital disease, and (b) a 3D printed cardiac model after the Mustard procedure for correcting the congenital heart defect using a commercial ABS thermoplastic filament for printing. Adapted from references (24, 25), respectively. (c) A 3D printed prostate model, and (d) a 3D printed kidney model using the Vero™ family of polymers. Adapted from references (27, 28), respectively.

For neurological applications, Anderson *et al.* (30) 3D printed hollow intracranial aneurysm models (Figure 1.2 (a)) with rigid walls using an FDM process and PLA filaments. The models could accurately replicate the patients' aneurysm anatomy in a digital subtraction angiography (DSA) image (Figure 1.2 (b)), and therefore they could be used for surgical aid applications as well as for MRI flow phantoms and computational fluid dynamic studies based on rigid models for simulation of aneurysm hemodynamics (30). In another case, Erbano *et al.* (31) created 3D intracranial aneurysm models using another rigid photosensitive liquid resin, FullCure 720 (Stratasys), via the PolyJet process. The models replicated the accurate location, size, and shape of the intracranial aneurysms, which were identical to the ones measured by DSA. It was concluded that these models can facilitate the selection of surgical procedures and tools (such as aneurysm clips), thus yielding better operational planning for intracranial aneurysms. Wurm *et al.* (14) initially fabricated rigid cerebral aneurysm models via 3D printing of a photosensitive polymeric liquid-plastic solution using the SLA process. The 3D printed models were applied for diagnosis, surgical planning, simulation, training of novice neurosurgeons, and informing

patients. All neurosurgeons in the study stated that the 3D printed models were helpful in establishing better comprehension of the cerebrovascular anatomy, as well as the configuration, orientation, and dimension of aneurysms. However, the models were found to be less beneficial for clipping and dissecting exercises due to the rigid nature of the material used for 3D printing.

In the hepatology field, Zein *et al.* (32) created 3D printed synthetic liver models from living donors and their respective recipients using the PolyJet process. The 3D printed liver models from donor and recipient accurately mimicked their corresponding native livers (Figures 1.2 (c, d)) and were used for anatomical and geometrical evaluations before, during, and after the surgical procedures. The models were found to facilitate the comprehension of the spatial relationship between the vascular and biliary anatomies, as well as enabling hands-on surgical planning and training with the purpose of reducing intraoperative complications. Souzaki *et al.* (33) also 3D printed a model of a patient's liver with a malignant tumor using the PolyJet process. The model was used for viewing the anatomies and the relative positions of the portal vein, hepatic vein, and tumor, which were identical to the anatomy of the patient's liver. The surgeons utilized the model to evaluate the surgical procedure and determine the resection line for removing the tumor before the operation. The surgical outcome indicated that the tumor was entirely removed and the surgical margin was negative.



Figure 1.2. Examples of 3D printed organ models using rigid-plastic materials with applications in neurology and hepatology. (a) A 3D printed intracranial aneurysm model using polylactic acid as the rigid walls, and (b) its corresponding digital subtraction angiography image for patient aneurysm. Adapted from reference (30). (c) A 3D printed liver model, and (d) a right liver lobe model using PolyJet process and their corresponding actual organs. Adapted from reference (32).

1.2.1.2. 3D Printed Organ Models Using Elastomeric (Rubber-Like) Materials

With the advancement of 3D printing technologies, the palette of materials that can be used in these processes evolved to broaden the applications. This includes the possibility of 3D printing elastomeric (rubber-like) and flexible materials, beyond conventional rigid plastics. Some examples of such materials include the Tango™ family (Stratasys) of photopolymers for PolyJet printing, or thermoplastic elastomer (TPE) filaments such as NinjaFlex® (NinjaTek), SemiFlex™ (NinjaTek), and PolyFlex™ (Polymaker) for FDM printing. In contrast to TPE filaments with elastic properties, rubbers are thermoset polymers with network structures. These thermoset network polymers are not suitable for FDM printing because the polymer chain motion is greatly restricted by a high degree of crosslinking after heating, such that they cannot be remanufactured after their initial heat forming (23). 3D printable elastomeric (rubber-like) materials have low Young's moduli and good flexibility compared with other 3D printing materials (34). The elasticity and flexibility in these materials are due to the reconfiguration of long chains of the polymers and covalent crosslinks. 3D printed organ models fabricated by such materials provide

tactile sensation closer to the actual organ, compared to rigid-plastic materials. Therefore, they allow surgeons to perform different rehearsal operations on them, such as cutting and pressing. Some examples for application of such models in the fields of cardiology (35-38), urology (27, 28), neurology (39-41) and pulmonology (42, 43) are discussed below.

For cardiac applications, Yoo *et al.* (35) created cardiac models with congenital heart disease (Figure 1.3 (a)) using the TangoPlus™ photopolymer via the PolyJet process. The models were used by a total of 81 professionals or trainees for performing the required surgical procedures (Figure 1.3 (a)). Although differences in elasticity and consistency between the model material and human myocardium were noticed by most of the respondents, 88% of the responses indicated that the quality of the models was acceptable for surgical practice, while 12% found it manageable. In another example, Kiraly *et al.* (36) fabricated a scaled-up (3×), flexible, hollow heart model with a congenital defect (Figure 1.3 (b, c)). The model was used to guide the surgical approach of arch repair at each step of the operation (Figure 1.3 (b)). The patient's operation (Figure 1.3 (c)) was performed following preoperative rehearsal on the 3D printed model (Figure 1.3 (b)), which resulted in increasing the patient's safety, and ultimately, the likelihood of a positive operation outcome. Shiraishi *et al.* (37) also created a 3D heart model using a stereolithographic biomodelling technique and a photosensitive rubber-like urethane with tensile modulus of 0.01 GPa. The model offered detailed anatomical features and allowed surgeons to cut and suture in preoperative practice due to its rubber-like properties. Furthermore, Yang *et al.* (38) printed a heart model via the PolyJet process and by using the Tango™ family of photopolymers with different colors to distinguish different parts in the heart model. It was

stated that the model not only could be utilized for better visualization of the geometry, but it could also be disassembled for surgical practice, such as a rehearsal for the case of an extended septal myectomy performed in the study.

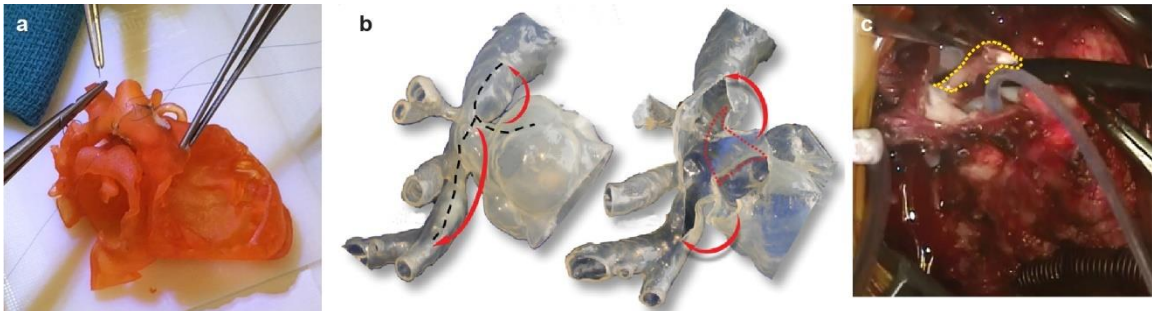


Figure 1.3. Examples of 3D printed organ models using elastomeric (rubber-like) materials with applications in cardiology. (a) A 3D printed cardiac model with a congenital defect using the TangoPlus™ photopolymer for hands-on surgical training. Adapted from reference (35). (b) A 3D printed hollow aortic arch model. The black dotted lines, red dotted lines, and red arrows represent the proposed incision lines, the internal obstructive ridge to be resected after opening the model, and arch augmentation, respectively. Adapted from reference (36). (c) The obstructive ridge is resected (yellow dotted line) in real operation, guided via simulation on the corresponding 3D printed model in (b). Adapted from Reference (36).

In the field of urology, Wake *et al.* (27) 3D printed a patient-specific, cancerous kidney model with accurate anatomy for applications in urological oncology (Figure 1.4 (a)) using a transparent, flexible material (HeartPrint™ Flex, Materialise) as the main cortex, and the Vero™ family of rigid photopolymers in different colors as the remaining structures. Such kidney models with tumor sections allowed surgeons to evaluate the complexity of the tumor and its positional relationship with respect to other parts of the organ, thus facilitating the operational planning for partial nephrectomy or ablative therapy. In a real surgical case, the model was used to assist surgeons in the selection of an approach for partial nephrectomy, as well as a resection guidance during the surgery. Kusaka *et al.* (28) also 3D printed a kidney graft and pelvic cavity model via the PolyJet printing process using mainly the Tango™ family of photopolymers with different colors. The model was

successfully applied for preoperational planning and accurate simulation of the surgical procedure for kidney transplantation.

For neurological applications, Kimura *et al.* (39) and Khan *et al.* (40) developed a hollow cerebral aneurysm and a cerebral vasculature physical model by using the Tango™ family of photopolymers in the PolyJet printing process. In Kimura's work, various types of aneurysm clips were applied on the 3D hollow models (Figure 1.4 (b)) under the operative microscope to optimize the clip placement (39). In Khan's work, the 3D printed cerebral vasculature physical model accurately represented the patient's aneurysm (40). The participating neurosurgical trainees in the study found the models beneficial for better comprehension of the anatomical features of the patients' aneurysm and the corresponding vascular structures, as well as for the determination of proper surgical approach and tools (40). In addition, Wurm *et al.* (41) used the PolyJet process to 3D print an aneurysm model. This model was used as a replaceable part for several clipping exercises in microsurgical simulation due to its flexible nature. The model could help neurosurgeons and trainees hone their skills in the clipping approach, clip selection and its placement.

In the pulmonology field, Bustamante *et al.* (42) fabricated 3D printed tracheobronchial tree models (Figure 1.4 (c)) using the PolyJet process. The models were examined with a flexible fiberoptic bronchoscope, and the obtained image (Figure 1.4 (c) inset) from the model was found to be similar with the actual views of the organ during lung isolation. The models were expected to aid medical professionals to overcome issues in achieving lung isolation via enhanced familiarity with endoscopic bronchial anatomy. In addition, Kurenov *et al.* (43) 3D printed models of human pulmonary arteries using the

TangoPlus™ photopolymer via the PolyJet process. In terms of anatomy, the models were sufficiently accurate for clinical purposes. In the study, the models were used to design a catheter for regional lung chemotherapy. It was perceived that the applications could be expanded into other areas of clinical care and research for thoracic surgery, such as complex thoracoscopic surgery lobectomies.

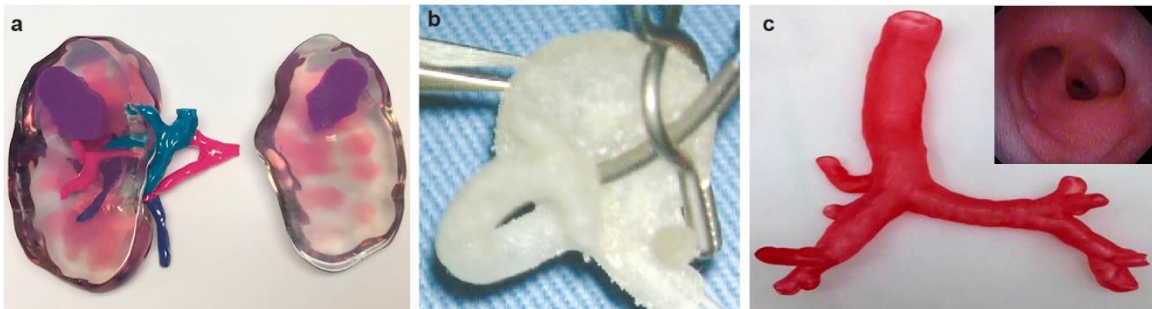


Figure 1.4. Examples of 3D printed organ models using elastomeric (rubber-like) materials with applications in urology, neurology and pulmonology. (a) A 3D printed kidney model using flexible material as the kidney's main cortex showing the relative position of the renal tumor with respect to the renal artery, vein, and collecting system. Adapted from reference (27). (b) A 3D printed left middle cerebral bifurcation aneurysm for surgical clipping rehearsal. Adapted from reference (39). (c) A 3D printed tracheobronchial tree model. Inset: Fiberoptic view of the 3D printed tracheobronchial tree model through the bronchus intermedius. Adapted from reference (42).

1.2.1.3. 3D Printed Organ Models Using Powder-Based Materials

Powder-based materials such as starch, cellulose and plaster powder, solidified with binding materials via inkjet 3D printing, have also been evaluated for fabrication of different organ models for surgical applications. Despite the mismatch of their mechanical properties with real organs, such models provide accurate anatomical details with convenient, low-cost fabrication. In the field of cardiology, Schmauss *et al.* (44) demonstrated an example for creating 3D printed cardiac models (Figure 1.5 (a)) using starch/cellulose powder (zp 15e, Z Corporation), a polymer as the binder (zb 60, Z Corporation) and an elastomeric urethane resin (Por-A-Mold 2030, EnvironMolds LLC.) for further infiltration. The participating surgeons could detect the bypass grafts and their

position with respect to the sternum from the model shown in Figure 1.5 (a). The sterilized model was further used in the operating room for guiding the intraoperative procedures for reopening the sternum (44). In another example, Mottl-Link *et al.* (7) 3D printed a cardiac model (Figure 1.5 (b)) using plaster-based powder with a binding material. The final model allowed surgeons to obtain intracardiac views that are difficult to achieve during the actual operation. Additionally, the plaster materials were used in neurology applications. Kondo *et al.* (45) and Oishi *et al.* (46) developed 3D printed models of a skull base and intracranial tumors using plaster materials. Such models (Figure 1.5 (c)) can provide a better visualization of the anatomy and size of the organ, tumor and their positional relationships. The models were further used to provide realistic surgical practice and sensation via insertion of surgical instruments under microscopic observation (46).

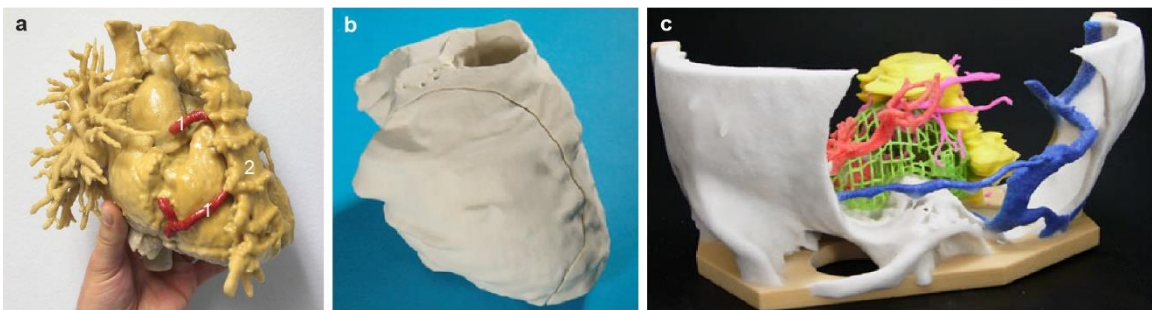


Figure 1.5. Examples of 3D printed organ models using powder-based materials with applications in cardiology and neurology. (a) A 3D printed cardiac model using starch/cellulose showing the relative position of the right coronary artery bypass graft (shown in red and labeled “1”) with respect to the patient’s sternum (labeled “2”). Adapted from reference (44). (b) A 3D printed cardiac model using plaster. Adapted from reference (7). (c) A 3D printed skull model with a mesh tumor using plaster. Adapted from reference (45).

1.2.2. Prior Work on Organ Models with Integrated Functionalities

Integration of advanced functionalities, such as electronics and sensing modules, into biological organs or organ simulators have paved new avenues in biomedical research. For instance, the integration of sensing features into organ-on-chip microphysiological models

has facilitated the quantitative monitoring of organ responses for drug screening applications (47, 48). In addition, various efforts have been focused on the development of bio-integrated electronics that can be mounted on the epidermis or on organs with the purpose of sensing and assessing physiological biomarkers (12, 49-52), or introducing new functionalities including energy harvesting from the dynamic motions of organs (53, 54).

The same strategy can be adapted for integrating advanced functionalities into physical organ models to broaden their applicability and enhance their efficacy for surgical planning and training. Previous work has shown the feasibility of incorporating such functions into organ models (55, 56). For instance, Laufer *et al.* (55) integrated force sensors (Figure 1.6 (a)) into a mold-fabricated breast model (Figure 1.6 (a) inset). The developed simulator can be used for measuring the applied force during clinical breast examination and assessing clinical skills and performance (Figure 1.6 (b)). Poniatowski *et al.* (56) incorporated UV light-sensitive assessment lines into a patient-specific, mold-fabricated pyeloplasty simulation model. The lines are not visible under normal light (Figure 1.6 (c)) or endoscopic conditions, but can be visualized under UV light (Figure 1.6 (d)). Therefore, with this integrated function, the model can be used to evaluate the twist angle at the anastomosis in training for laparoscopic pyeloplasty using the post-task Black Light Assessment of Surgical Technique (BLAST™).

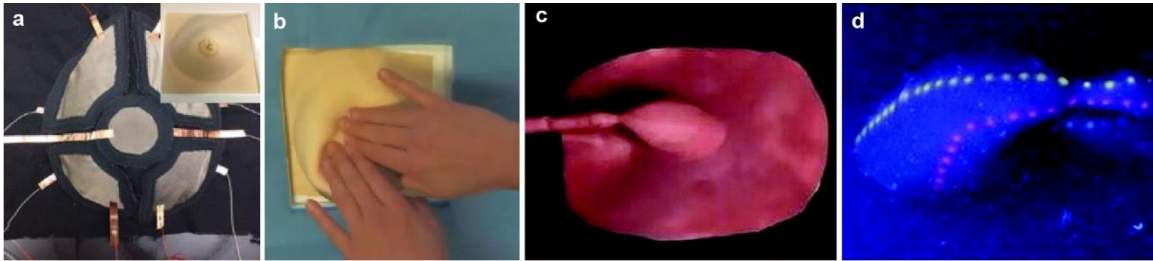


Figure 1.6. Organ models or simulators with integrated functions. (a) Force sensors were shaped to fit a breast model for a breast examination simulator. Inset: breast examination simulator with an integrated sensor. Adapted from reference (55). (b) Demonstration of the clinical breast examination on the simulator with integrated force sensor. Adapted from reference (55). (c, d) Top view of a pyeloplasty simulator model with the integrated UV light sensitive assessment lines, under room light (c) and UV (d). Adapted from reference (56).

1.2.3. Dielectric Elastomers for Soft Electromechanical Devices

Among the different classes of materials used for fabrication of soft electromechanical devices, electroactive polymers (EAPs), which exhibit mechanical deformation in response to electrical stimuli, and vice versa, have received ample attention due to their favorable properties including high elasticity, high power density, large actuation strains, fracture tolerance, scalability, low weight, low performance noise, and low cost (57, 58). An additional advantage of using EAPs over other mechanisms is their compatibility with an electrical control system. In other words, in EAPs, a correlation can often be drawn between the electrical characteristics of the material (for example resistance or capacitance) and its state of mechanical deformation. Therefore, this inherent feedback mechanism of the material can be harnessed to create a closed loop feedback to control the device performance.

Dielectric elastomer actuators (DEAs) are a type of EAPs that are made up of a thin dielectric elastomer (DE) membrane sandwiched between two compliant electrodes. Upon the application of a high electric field, the DE layer will respond in the form of an in-plane expansion and compression along its thickness (Figure 1.7). This phenomenon is governed

by the interaction between the electrostatic charges on the electrodes. In other words, the attraction of opposite charges and the repulsion of like charges on the two electrodes impose a stress on the dielectric elastomer that results in its mechanical deformation (59).

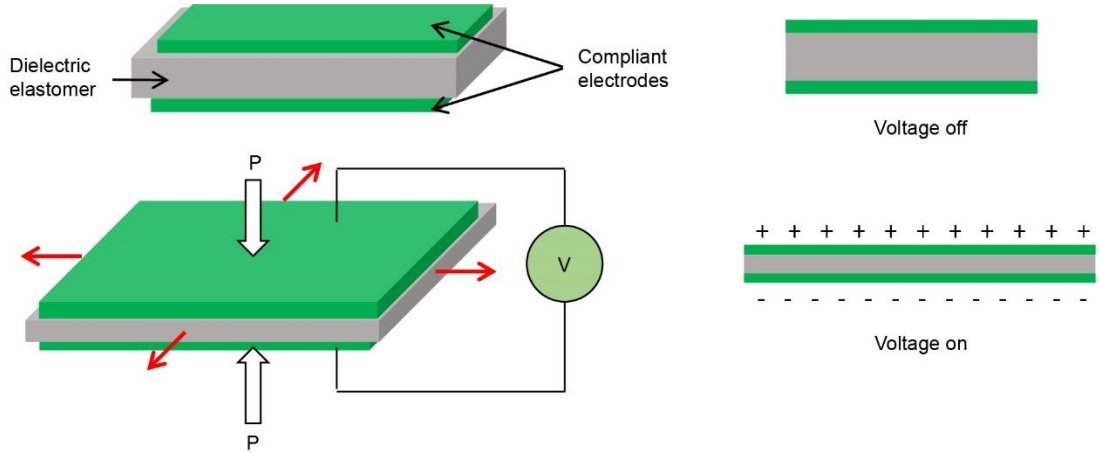


Figure 1.7. Principle of operation of a dielectric elastomer actuator. Adapted from reference (60).

The actuation stress, which is also known as Maxwell pressure, can be described as a function of applied voltage using Equation (1):

$$P = \epsilon_0 \epsilon_r E^2 = \epsilon_0 \epsilon_r \left(\frac{V}{t}\right)^2 \quad (1)$$

where ϵ_0 , ϵ_r , E , V , and t represent the permittivity of free space (8.85×10^{-12} F/m), the relative permittivity (dielectric constant) of DE, the applied electric field, the applied voltage and the DE membrane thickness, respectively (61). The strain response of a DEA depends on several factors including the DE modulus, boundary conditions and external loading (60). For a simplified case with small strains (<10%), free boundary conditions, and with the assumption of an ideal rubber (i.e.: incompressible rubber with Poisson's ratio of 0.5), the strain induced on the thickness of the DE is proportional to the square of the applied voltage and can be expressed as (60, 61):

$$s = -\frac{P}{Y} = -\frac{\epsilon_0 \epsilon_r \left(\frac{V}{t}\right)^2}{Y} \quad (2)$$

where Y is the modulus of elasticity.

DEAs have superior performance in several aspects compared to other existing actuator technologies such as piezoelectric actuators, magnetostrictive actuators, or shape memory alloys; For instance, DEAs yield high strain rates (up to 380%), high electromechanical coupling efficiency (with a theoretical transduction efficiency of 80-90%), fast response speed (for small strains, over 50,000 Hz has been reported), high energy density (3.4 J/g, that is 21 times greater than single-crystal piezoelectric actuators and more than two orders of magnitude greater than most commercial actuators), high power density (1 W/g, comparing to human muscle with an energy density of 0.2 W/g), and high actuation pressure (up to 8 MPa) (62, 63). In addition, the performance characteristics of DEAs in terms of strain, density, actuation pressure, speed and efficiency are close to those of natural muscle, thus make them a proper candidate for biomimetic design (58, 60).

DEAs can be fabricated with different configurations to achieve various forms of deformations, including out-of-plane motions such as bending and buckling. For instance, the DEA structure can be constrained to a rigid frame, made into a tubular arrangement, rolled into a scroll, stacked on a flexible layer to form unimorph and bimorph structures to generate bending motion, or they can be designed to couple both planar directions into a single linear direction (spider and bowtie), or use both directions of deformation (diaphragm) (59, 64).

It should be noted that beside actuation, basic configurations of dielectric elastomers can be used in the reverse mode of transduction and convert mechanical stimuli to electrical signal or energy, thus serve as a sensor or generator element in different application areas (59, 65).

1.3. Dissertation Overview

This dissertation is organized into five chapters. The topics discussed in each chapter are as follows:

- In *Chapter 2*, a polymeric material system, compatible with direct ink writing printing process, is proposed. It was shown that the composition of this material system can be tuned to cover a wide range of soft tissue mechanical properties. As a proof of concept demonstration, the developed material system was implemented to 3D print a patient-specific prostate model.
- In *Chapter 3*, 3D printing of soft electromechanical transducers is discussed. Specifically, the development of 3D printed dielectric elastomer actuators based on ionic hydrogel-elastomer hybrids as electrically-driven bending actuators is presented. In addition, it was shown that the same strategies can be applied for 3D printing soft capacitive tactile sensor units, and sensor arrays with the end goal of their integration into organ models for providing quantitative feedback during surgical interventions.
- In *Chapter 4*, the concepts and methodologies discussed in the previous chapters are brought together to develop a 3D printed, multi-material, patient-specific model of the heart's aortic root with internal sensor array tailored for applications in transcatheter aortic valve replacement as an example of minimally invasive procedures. The efficacy

of the models was evaluated by comparing their geometrical fidelity with patient's postoperative data, as well as their *in vitro* hemodynamic performance in different cases. Furthermore, it was demonstrated that the internal sensor array can facilitate the optimization of prosthetic valve selection and placement via mapping the pressure applied on the critical region of the anatomy.

- In *Chapter 5*, concluding remarks and the future research directions are presented.

CHAPTER 2[†]

Development of Tissue-Mimicking Inks for 3D Printing Patient-Specific Organ Models

[†]The work reported in this chapter is partly in preparation for publication and is partly based on the following original publications:

- K. Qiu, G. Haghiashtiani, & M. C. McAlpine, 3D Printed Organ Models for Surgical Applications. *Annual Review of Analytical Chemistry* 11, 287-306 (2018).
- K. Qiu, Z. Zhao, G. Haghiashtiani, S. Z. Guo, M. He, R. Su, Z. Zhu, D. B. Bhuiyan, P. Murugan, F. Meng, S. H. Park, C. Chu, B. M. Ogle, D. A. Saltzman, B. R. Konety, R. M. Sweet, M. C. McAlpine. 3D Printed Organ Models with Physical Properties of Tissue and Integrated Sensors. *Advanced Materials Technologies* 3, 1700235 (2018).

2.1. Introduction

Tissue-mimicking materials, such as biopolymers (e.g., gelatin, gellan gum, agar, and agarose) and synthetic polymers (e.g., polyurethane (PU), polyvinyl alcohol (PVA), polyvinyl chloride (PVC), room-temperature vulcanizing (RTV) silicones, and polydimethylsiloxane (PDMS)) (66), have been employed in various arenas of medicine for simulation purposes, including medical imaging modalities (67-70), cardiac strain estimation (71, 72), thermal therapy (73, 74), and surgical simulation and training (75, 76). The composition of these materials can be tailored to replicate the specific properties of soft tissue depending on the application. For instance, phantoms based on polymers such as gelatin (77), agar (78), PVC (66), and PVA (79) have been developed to mimic the acoustic properties (including the speed of sound, acoustic impedance, attenuation, and backscattering coefficient) of soft tissue, and were utilized in ultrasound imaging for system calibration, development of new techniques, and training of technicians (67, 80). For developing organ models with implications in surgical planning and training, the composition of the selected material should be modified to closely match the mechanical properties (including elastic modulus, viscoelastic behavior, hardness, ultimate strength, etc.) of the biological soft tissue. Models fabricated using such materials provide more accurate haptic feedback and mechanical behavior, analogous to the real organ.

A common technique for incorporating tissue-mimicking materials in organ models is to first use 3D printing to create a mold, and then casting it with tissue-mimicking materials. These molds can be created via one of the following approaches: 1) 3D printing a negative mold of the organ and infusing it with the tissue-mimicking material (76, 81-

85), or 2) employing an approach similar to lost wax casting, i.e. directly 3D printing the organ model using commercially available materials, and using it as a template for creating a mold (for example, via silicone molding methods), and subsequently filling the mold cavity with the tissue-mimicking material to fabricate the final organ model (86-90).

Although molding techniques provide a platform for using customized tissue-mimicking materials and fabricating organ models, they fall short in different aspects that hampers their widespread adaptation for clinical practice. These mold-based fabrication procedures typically involve several steps which not only could be time, labor, and cost intensive (30, 35, 91), but also are prone to the introduction of inaccuracies to the final model (35). In addition, it is cumbersome, if not impossible to utilize molding techniques for creating organ models with complex geometries and realistic features, such as incorporating multiple materials to replicate different tissue morphologies within an organ (for instance, cancerous tissue vs. healthy tissue in an organ) or encompassing anisotropic properties of tissue. Therefore, the direct 3D printing of tissue-mimicking materials, in lieu of using molding techniques, can appreciably facilitate the fabrication of complex, patient-specific organ models with realistic, physical properties of tissue. For this purpose, the material should be formulated to have the required tissue-mimicking properties, along with desirable rheological characteristics (such as shear thinning properties) to facilitate the 3D printing process.

While the composition of some of the existing tissue-mimicking materials can be customized for 3D printing (92), they might possess specific properties that do not make them the best candidates for developing organ models for rehearsal with surgical tools. For

example, widely-used tissue-mimicking materials based on hydrogels, such as gelatin and agar, suffer from limited lifetime, mainly due to the evaporation of their water content over time or bacterial growth (93, 94). In addition, pure gelatin is prone to undesirable damage (94) due to its brittle fracture behavior (95, 96), making it unfavorable for applications in which surgical tools are used. Furthermore, PVA cryogels need to undergo multiple, prolonged freeze-thaw cycles (normally over 12 hours/cycle) to achieve the required mechanical properties (93, 94, 97). Therefore, developing 3D printable materials with convenient preparation and customization processes to match the properties of the biological tissues is of prime importance.

Among the existing 3D printing technologies, DWA (or DIW) conveniently allows the 3D printing of various types of customized materials including polymer melts, hydrogel and sol-gel precursors, colloidal suspensions, and metallic and semiconducting micro- and nanoparticles (98, 99). In this process, one or more materials of interest, commonly referred to as “inks,” are extruded through fine deposition nozzles under an applied pressure, while a robotic positioning system controls the motion of the nozzle and the printing pathways.

The DWA technique has been previously harnessed to 3D print models of the aortic root from house-hold silicone for conducting surgical training on transapical aortic valve replacement procedures (91, 100). However, these efforts did not involve the customization of the ink material to precisely mimic the properties of tissue. In another recent study, von Rundstedt *et al.* (101) used two silicone-based inks in a DWA process to 3D print models of patients’ kidneys including their tumor anatomies. The models were utilized for rehearsal of robot-assisted laparoscopic enucleation of the kidney tumor using the da

Vinci® robotic system. It was stated that the inks could mimic the properties of the normal kidney and tumor tissue; however, no characterization results were provided to support this claim.

In this chapter, a polymeric material system, compatible with DWA printing process, is proposed. It was shown that the composition of this material system can be tuned to cover a wide range of soft tissue mechanical properties. As a proof of concept demonstration, the developed material system was implemented to 3D print a patient-specific prostate model.

2.2. Development of Tunable 3D Printable Polymeric Materials with Patient-Specific Physical Properties

Biological soft tissue and organs mostly exhibit elastic moduli spanning from ca. 0.1 kPa to ca. 1 MPa (102). Hence, the proposed material system should primarily have adjustable properties in order to cover the moduli in this range and replicate the properties of tissue of interest. In addition, the proposed material should satisfy other requirements including good printability, maintaining stable structures and properties during and after printing, vulcanization at room temperature within a reasonable time period, and facile preparation. To address these requirements, we developed a polymeric material system that consisted of two main components: an active agent and a bulking agent thus yielding a composite structure analogous to the nature of human tissue (103, 104) (Figure 2.1 (a)). In our final formulation, a silicone sealant (RTV sealant Loctite SI 595 CL) was used as the active agent for vulcanization to stabilize the structure, while a silicone grease (Trident LP20) was applied as the bulking agent for introducing softness and flexibility into the

structure. Additives, such as coloring agent or thickening agent, were also optionally added to the composition for tuning the color of the material or adjusting its printability. The main components in this ink system are all silicone-based materials, which enables their homogeneous mixture. In addition, silicone-based materials exhibit advantageous characteristics including shear thinning behavior, resistance to polymer creep before crosslinking, and good elasticity after crosslinking.

By adjusting the weight ratio of bulking agent (B) to active agent (A) for different ink formulations, the properties of the customized polymeric inks can be altered. As shown in Figure 2.1 (b, c), by increasing the weight ratio of the bulking to active agent from 0 to 2.05, the corresponding values of Young's moduli decrease from 677.6 ± 28.8 to 37.5 ± 1.9 kPa. Importantly, the value range of the Young's moduli of the inks falls in the broad range of values reported for soft tissue, hence, this trend can be used to tailor the mechanical properties of the materials to simulate tissues/organs of interest.

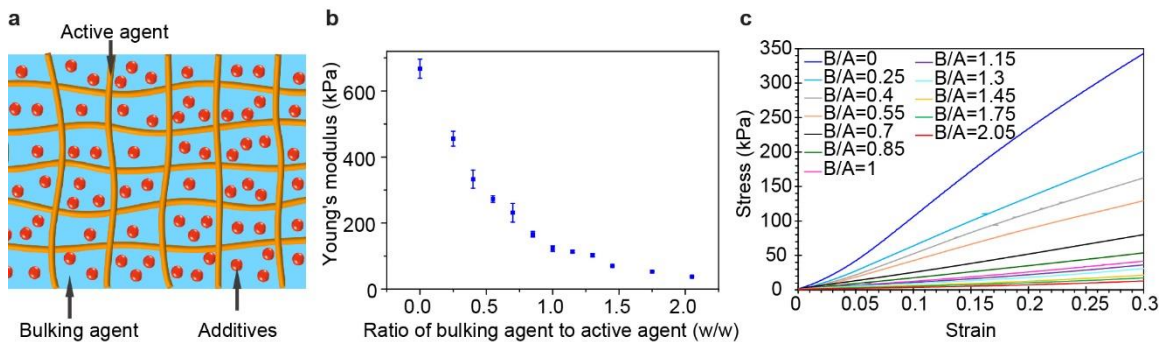


Figure 2.1. Design and development of customized polymeric materials. (a) Schematic of the composite structure of the customized polymeric inks. (b) Young's modulus (<3% strain) of the custom-formulated polymeric material versus different weight ratios of the components. (c) Stress-strain plots of the custom-formulated polymeric materials with different formulations (B/A represents the weight ratio of bulking agent to active agent).

The tunability of the mechanical properties of this material system by adjusting the component ratios is correlated to the crosslinking density. To verify this, a sol-gel fraction

analysis test was performed by immersing the samples of the polymeric materials with different component ratios in the organic solvent hexane (Figure 2.2). It was observed that as the weight ratio of bulking agent to active agent increased from 0 to 1.75, the corresponding normalized weight loss of the materials ($\Delta m/m_0$, where m_0 represents the initial dry weight of the materials and Δm corresponds to the changes in the weight) after 96 hours of immersion in the solvent increased from 10.9% to 78.1% (Figure 2.2 (a)). This trend correlates with the weight ratio of bulking agent (silicone grease) in the formulation which does not involve in ink crosslinking, as well as the non-crosslinked components in the active agent (silicone sealant), hence, confirming that the increase in the weight ratio of bulking agent in the composition reduces the degree of crosslinking and results in softer materials.

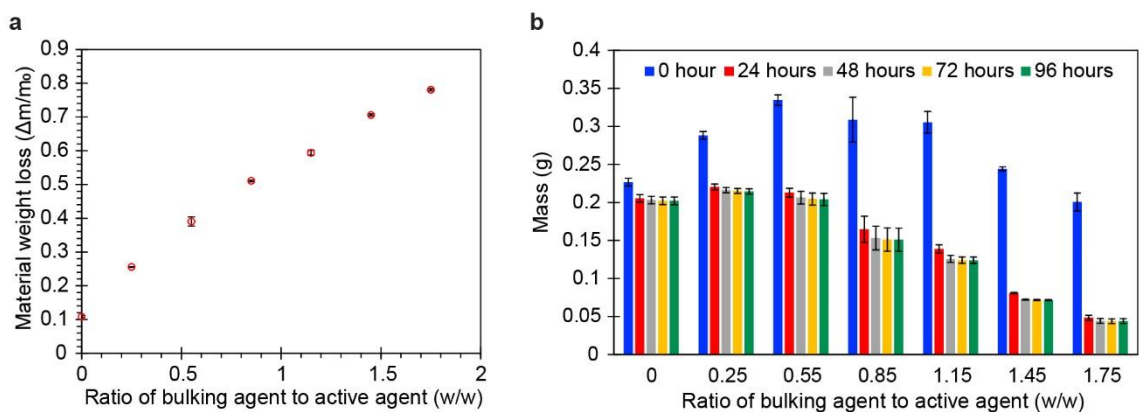


Figure 2.2. Sol-gel fraction analysis of the customized polymeric materials in hexane. (a) Normalized ratio of material weight loss for different compositions of the customized polymeric material after 96 hours of immersion in hexane. (b) Mass changes for different compositions of the customized polymeric material in hexane at different time stamps after immersion in the solvent.

For the applications explored in this work, the customized polymeric materials were used to 3D print organ models that were mainly used in air or a blood-mimicking solution comprising of water and glycerol. Therefore, we investigated the stability of the materials

with different formulations in these two environments. The results showed that different formulations of the polymeric material (B/A ranging from 0 to 1.75) were stable without any significant weight loss after 96 hours of exposure to ambient air environment (Figure 2.3 (a)), as well as immersion in water/glycerol solution (Figure 2.3 (b)). This confirmed that the 3D printed models using these custom-formulated inks can maintain stable properties for applications conducted in these test environments.

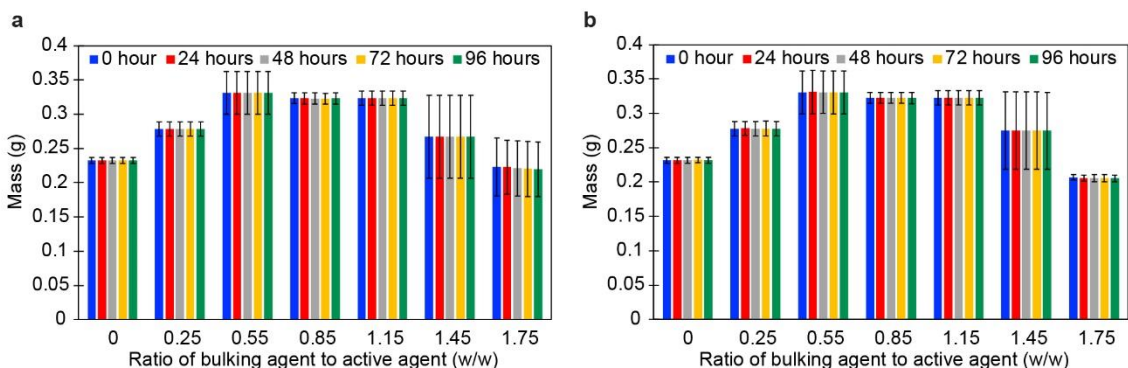


Figure 2.3. Stability of the customized polymeric materials in different test environments. (a) Mass changes for different compositions of the customized polymeric material in hexane at different time stamps of exposure in ambient air. (b) Mass changes for different compositions of the customized polymeric material in water/glycerol solution at different time stamps after immersion.

In addition, we investigated the rheological properties of the custom-formulated inks and their compatibility with DWA printing process. First, we performed viscometry tests on the main components of the inks (active and bulking agents) and examples of formulations (B/A=0.25, 0.7, 0.85, 1.15) to observe the changes in the apparent viscosity of the inks by varying the shear rate. As shown in Figure 2.4 (a), as the shear rate increased from 10^{-1} to 10^3 s^{-1} , the apparent viscosity of the inks decreased from about 10^3 to $1 \text{ Pa}\cdot\text{s}$. This trend indicated the shearing thinning behavior of the developed inks. Shear thinning is a property attributed to non-Newtonian fluids, which results in a decrease in the viscosity of a fluid under applied shear strains. Therefore, it facilitated the flow of the ink materials

through the deposition nozzle due to a decrease in the viscosity under the imposed shear rates during the printing process, as well as sustaining of the shape of the printed inks after deposition onto the substrate (99). In addition, the inks exhibited yield stress behaviors (Figure 2.4 (b, c)) in the oscillatory rheometry test, which was also advantageous for the 3D printing process. Particularly, applying pressures to the ink beyond the yield point during the printing process, allowed for the extrusion of the ink through the nozzle as a result of reduction in the storage modulus (G'), and ultimately its decrease to a value lower than loss modulus (G'') ($G' < G''$, viscous liquid-like behavior). Once the ink was deposited and the shear stress on the material was relieved, the storage modulus increased to its plateau value in the linear viscoelastic region (in the range of 10^3 - 10^4 Pa for the example formulations), which facilitated the shape retention of the deposited ink ($G' > G''$, solid-like behavior) (105).

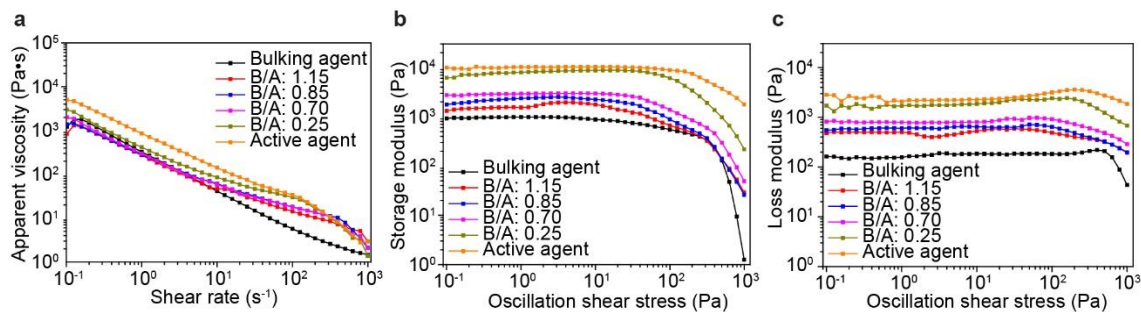


Figure 2.4. Rheological characterization of custom-formulated polymeric inks. (a) Viscometry data of different custom-formulated polymeric inks and comparison to active and bulking agents. (b) Oscillatory rheology data of the storage modulus of different custom-formulated polymeric inks and comparison to active and bulking agents. (c) Oscillatory rheology data of the loss modulus of different custom-formulated polymeric inks and comparison to active and bulking agents (B/A represents the weight ratio of bulking agent to active agent).

Finally, to further establish the merits of the customized polymeric inks, a comparison between the Young's modulus of biological tissues with the developed inks, other tissue-mimicking materials, and commercial rigid-plastic and elastomeric (rubber-like) polymers

has been compiled in Figure 2.5.

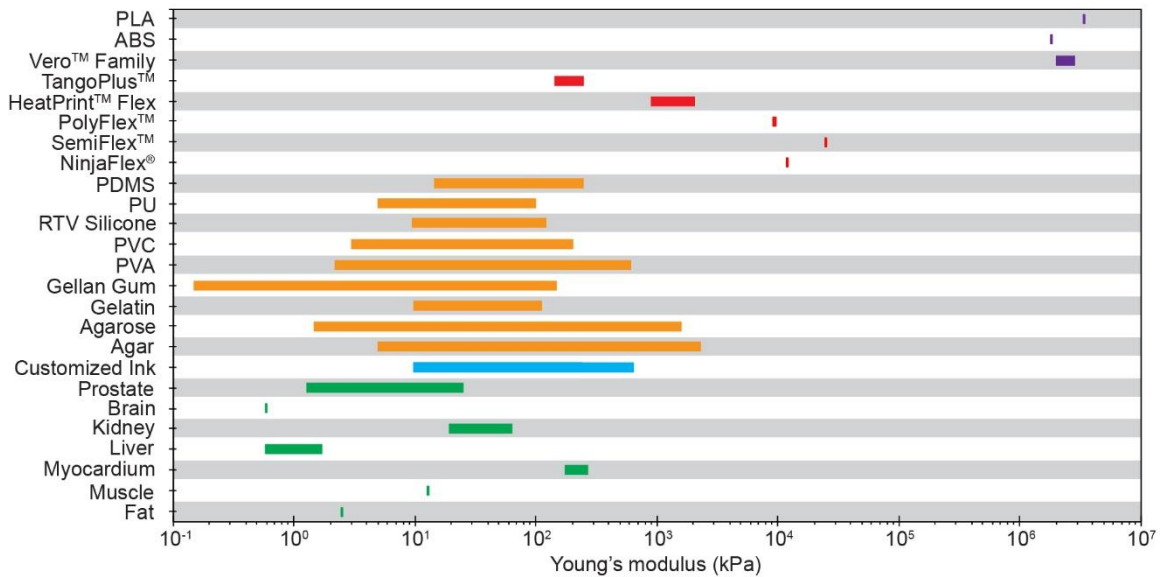


Figure 2.5. Comparison of Young's modulus of biological tissues (green) with different materials including customized polymeric ink (blue), tissue-mimicking materials (orange), commercial 3D printing elastomeric (rubber-like) materials (red), and commercial 3D printing rigid plastics (purple). Data for all human biological tissues are retrieved from reference (66), except for myocardium and kidney, which are porcine tissue retrieved from references (106) and (107), respectively. Data for all tissue-mimicking materials are retrieved from reference (66). Data for commercial 3D printing materials including NinjaFlex®, SemiFlex™, PolyFlex™, HeatPrint™ Flex, TangoPlus™, Vero™ Family, and ABS/PLA are retrieved from references (108-114), respectively.

2.3. Proof of Concept Demonstration: 3D Printed Patient-Specific Prostate

Model

To demonstrate the applicability of the developed material system for 3D printing patient-specific organ models with physical properties of tissue, we chose the prostate as a proof-of-principle organ model, due to its relatively simple geometry. In addition, prostate surgeries have inherent risks for damaging the urethral sphincter and neurovascular bundle (NVB) during prostate removal, and therefore, proper preoperative planning and rehearsal via a 3D printed prostate model may have implications for surgical outcomes in millions of patients worldwide (115).

In the first step, we performed mechanical characterization of human prostate tissue samples and compared the results to the developed material system in order to select the formulation with proper ratio of the components to mimic the properties of their biological counterparts. For this purpose, we obtained the stress-strain curves for cylindrical samples from patient prostate tissue in static compression test and compared the results to samples of customized polymeric inks (Figure 2.6 (a)). At 0-0.15 strain range (an acceptable range for most surgical tasks on prostate), the customized polymeric inks 1, 2 and 3 (with B/A~3.21, 3.44, and 3.88, respectively), closely matched the general trends of stress-strain curves obtained from three prostate tissue samples, suggesting patient-specificity in ink composition. The Young's moduli for strains less than 10% for representative samples of inks 1 (31.6 kPa), 2 (26.0 kPa) and 3 (12.4 kPa) are analogous to tissue samples 1 (25.7 kPa), 2 (20.3 kPa) and 3 (10.9 kPa). For higher strains, the modulus values increase with a nonlinear trend for tissue samples (due to viscoelastic, poroelastic and anisotropic properties of soft tissue (116-118)) and polymeric ink samples (due to viscoelastic behavior). The values obtained for Young's moduli are also comparable to previous reports for the prostate tissue samples (119), and are well below the values for typical 3D printed hard plastics and rubber-like materials.

After demonstrating the capability of tailoring ink composition to match the properties of a specific prostate tissue, we chose the ink 2/tissue 2 pair as a representative example for the remainder of the characterizations, 3D printing and proof of concept demonstrations. For quantitative analysis of the fidelity of dynamic compression properties, the mechanical responses of cylindrical samples under applied dynamic

compression were evaluated and compared for ink 2 and the corresponding tissue 2 (Figure 2.6 (b, c)). Both storage (E') and loss (E'') moduli for cylindrical samples of tissue 2 and ink 2 at 0.05, 0.10 and 0.20 strains showed high fidelity. For the storage modulus, the values for both tissue and ink increased with increasing oscillation frequency (0.1 Hz to 20 Hz) and strain (0.05 to 0.20). The trends of the obtained results are similar to previous reports for biological tissue exhibiting viscoelastic properties (118, 119). For the loss modulus, the values only indicated a clear increase with oscillation frequency.

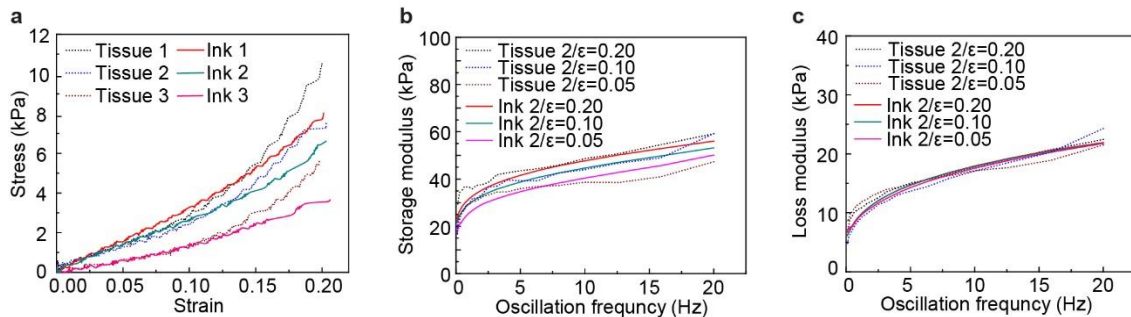


Figure 2.6. Comparison of mechanical properties of the custom-formulated polymeric materials with prostate tissue specimens. (a) Stress-strain plots of patient prostate tissue samples (Tissue 1, 2, 3) and samples of customized polymeric inks (Ink 1, 2, 3) in static compression test. (b) Dynamic compression fidelity of storage modulus between a patient prostate tissue sample (Tissue 2) and a sample of customized polymeric ink (Ink 2) at frequencies of 0.1-20 Hz and strains of 0.05, 0.10, and 0.20. (c) Dynamic compression fidelity of loss modulus between a patient prostate tissue (Tissue 2) and a sample of customized polymeric ink (Ink 2) at frequencies of 0.1-20 Hz and strains of 0.05, 0.10, and 0.20.

After selecting the ink formulation with properties commensurate to the prostate tissue, information about the prostate anatomy was extracted from MRI scans. This information was utilized to create a stereolithographic (STL) model and sliced into horizontal layers to generate G-code for the 3D printing process using our custom-built 3D printing system (Figure 2.7 (a)). Unlike conventional commercial 3D printers that use heating for extrusion of thermoplastic filaments, this setup uses adjustable pressure settings, which is better suited to handle the shear thinning properties of silicone-based

polymeric inks at room temperature. The 3D printing process (Figure 2.7 (b)) follows the pathways dictated by the corresponding sliced STL model in order to generate the final 3D printed prostate model (Figure 2.7 (c)).

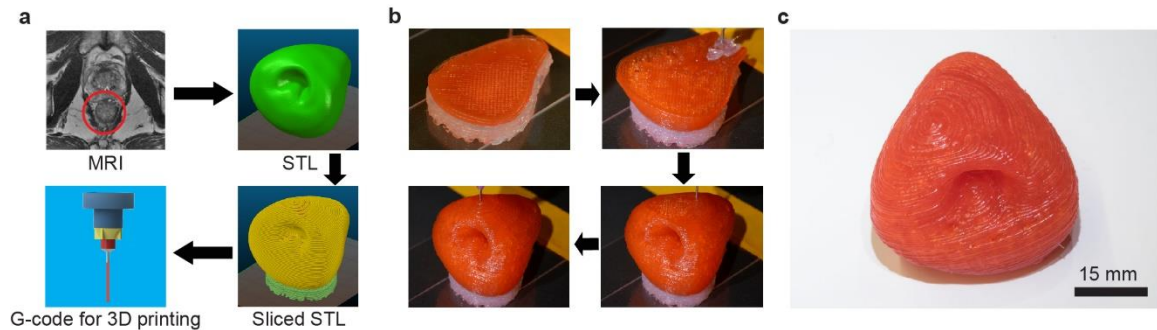


Figure 2.7. 3D printing of patient-specific prostate model. (a) Procedure for converting patient-specific MRI to G-code for the 3D printing process. (b) Layer-by-layer 3D printing process of the prostate model using the customized polymeric ink. (c) Image of the final 3D printed prostate model.

After 3D printing and curing of the model in ambient air, a quantitative analysis of the organ model was performed to quantify the fidelity of the anatomy between the 3D printed prostate model and its corresponding patient prostate. For this purpose, a 3D registration technique was used for surface comparison in order to analyze the anatomical fidelity (120). The 3D printed prostate model was scanned by MRI, and then the MRI image stack (Figure 2.8 (a)) was utilized to generate an STL model. A calibrated distance map (Figure 2.8 (b)) and a histogram of the calibrated distances (Figure 2.8 (c)) of the corresponding points on the surface of the patient prostate model and 3D printed prostate model were generated via 3D registration. The results indicated that the anatomical difference for the outer surface (Figure 2.8 (b), left) and inner urethra surface (Figure 2.8 (b), right) is trivial, and most of the calibrated distance points scatter from -0.8 to 0.3 mm, with peaks close to 0 mm (Figure 2.8 (c)). The overall anatomical fidelity was found to be 98%.

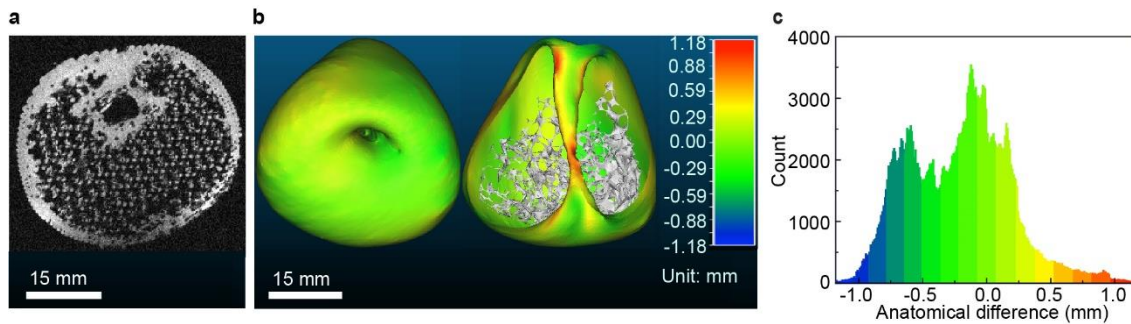


Figure 2.8. Anatomical fidelity analysis of the 3D printed model in comparison with patient’s prostate. (a) An MRI image obtained via scanning a 3D printed prostate model. (b) Calibrated distance map obtained via 3D registration for comparison of anatomical fidelity between patient prostate and 3D printed prostate model at the outer surface (left) and urethra surface (right). (c) Histogram of the calibrated distances of the surface points for comparison of anatomical fidelity between patient prostate and 3D printed prostate model.

Finally, we demonstrated the application of the 3D printed prostate models for surgical rehearsal with diagnostic and surgical tools. For instance, an endoscope was inserted into the urethra of the 3D printed prostate model (Figure 2.9 (a)). Due to the matching physical properties of the model with tissue, the endoscope can be easily inserted into the urethra to obtain an unobstructed endoscopic view for any region of the surface, even under conditions of pressing or squeezing (Figure 2.9 (b)). The endoscopic view from the 3D printed prostate model shows the unfilled prostatic urethra in the patient’s MRI which is neither dilated by the endoscope, nor filled by irrigating fluid and urine. Thus, this application suggests the effectiveness of these organ models in assisting medical professionals for more efficient planning and rehearsal from organ inner channels via the use of an endoscope.

In addition, we performed a suturing practice on the 3D printed prostate model with the aid of a surgeon (Figure 2.9 (c)). Although this is not a common practice for the prostate organ, it indicates that the 3D printed models exhibit sufficiently good strength to avoid excessive damage during invasive surgical procedures, such as needle penetration.

Furthermore, feedback from the surgeon indicated that the 3D printed prostate model remained robust during suturing, it did not exhibit any tearing, and the surgical knot did not pull through.

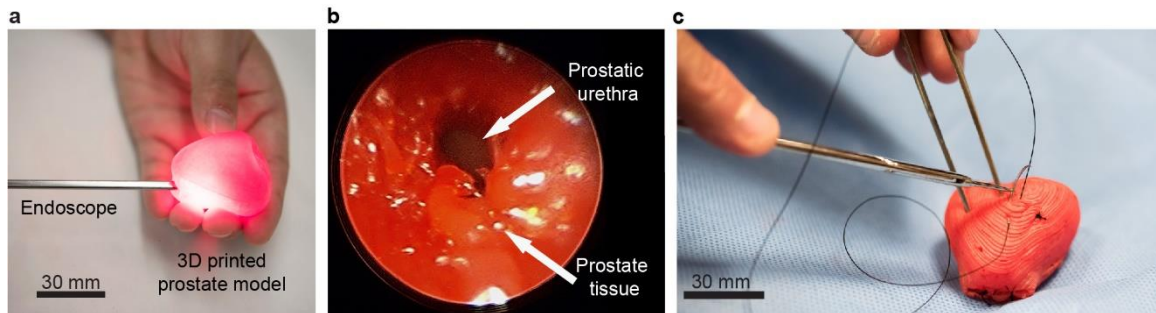


Figure 2.9. Examples of potential application of the tissue-mimicking prostate model in surgical rehearsal and training. (a) Surgical rehearsal involving applying an endoscope in the urethra of the 3D printed prostate model. (b) Endoscopic view of the urethra inside of the 3D printed prostate model. (c) Surgical suturing on the 3D printed prostate model.

2.4. Conclusion

In this chapter, a silicone-based material system mainly comprising of an active agent and a bulking agent was proposed. It was shown that by adjusting the weight ratios of these two components in the formulation, the crosslinking density of the material can be altered. Consequently, the mechanical properties and the elastic modulus of the material can be tuned to match the broad range of reported moduli for soft tissue. In addition, rheological studies confirmed the favorable properties of this material system for the DWA 3D printing process, including shear thinning and yield stress behavior. As a proof of concept demonstration, the material formulation was optimized to mimic the static and dynamic mechanical behavior of tested specimens of human prostate tissue. The selected formulation was used in the 3D printing process to fabricate patient-specific model of the prostate. A quantitative analysis confirmed the fidelity of anatomy between the 3D printed prostate model and the corresponding patient's organ. Preliminary explorations of the

model for applications in preoperational rehearsal with diagnostic and surgical tools demonstrated that such organ models could aid medical professionals to perform more effective preoperative planning. In addition, the tissue-like tactile sensation can help to hone surgical skills for training purposes.

Additional details on experimental methods, materials, and other supplementary information for this chapter is provided in Appendix A.

CHAPTER 3[†]

3D Printing Soft Electromechanical Transducers

[†]The work reported in this chapter is partly based on the following original publications:

- G. Haghighashtiani, E. Habtour, S. H. Park, F. Gardea, & M. C. McAlpine. 3D Printed Electrically-Driven Soft Actuators. *Extreme Mechanics Letters* 21, 1-8 (2018).
- K. Qiu, Z. Zhao, G. Haghighashtiani, S. Z. Guo, M. He, R. Su, Z. Zhu, D. B. Bhuiyan, P. Murugan, F. Meng, S. H. Park, C. Chu, B. M. Ogle, D. A. Saltzman, B. R. Konety, R. M. Sweet, M. C. McAlpine. 3D Printed Organ Models with Physical Properties of Tissue and Integrated Sensors. *Advanced Materials Technologies* 3, 1700235 (2018).

3.1. Introduction

Since the early 1500s, when Leonardo da Vinci explored the possibility of human flight by observing and attempting to imitate birds, the concept of “biomimetics” – the ability to emulate nature and living organisms – has inspired a plethora of scientific discoveries and engineering innovations that have led to novel materials, mechanisms, and devices (*121, 122*). Among these efforts is the development of “soft robots” with the purpose of reproducing locomotion, morphing structures, sensing, and emulating other distinctive capabilities of active biological organisms (*58, 123-125*). The field of soft robotics is primarily enabled by advances in the development of soft materials with properties commensurate to their biological counterparts.

In recent years, ionic hydrogel-elastomer hybrids, which are formed by laminating layers of hydrogels and elastomers together, have attracted vast attention owing to their favorable characteristics. Specifically, elastomers are resilient materials with low elastic modulus (~ 0.1 MPa to ~ 100 MPa), high failure strains ($> 300\%$ strain) (*126*), and resistance to extreme environmental conditions such as changes in temperature (*127*). Moreover, ionic hydrogels are soft, transparent, conductive materials which employ ions as the charge carriers as opposed to electrons in conventional electrode components. It has been demonstrated that such hydrogels remain functional at high voltages (above 10 kV) and high frequencies (above 10 kHz), and can exhibit large stretchability (area strain of 167%) with high transmittance and low sheet resistance (*128*). Furthermore, the combination of these two materials has been found to be analogous to human skin, with the elastomer replicating the epidermis layer, and the ionic hydrogel mimicking the dermis

layer, including signal transfer via ions as part of the natural sensing mechanism (129, 130). Such ionic hydrogel-elastomer hybrids have been used in development of soft devices and stretchable electronics including sensors (130-133), actuators (128, 134), mechanical energy harvesting devices (135), electroluminescent skins (136, 137), electrical interconnects (138), flexible circuit boards, and stretchable microfluidic chips (129).

Conventional methods used for the fabrication of soft devices typically involve post-processing steps, or manual assembly of the parts. Recent advances in extrusion-based, direct ink writing (DIW) approaches for multi-material 3D printing allow for the incorporation of various functional layers in high density and with fine features in the fabrication process, thus paving a path for the facile creation of soft devices with complex geometries and integrated functionalities (139). It has been demonstrated previously that hydrogel and elastomer precursors can also be employed in a DIW process for fabricating functional soft sensors (131, 132).

In this chapter, we discuss the development of a dielectric elastomer actuator (DEA) in unimorph configuration, which is the first demonstration of 3D printing ionic hydrogel-elastomer hybrids for fabricating electrically-driven bending actuators. In addition, we demonstrate that the same strategies can be applied for 3D printing a soft capacitive tactile sensor unit, and a sensor array with the end goal of their integration into organ models for providing quantitative feedback during surgical interventions.

3.2. Mechanism of Actuation in DEAs Based on Ionic Hydrogel-Elastomer Hybrids

In hydrogel-elastomer hybrids, the dielectric elastomer membrane is sandwiched between two layers of ionic hydrogel electrodes, forming the active region of the device. As shown in Figure 3.1 (a), two metallic electrodes were then placed in contact with ionic hydrogels on each side and outside of the deformable region, to provide the contact leads for voltage application (128). The interface of metallic electrode/ionic hydrogel conductor forms an electrical double layer (EDL) on each side, and along with the dielectric layer, the whole structure acts as three capacitors in series (Figure 3.1 (b)). The metallic electrodes and ionic conductors (electric double layers) are separated by charges on the order of nanometers, while the separation of charges on the two sides of the dielectric elastomer layer is equal to its thickness (on the order of hundreds of microns). Consequently, the electrical double layers have higher capacitance compared to the dielectric layer (about seven orders of magnitude higher) ($C \sim \frac{A}{d}$, where C , A , and d represent the capacitance, area, and separation distance). When a high electric field is applied to the device in the actuation mode (Figure 3.1 (c)), since the capacitors in series add up to the same amount of charge ($C_D V_D = C_{EDL} V_{EDL}$, where C and V are the capacitance and voltage, and subscripts D and EDL represent the dielectric layer and the electrical double layer, respectively), much of the applied voltage drops across the dielectric layer, and the voltage across the electrical double layer remains much smaller than 1 V. The small value of V_{EDL} prevents electrochemical reaction, while the larger value of V_D allows for the

electromechanical transduction (128). Therefore, the dielectric elastomer layer experiences in-plane areal expansion and contraction along its thickness.

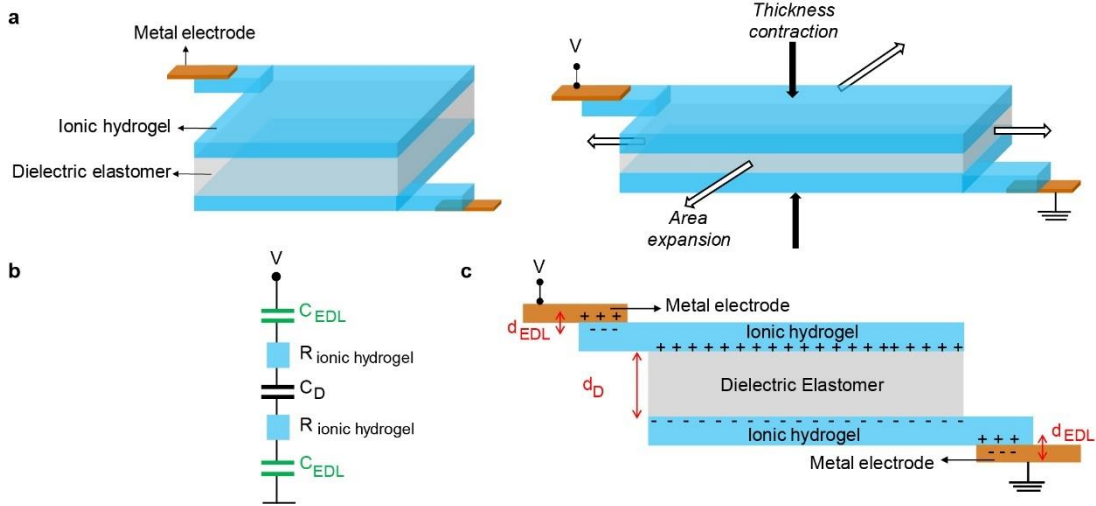


Figure 3.1. Mechanism of actuation in DEAs based on ionic hydrogel-elastomer hybrids. (a) Structure of the DEA with ionic hydrogel electrodes prior to voltage application (left) and actuation performance of the device upon the application of voltage (right). (b) The equivalent circuit of the structure representing three capacitors in series. (c) Schematic of the device cross section upon voltage application and actuation. Adapted from reference (128).

In the unimorph DEA configuration, the device resembles a cantilever in which the unit DEA structure is attached to a stiffer passive layer. Upon the application of high electric fields, the in-plane expansion of the dielectric layer is translated to an out-of-plane bending motion due to the restriction imposed by the passive layer (Figure 3.2) (59, 140).

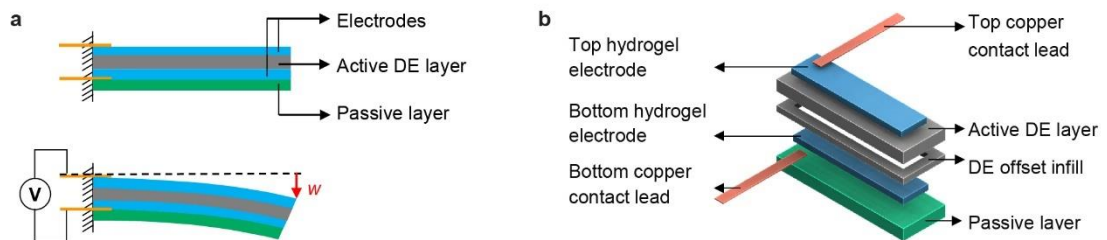


Figure 3.2. DEA structure and components in unimorph configuration. (a) Schematic of a bending unimorph DEA. (b) Exploded view of the DEA device and different constituent material layers.

3.3. Optimization of Ink Formulations for 3D Printing

The first step in developing the unimorph DEA is tailoring and optimizing the individual material compositions for the electrodes, the active dielectric elastomer, and the passive layer in order to satisfy printability and device performance requirements. To manipulate the selected materials in the DIW process, careful consideration of the rheological properties of the inks (viscosity, yield stress, and viscoelastic moduli) is required. Specifically, the selected ink materials should exhibit shear thinning behavior, a property attributed to non-Newtonian fluids, which results in a decrease in the viscosity of a fluid under applied shear strains. The shear thinning behavior facilitates the flow of the ink materials through the deposition nozzle due to a decrease in the viscosity under the imposed shear rates during the printing process, while sustaining the shape of the printed inks after deposition onto the substrate (99). In addition, the ink materials should preferably require no post-processing steps, in an effort to maintain a comprehensive fabrication process on the printer platform, thus simplifying the process.

Combining low and high molecular weight polymers for formulating the composition of ionic hydrogels and other materials, including silicones, has been demonstrated to be a viable strategy for modifying their rheological properties, thus rendering them suitable for use in the DIW process (131, 132). In these material systems, the high molecular weight polymer is used to modify the viscosity and yield stress of the ink (131, 132), while the crosslinking of the low molecular weight polymer dictates the material elasticity (131).

Here, we adopted a similar strategy to formulate the composition of the main components of the device. Following optimization, the composition of the UV curable,

ionic hydrogel used for the compliant electrodes consisted of 7.9 wt.% acrylamide (AAm) as the monomer, 3.16 wt.% polyacrylamide (PAM, Mol. Wt.=5,000,000) as the rheology modifier, 21.48 wt.% lithium chloride (LiCl) for ion induction, 0.13 wt.% *N,N'*-Methylenebisacrylamide (MBAA) as the crosslinking agent, 0.08 wt.% Irgacure 1173 as the photoinitiator, and 37.6 wt.% ethylene glycol (EG) along with 29.64 wt.% ultrapure water as the solvents. The hygroscopic properties of LiCl used in this formulation improved the water retention of the hydrogel, thus increasing its longevity and preventing dehydration that could inhibit its performance as an electrode in the DEA (141).

The final composition of the active dielectric layer in this study included 20 wt.% barium titanate (BaTiO₃) nanoparticles (<100 nm, cubic) in a UV curable silicone matrix comprising high molecular weight silicone sealant (Loctite® 5039™ Nuva-Sil®) and a two-part silicone elastomer (Wacker SEMICOSIL® 912 as the base and ELASTOSIL® CAT UV as the catalyst with a 10:1 mixing ratio) at a 1:1 weight ratio. Silicone elastomer was utilized due to its relatively fast and stable electromechanical response, low mechanical loss (61, 142), and availability in a wide range of viscosities, curing rates, and mechanical properties. Furthermore, BaTiO₃ particles possess a high dielectric constant that can range from 500 to 6900 at room temperature depending on the synthesis method, and levels of purity, density, and grain sizes (143). Thus, the inclusion of BaTiO₃ in a silicone matrix yields an elastomeric composite material with an enhanced dielectric property and electromechanical sensitivity (144-147).

Finally, we used a UV curable, one-part silicone sealant (Loctite® 5084™ Nuva-Sil®) as the passive layer due to its higher stiffness (relative to the dielectric elastomer), non-

corrosiveness, and facile printability. The 3D printing of the individual materials was optimized based on the nozzle tip diameter, extrusion pressure, and printing speed (Table B.1 in Appendix B).

3.4. Materials Characterization

The shear thinning behavior of the ionic hydrogel and the dielectric elastomer inks was confirmed by performing viscometry tests on material precursors in the uncured state (Figure 3.3 (a)). The shear thinning behavior for both materials occurred at shear rates above 0.1 s^{-1} , which facilitated their extrusion through the deposition nozzles. Specifically, during extrusion from nozzles with specified diameters and printing speeds (Table B.1 in Appendix B), the hydrogel and DE inks experienced shear rates of ca. 78.19 s^{-1} , and 111.85 s^{-1} , at which the exhibited apparent viscosities were $3.20 \text{ Pa}\cdot\text{s}$, and $21.93 \text{ Pa}\cdot\text{s}$, respectively (Appendix B). The shear yield stress, σ_y , along with the storage (G') and loss (G'') moduli of the inks, were obtained by performing oscillatory rheometry on the materials (Figure 3.3 (b)). The hydrogel and DE inks exhibited yield stresses of $\sim 51 \text{ Pa}$ and 253 Pa (determined as the value of shear stress at the limit of linear viscoelastic region), respectively. It is important to point out that both G' and G'' remained constant below the yield values; however, beyond the yield points, both materials experienced a drop in G' and G'' . Manipulating the yield behavior of the inks provided two key fabrication advantages: (i) a decrease in the storage modulus beyond the yield point improved the controllability of the ink extrusion; and (ii) an increase in storage modulus (G' reached values of $\sim 69 \text{ Pa}$ and 1034 Pa , for hydrogel and DE inks, respectively) at shear stresses below the yield values

facilitated the shape retention of the printed materials after their deposition on the substrate (105).

To evaluate the overall performance of the device components, mechanical and electrical characterizations were conducted, consisting of uniaxial tensile tests of the three materials (ionic hydrogel, DE layer, and passive layer), and studying the changes in resistance of hydrogel electrodes with applied strains. The uniaxial tensile tests were performed to ensure that the hydrogel electrodes were compliant to the dielectric layer, and the passive layer had a higher stiffness compared to the dielectric layer to yield out-of-plane motion (Figure 3.3 (c)). All materials exhibited a non-linear hyperelastic behavior. The elastic modulus of the passive layer, silicone dielectric elastomer, and ionic hydrogel electrodes at 100% strain were estimated as 167.57 ± 36.27 kPa, 39.82 ± 7.15 kPa, and 8.77 ± 3.00 kPa, respectively.

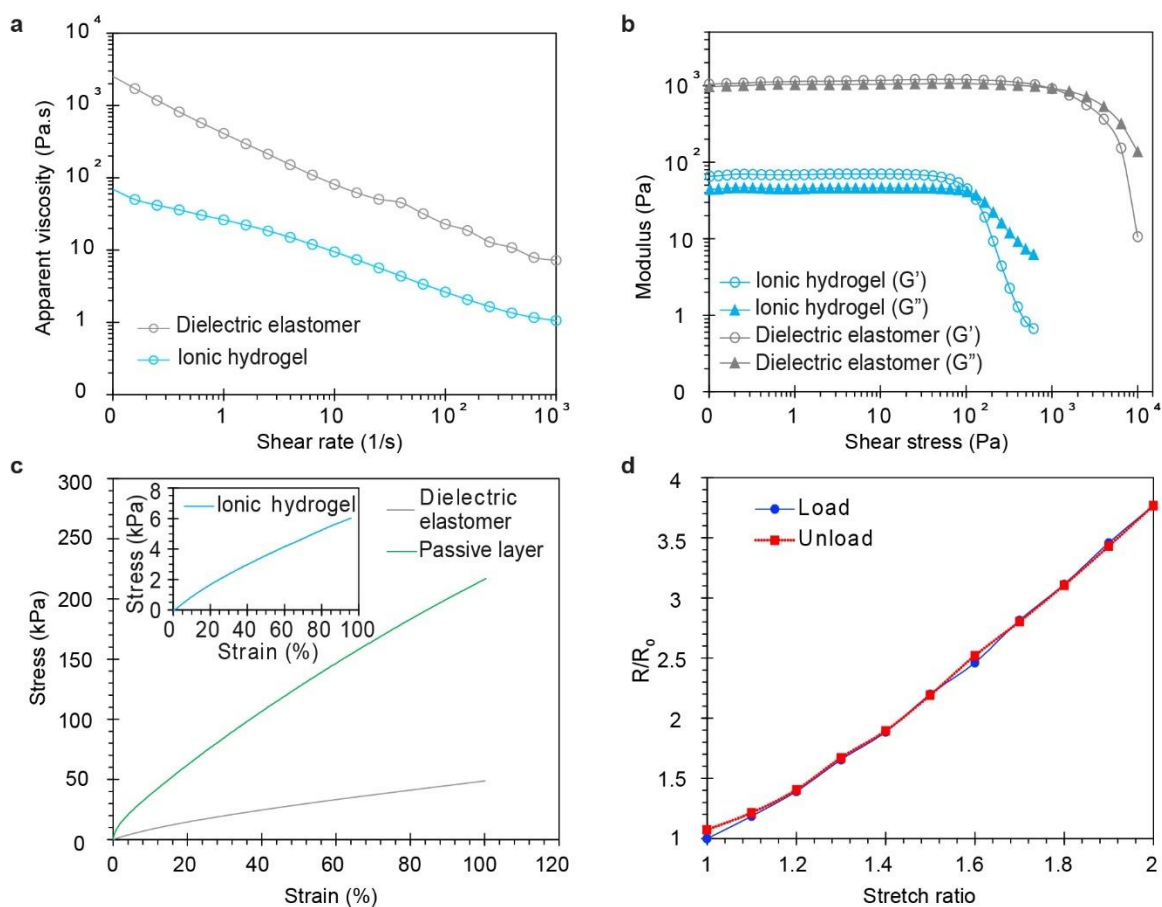


Figure 3.3. Materials characterization. (a) Viscometry and (b) oscillatory rheology data including the storage modulus (G') and loss modulus (G'') of the ionic hydrogel electrode and the silicone/BaTiO₃ dielectric layer. (c) Stress-strain plots of the three components. (d) Changes in resistance of the ionic hydrogel at different stretch ratios for loading and unloading cycles.

We examined the effect of uniaxial stretching on the changes in resistance of 3D printed ionic hydrogel electrodes in loading and unloading tests (Figure 3.3 (d)). The increase in the resistance of the hydrogel with increasing stretch ratio was consistent with the expected trend of $R/R_0 = \lambda^2$ for a conductive material with resistivity independent of applied stretch, where R_0 and R represent the resistance before and after stretching the hydrogel λ times its initial length, respectively (128). In addition, no significant hysteresis was observed in the changes in resistance during loading and unloading cycles.

3.5. Overcoming Materials Incompatibilities and Device Fabrication

The fabrication of the DEA device required the stacking of different material layers in the DIW process, followed by post-deposition crosslinking and curing of each layer prior to the deposition of subsequent layers. One of the main challenges that should be addressed during the device fabrication process was the integration of the different materials and overcoming their incompatibilities. This issue arose from the fact that silicone-based materials are hydrophobic, and the hydrogel ink is hydrophilic. Therefore, effective surface engineering strategies should be incorporated in the device fabrication process in order to overcome the surface dewetting that results from the weak interactions between the hydrogel droplet and the underlying silicone layer.

There exist several promising surface engineering strategies to minimize these material incompatibilities. For instance, plasma treatment is a common method used specifically in microfluidics to decrease the hydrophobicity of silicones. However, the treated surfaces are not stable and often suffer from hydrophobic recovery (148). In addition, this process usually necessitates cleanroom facilities and the removal of printed structures from the printer platform, which is not favorable to our purpose of devising fully 3D printed structures. Another potential method to modify the silicone's surface and improve its wettability is graft polymerization. This process mainly involves the chemical treatment of silicone's surface, followed by initiation using different techniques, such as UV irradiation, thus generating radical sites on the surface of the silicone for further reaction with another chemical component and surface graft polymerization (149-151). Hence, we took advantage of the UV element present in the fabrication process and

employed this method that entailed the chemical treatment of the silicone surface. This method involved the application of benzophenone (BP) photoinitiator, which has been used to activate elastomer surfaces in UV assisted polymer grafting and was shown to improve the interfacial bonding of elastomer-hydrogel hybrids (129). As illustrated in Figure 3.4 (a), upon the treatment of the elastomer surface with BP and exposure to UV light, the BP molecule generates radical sites that can separate a hydrogen atom from the elastomer (149, 151, 152). The hydrogel monomer, acrylamide in this case, will then react with the generated radicals, leading to graft polymerization and chemical bonding of the hydrogel to the elastomer surface (149, 151, 152). During device fabrication, we treated the surface of the 3D printed silicone structures with aliquots of 10 wt.% BP solution in acetone. After the absorption of BP, the surface of silicone was dried using nitrogen gas and the subsequent hydrogel layers were printed while the entire structure was exposed to UV light. This method resulted in the deposition of hydrogel films with uniform surfaces on the silicone layer with improved interfacial bonding (Figure 3.4 (b)).

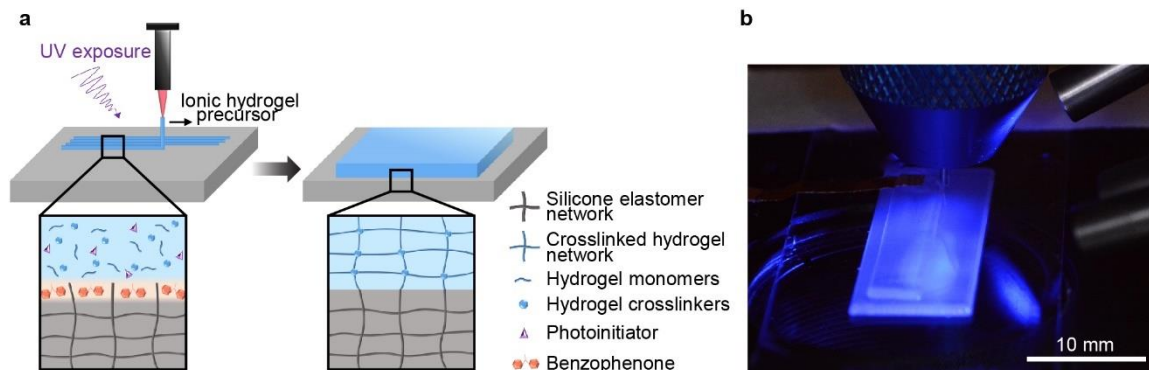


Figure 3.4. Surface treatment and 3D printing of ionic hydrogel on underlying silicone-based surface. (a) Schematic of depositing hydrogel on the surface of silicone-based layer treated with BP under UV light exposure. (b) Printing of the ionic hydrogel on the silicone-based passive layer after surface treatment with BP and under UV light.

Figure 3.5 shows the step-by-step fabrication process of DEA devices. In order to facilitate the testing of DEA actuation performance, copper tape pieces were integrated into the device structure to function as electrical contact leads. The bottom electrical lead was inserted during the printing process, prior to depositing the bottom hydrogel electrode. The top electrical lead was attached to the upper surface of the hydrogel layer after completing the printing process of the device.

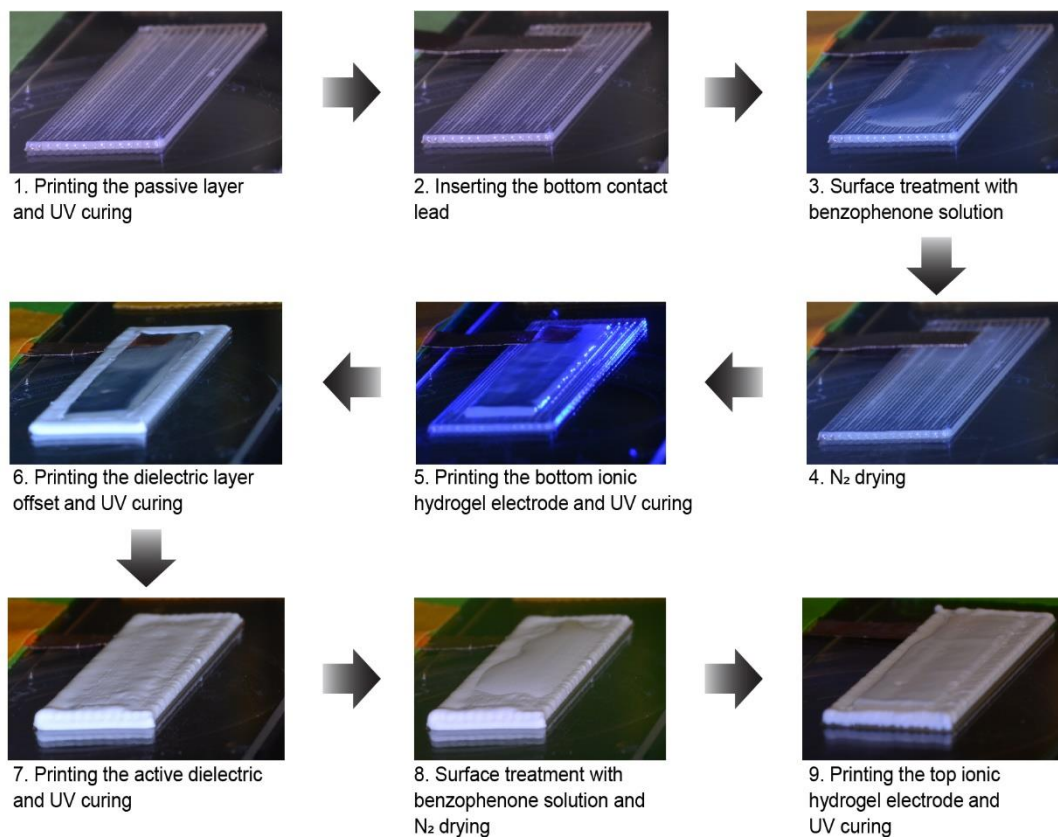


Figure 3.5. Step by step fabrication process and 3D printing of the unimorph DEA.

The final 3D printed DEA (Figure 3.6 (a)) had dimensions of ca. 30 mm × 10 mm × 1.6 mm (length × width × height). The thicknesses of the passive layer, DE layer, and hydrogel electrodes were approximated as 300 μm, 500 μm, and 380 μm, respectively, based on SEM images of the device cross section (Figure 3.6 (b)).

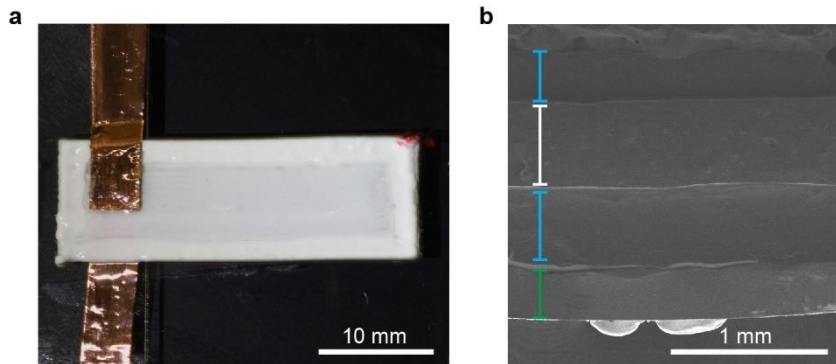


Figure 3.6. Final 3D printed DEA. (a) Top view image of the final 3D printed DEA. (b) SEM image of the DEA cross section. The green, blue, and white markers denote the passive layer, hydrogel electrodes, and dielectric layer, respectively.

3.6. DEA Performance Analytical and Finite Element Modeling

Most of the modeling efforts provided in the literature for predicting the deformation response of nonlinear soft devices tend to apply linearized approaches, which are applicable only in restrictive conditions, such as small displacements (153). Thus, linear models are inaccurate when the deflection amplitudes are higher than the thicknesses of the structures (154). The modeling approach in this study encompasses both the material and kinematic nonlinearities through the implementation of the energy formulation instead of the common force-balance method, which can become cumbersome for nonlinear systems (154). In other words, the material and kinematic nonlinearities are the impetuses for the mathematical development to capture the important energetics of the device (153). The energy formulation is an attractive approach for predicting the device actuation and response characteristics due to electrical and mechanical loads experienced simultaneously by the device. Additionally, the Rayleigh-Ritz method can be employed in conjunction with the energy formulation to obtain a solution for the deflection in the beam-like device (154). Details of the model derivation are presented in Appendix B. Briefly, the DEA

device was treated as a cantilever nonlinear Euler-Bernoulli beam. The general assumptions were: (i) static equilibrium; (ii) no slip occurs between the layer interfaces; (iii) isotropic behavior in each material layer; and (iv) zero strain at the neutral axis.

To account for the materials nonlinearities, the hyperelastic constitutive laws were incorporated into the derivations using the Neo-Hookean material model. Thus, the predictive actuation response included nonlinearities stemming from (i) the electro-hyperelastic coupling in the dielectric elastomer layer, and (ii) the hyperelastic behavior of the hydrogel and passive layers.

In order to capture the geometric nonlinearities due to the high kinematics (physical flexibility) of the device, third-order terms were included in the strain energy development using the Taylor series expansion. If w represents the transverse displacement of the device during deflection, the normalized curvature (κ) can be defined as a function of the spatial derivatives (w' and w'') of w as follows (153):

$$\kappa = w'' + \frac{1}{2}w''w'^2 \quad (1)$$

The Rayleigh-Ritz method was employed in which an assumed solution was directly substituted into the energy expressions (154, 155). Mathematically, w , can be expressed as a summation of functions from a complete, orthogonal, sufficiently differentiable function set. The advantage of using the Rayleigh-Ritz method is that a function needs to satisfy only the kinematic boundary conditions. The approximate solutions were assumed in the form:

$$w(x) = q\psi(x) \quad (2)$$

where the trial functions, ψ , are known independent comparison functions to denote the mode shapes (curvature due to deflection) of the beam and q represents the generalized coordinates.

The constitutive relation for the entire DEA system can be modeled similar to piezoelectric devices (156), which can be generally expressed as follows (157):

$$\begin{bmatrix} \mathbf{D} \\ \boldsymbol{\epsilon} \end{bmatrix} = \begin{bmatrix} e^\sigma & d^d \\ d^c & s^{\mathbb{E}} \end{bmatrix} \begin{bmatrix} \mathbb{E} \\ \boldsymbol{\sigma} \end{bmatrix} \quad (3)$$

where electric displacement, strain, applied electric field and stress vectors are denoted by vectors D , ϵ , \mathbb{E} , and σ , respectively. The dielectric layer material constants include the dielectric permittivity at a constant stress σ (e^σ), the electric displacement per unit stress at a given electric field (d^d), strain per unit electric field at a known stress (d^c), and the elastic compliance at a constant electric field \mathbb{E} ($s^{\mathbb{E}}$). It should be noted that d^c and d^d are numerically identical (157).

Using 1-axis and 2-axis notations to represent the planar directions, and the 3-axis to denote the direction along the thickness of the device, the axial stress (σ_{11}) – which includes the contribution of the electromechanical strain (Λ) and axial strain (ϵ) – can be simplified as:

$$\sigma_{11} = E_{11}[\epsilon_{11} - \Lambda] \quad (4)$$

where E_{11} represents the elastic modulus of the DE. The electromechanical strain, Λ , of the DE layer with thickness t in response to applied voltage V can be defined as (154, 156):

$$\Lambda = d_{31} \left(\frac{V}{t} \right) = \nu \frac{\epsilon_o \epsilon_r}{E_{11}} \left(\frac{V}{t} \right)^2 \quad (5)$$

The Poisson ratio, vacuum permittivity, and relative dielectric permittivity are ν , ϵ_o , and ϵ_r , respectively.

Finally, the potential energy of the DEA with length L and cross section area A can be expressed as follows (154):

$$P = \frac{1}{2} \int_0^L [\varepsilon \quad \kappa] \begin{bmatrix} EA & EI_c \\ EI_c & EI_b \end{bmatrix} \begin{bmatrix} \varepsilon \\ \kappa \end{bmatrix} dx - \int_0^L [F_\Lambda \quad M_\Lambda] \begin{bmatrix} \varepsilon \\ \kappa \end{bmatrix} dx \quad (6)$$

where EA , EI_c , EI_b , F_Λ , and M_Λ are the extensional stiffness, coupling stiffness, bending stiffness, induced force and bending moment, respectively. After substituting the assumed solution into P and applying the Euler-Lagrange method for a static condition, the governing equation for the DEA transverse displacement as a function of the generalized coordinates becomes:

$$k_{nb}q_2^3 - k_{n\Lambda}q_2^2 + k_{lb}q_2 = Q_{2,int} + Q_{2,ext} \quad (7)$$

where k_{lb} , $k_{n\Lambda}$, and k_{nb} represent the coefficients due to linear bending stiffness, nonlinear electromechanical strain, and nonlinear kinematic bending stiffness, respectively. The generalized internal, Q_{int} , and external, Q_{ext} , forces are due to the electrical potential, and external loads, respectively. The blocking force can also be defined as (154):

$$F_{bl} = \Lambda E A \quad (8)$$

The DEA actuation was also simulated using Abaqus FEM software to predict the device deflection due to a voltage ramp-up input and applied tip mass and gravitational loads. Further details on the analytical model and FEM simulation are presented in Appendix B.

3.7. DEA Performance Experimental Characterization

The actuation performance of the 3D printed DEAs was investigated in three different cases, including applied (i) ramp-up electrical input, (ii) cyclic electrical loading, and (iii) payload masses. For this purpose, one end of the device was anchored to a rigid structure, while the other end was unconstrained and free to deflect. The input voltage was delivered to the device via a custom-built electrical setup (Figure B.1 in Appendix B) connected to the copper leads. The application of high voltage stimulated the out-of-plane motion of the device. The vertical displacement of the free end of the device was obtained by analyzing the recorded actuation performance using a video analysis and modeling software (Tracker, see Appendix B for more details). First, we evaluated the performance of the DEAs in response to slowly ramping-up voltages (250 V/10 s) (Figure 3.7 (a)). As shown in Figure 3.7 (b), the DEA tip displacement was found to exhibit a quadratic relationship with the applied voltage. A maximum vertical tip displacement of 9.78 ± 2.52 mm (n=3) at ~5.44 kV was achieved, which was more than six times the thickness of the device.

In order to verify the behavior of the DEA, we simulated the actuation performance in response to an applied ramp-up voltage via analytical and FEM models. Both models illustrated similar quadratic relationships seen in the experimental results between the DEA tip displacement and the input voltage, as shown in Figure 3.7 (b). The analytical deflection results were ~41% below the experimental values. This noticeable deviation between the experimental and analytical results could be attributed to the following factors. First, the modeling was conducted for static conditions; thus, the time-dependent response and the relaxation behavior of the DEA were not considered. Second, the transverse shear effect

was ignored in the analytical model due to the simplifying assumptions in the non-linear Euler-Bernoulli beam theory (158). Finally, variations in the material properties, such as density and elastic modulus, and potential variabilities in each layer during the fabrication process may affect controlling the overall geometry and structural stiffness of the device, which will contribute to the deviations between the experimental and modeling results. In designing electromechanical transducers, it is often required to include a compensation factor to account for these variabilities (154). Thus, by comparing the analytical model with the experimental results, a compensation factor with a value of ~ 1.65 was used, which yielded an excellent fit with the experimental data (Figure 3.7 (b)). The values for E and d_{31} of the DE layer were then obtained using the model with the compensation factor and were implemented in the FEM simulation. The FEM predictions were in good agreement with the experimental results and remained within one standard deviation of the experimental data.

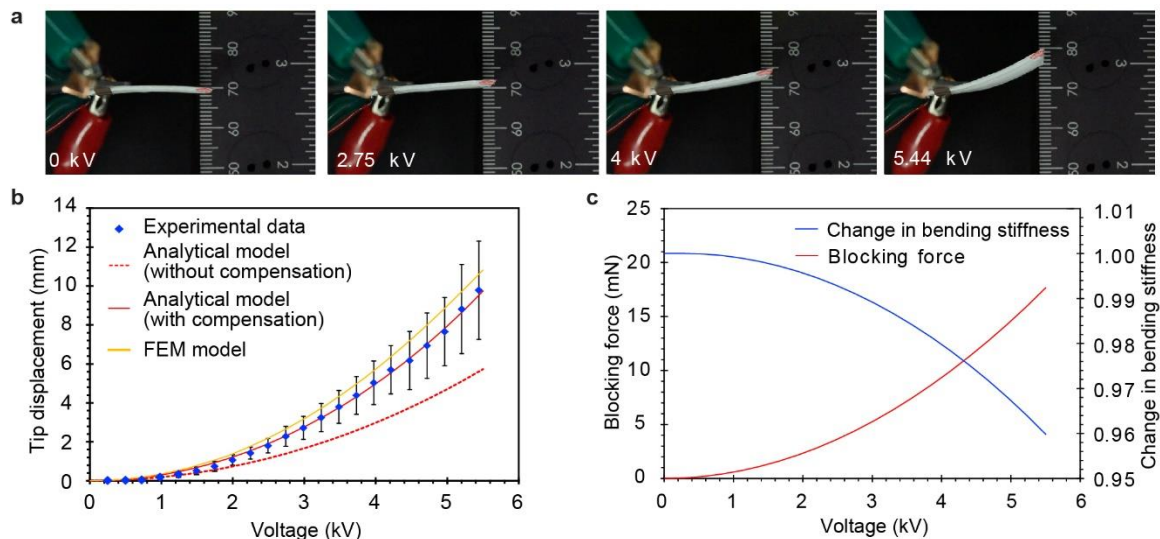


Figure 3.7. Characterization of device actuation performance in response to applied ramp-up voltage input. (a) Stills of device actuation performance at different applied voltages. (b) Experimental results during voltage ramp-up and their comparison with analytical and FEM simulation. Error bars represent standard deviation of the n samples that did not breakdown up to a specific level of the applied voltage. Specifically,

n is equal to 5, 4, and 3 for voltage ranges of 0-4.21 kV, 4.47-4.96 kV, and 5.2-5.44 kV, respectively. (c) Estimation of DEA blocking force and change in bending stiffness as a function of applied voltage using the analytical model.

The bending stiffness and blocking force of the device were estimated as functions of the input voltage (Figure 3.7 (c)). The blocking force increased due to an increase in V , reaching a value of 17.27 mN at ~5.44 kV, while the restoring bending stiffness decreased as V increased (Figure 3.7 (c)). Thus, the device became more compliant when the voltage increased. Using the approximation $\frac{F_{b1}W}{2m}$ (159, 160) (where m represents the mass of the device), a maximum energy density of ca. 0.13 J kg⁻¹ and efficiency of ca. 30 % were estimated for the unimorph DEA.

We also tested the repeatability and time-dependence of the device performance by applying a cyclic electrical load via a square-wave input voltage with a constant amplitude of 4 kV (Figure 3.8 (a)). The results showed that the DEAs exhibited a time-dependent response to step changes in the applied voltage from 0 to 4 kV (and vice versa), which was found to be consistent with previous reports on the performances of unimorph DEAs (140, 156). A rise time of 1.85 s was approximated for the device response at a frequency of 0.05 Hz. In addition, a slight drift in the device displacement over consecutive cycles of stimulation was observed, which was more prominent at the beginning and diminished after the first few cycles. These time-dependent characteristics of DEA performance have been attributed to the relaxation behavior of dielectric elastomers (161, 162), and the electrical dynamics of the device during capacitive charging and discharging (142, 163). Nevertheless, the peak-to-peak amplitude of the DEA displacement remained consistent over the actuation cycles, confirming the repeatability of the device performance.

Furthermore, we investigated the effect of oscillatory inputs on the deflection amplitude and rise time of the device (Figure 3.8 (b)). The effect of changes in frequency on device displacement was found to be trivial for frequencies below 0.1 Hz, while the rise time decreased with an increase in frequencies in this range. For oscillation frequencies above 0.1 Hz, a significant decrease in the device deflection and a relatively constant rise time were observed.

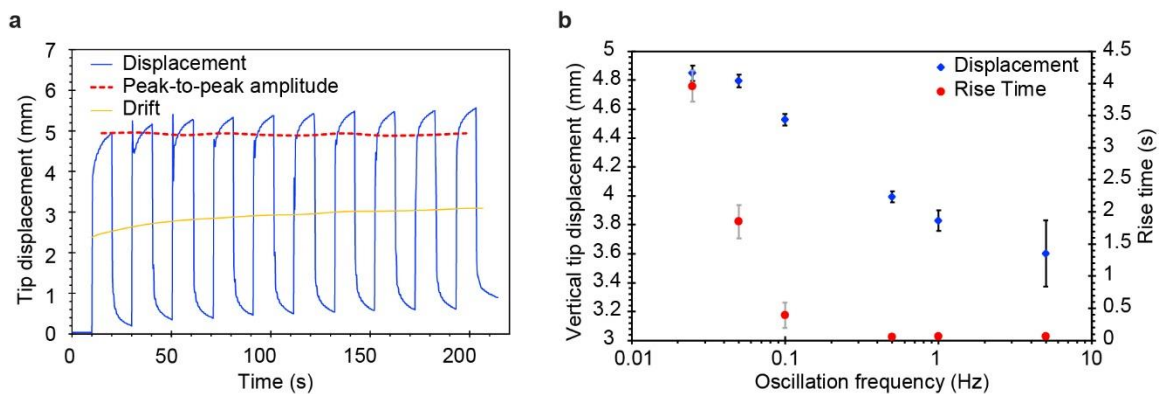


Figure 3.8. Characterization of the time- and frequency-dependent performance of the DEAs. DEA performance in response to square wave voltage input with an amplitude of 4 kV and frequency of ~ 0.05 Hz. (b) Effect of changes in the frequency of the square-wave input on DEA displacement and rise time.

The impact of dielectric thickness on the device actuation performance was also investigated using the analytical model. As shown in Figure 3.9, decreasing the thickness of the DE layer could yield higher device deflections at lower applied electric fields. However, it should be noted that this could entail a tradeoff via an increase in the probability of dielectric breakdown.

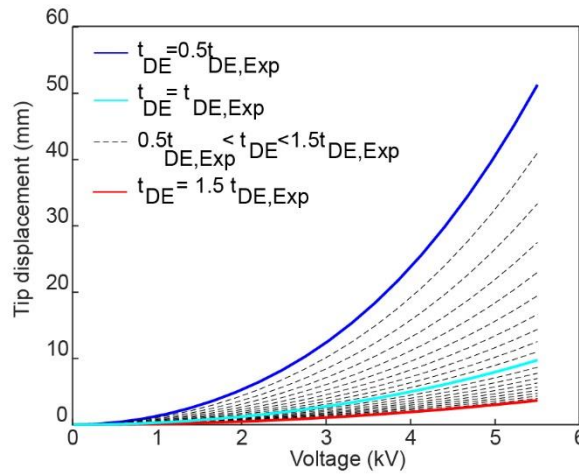


Figure 3.9. Effect of changing the DE thickness on device actuation performance.

Finally, we evaluated the DEA load lifting capacity by mounting payload masses of 0.04, 0.08, and 0.12 g on the tip of the device and obtaining the displacement of the tip mass against gravity upon the application of voltages ranging from 0.250 to 5 kV (Figure 3.10). At an input voltage of 5 kV, increasing the tip mass from 0 to 0.12 g reduced the maximum tip deflection from 2.80 to 0.85 mm. We also compared the experimental data for the DEA performance in response to an applied payload mass with results obtained from FEM. In general, the FEM simulations were consistent with the experimental trends and were in good agreement for tip masses with values of 0, 0.04, and 0.08 g (Figure 3.10 (b, c)). For the case with a tip mass of 0.12 g, a higher deviation between the experimental and FEM maximum displacement was observed. A possible explanation involves the relative shift in the radius of gyration due to the mounting of the increased mass on the tip of the device.

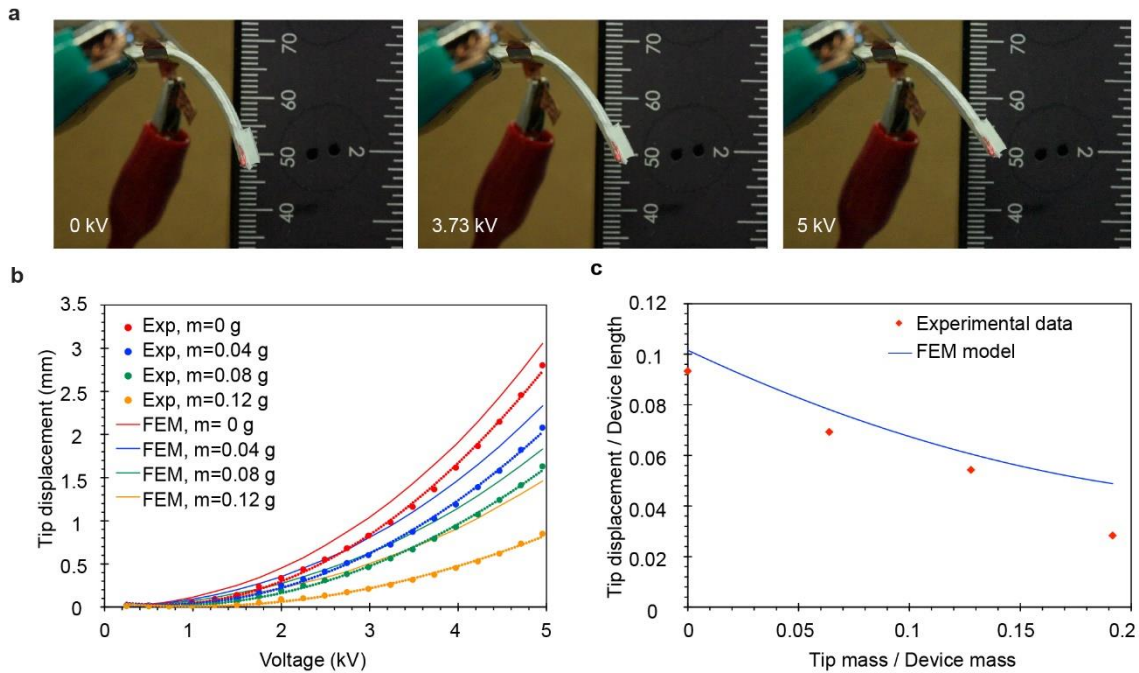


Figure 3.10. Characterization of DEA performance in response to applied tip masses. (a) Stills of DEA performance in lifting a tip payload mass of 0.04 g at different applied voltages. (b) Effect of different tip mass values on device performance and comparison with FEM simulation. (c) Plot of normalized maximum tip displacement as a function of normalized tip mass for experimental and FEM results (right).

3.8. Ionic Hydrogel-Elastomer Hybrids as Sensors

As discussed earlier, the basic configuration of dielectric elastomers can be used in the reverse mode of transduction and convert mechanical stimuli to electrical signal, thus serve as a sensing element in different application areas. For instance, previous studies have shown that the ionic hydrogel-elastomer hybrid structure can function as a capacitive sensor for tactile sensing and kinesthetic feedback (130, 131). It has also been discussed that capacitive sensors are superior over other types of electrical sensors in terms of high precision, sensitivity and resolution, temperature-independent and drift-free sensing in long runs, and simplicity and robustness of structure (130).

Upon the application of external pressure to the sensor, the dielectric elastomer experiences a deformation (compression of thickness and expansion in area), which results

in a change in device capacitance ($C_D \sim \frac{A}{d}$). Measuring the change in capacitance of the device can be harnessed to sense the applied pressures.

In the sensing mode, the same principles apply that were discussed earlier for the case of actuation. Specifically, the difference in the order of magnitude of the capacitance between the electrical double layer (EDL) and the dielectric layer prevents electrochemical reaction. In addition, since $C_{EDL} \gg C_D$, when the capacitance C (which is the equivalent of the three capacitors in series, i.e.: $1/C = 2/C_{EDL} + 1/C_D$) is measured between the two electrodes during the tests, the measurement is primarily governed by the capacitance of the dielectric layer, therefore $C \sim C_D$ (130).

We adapted a similar strategy to 3D print a soft capacitive sensing unit based on the ionic hydrogel-elastomer hybrids. The sensor consisted of two layers of polyacrylamide-based ionic hydrogel as the electrodes and a silicone-based dielectric elastomer as the electroactive component of the sensor (Figure 3.11 (a)). We also added silicone layers on the top (cover layer) and bottom (base layer) of the device to facilitate its handling and longevity (Figure 3.11 (a)). The composition of the ionic hydrogel was the same as the formulation discussed earlier in this chapter. The composition of the dielectric elastomer used in fabrication of the sensing unit comprised of the high molecular weight silicone sealant (Loctite® 5039™ Nuva-Sil®) and the two-part silicone elastomer (Wacker SEMICOSIL® 912 as the base and ELASTOSIL® CAT UV as the catalyst with a 10:1 mixing ratio) at a 3:2 weight ratio (131). A 1 cm × 1 cm sensor device was printed by alternately depositing layers of the two different materials, followed by their photopolymerization via UV exposure (Figure 3.11 (b)). As discussed before, to facilitate

the testing of the devices, copper tape was used as electric contact leads and was inserted into the device during the printing process. Specifically, the first copper lead was inserted after printing the first silicone layer (base) and prior to deposition of the bottom hydrogel electrode, and the second copper contact lead was inserted after printing the top hydrogel electrode and prior to depositing the top silicone encapsulation (cover). Indeed, to facilitate the uniform printing of the hydrogel on the hydrophobic surface of the silicone, we treated the underlying silicone surface with 10 wt. % solution of benzophenone in acetone. The final 3D printed device has dimensions of ca. 10 mm × 10 mm × 1.2 mm (length × width × height).

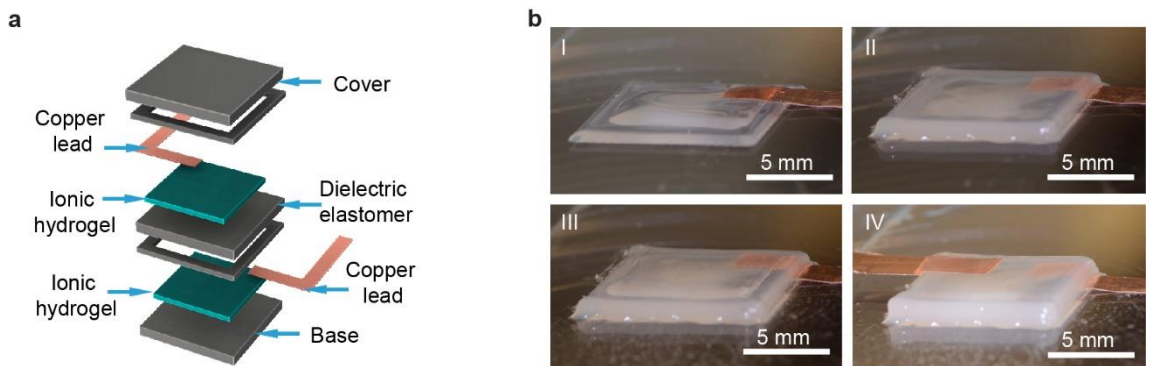


Figure 3.11. Structure and fabrication process of the 3D printed soft capacitive tactile sensor based on ionic hydrogel-elastomer hybrids. (a) Schematic of the structure and components of the soft tactile sensor. (b) Step-by-step 3D printing of the soft tactile sensor.

The 3D printed sensor was calibrated by applying different pressures to the device and measuring the changes in the capacitance. For this purpose, a cylindrical metal bar was mounted on a vertical axis of a nanopositioning stage (ANT130-L-ZS, Aerotech) to apply cycles of press-release to the device by varying the vertical position of the bar to obtain different values for the applied forces. The applied forces were recorded using a digital scale with a flat surface which was placed underneath the sensor. The applied pressure

values were then calculated by dividing the recorded forces by the sensor area before deformation. In addition, the sensor was connected to a characterization system (B1500A, Agilent Technologies) to observe the changes in device capacitance at each of the press-release cycles. A calibration plot was obtained for the sensor based on the capacitance changes at each applied pressure. As shown in Figure 3.12 (a), the capacitance changes and the applied pressure showed a linear correlation at a pressure range of 20 to 120 kPa for the sensor with this configuration. This calibration data can be used to calculate the pressure applied to the tactile sensor via corresponding changes in capacitance. In addition, the sensor exhibited repeatable response in terms of capacitance change under applied pressure during consecutive cycles of press-release with 50 kPa of applied pressure (Figure 3.12 (b)).

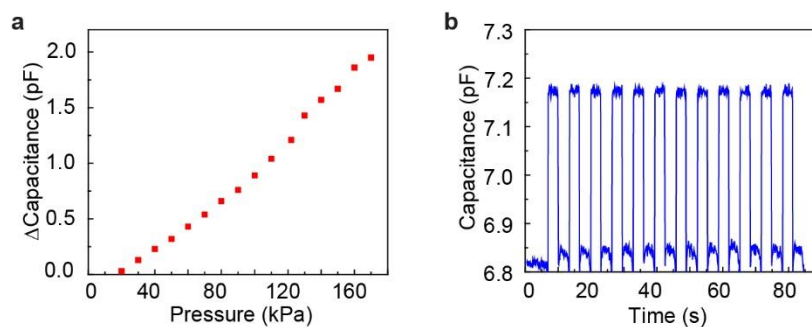


Figure 3.12. Characterization of the 3D printed capacitive sensor in response to applied pressures. (a) Calibration of the 3D printed sensor based on the correlation between capacitance change and the applied pressure. (b) Changes in capacitance of the device in response to applied cyclic pressures of 50 kPa.

3.9. Proof of Concept Demonstration: Integrated DE Sensor on 3D Printed Prostate Model

To explore the applicability of this soft tactile sensor for incorporation onto the 3D printed organ models with the purpose of obtaining quantitative feedback, we conformally integrated a 3D printed soft tactile sensor on the surface of the 3D printed prostate model

as a proof-of-concept demonstration. We designed and conducted quantitative surgical rehearsal applications using the 3D printed prostate model with the integrated 3D printed sensor. For each application, we applied three quick press-release and three press-hold-release cycles using either a finger or surgical and diagnostic tools on the sensor. The signal responses of capacitance change of the sensor were then translated into the values of applied pressures to the model using surgical/diagnostic tools via the obtained calibration plot discussed in the previous section.

For the first application example, we integrated the sensor on the outer surface of the model. Then we applied finger pressing, a surgical grasper, and surgical scissors to the sensor and deduced their corresponding pressure responses from the capacitance changes (Figure 3.13). For the second application example, we integrated the sensor on the urethra surface of the model. Then, we used an endoscope, surgical grasper and surgical scissors on the sensor and deduced their corresponding pressure responses from the capacitance changes (Figure 3.14). For each case, the real-time capacitance changes of the sensor during the interventions were recorded as shown in in Figures 3.13 and 3.14. These applications demonstrate the utility of the organ models with integrated sensing capability in training medical professionals to quantitatively realize and control the amount of applied pressure and its duration within reasonable ranges before operating on patient organs.

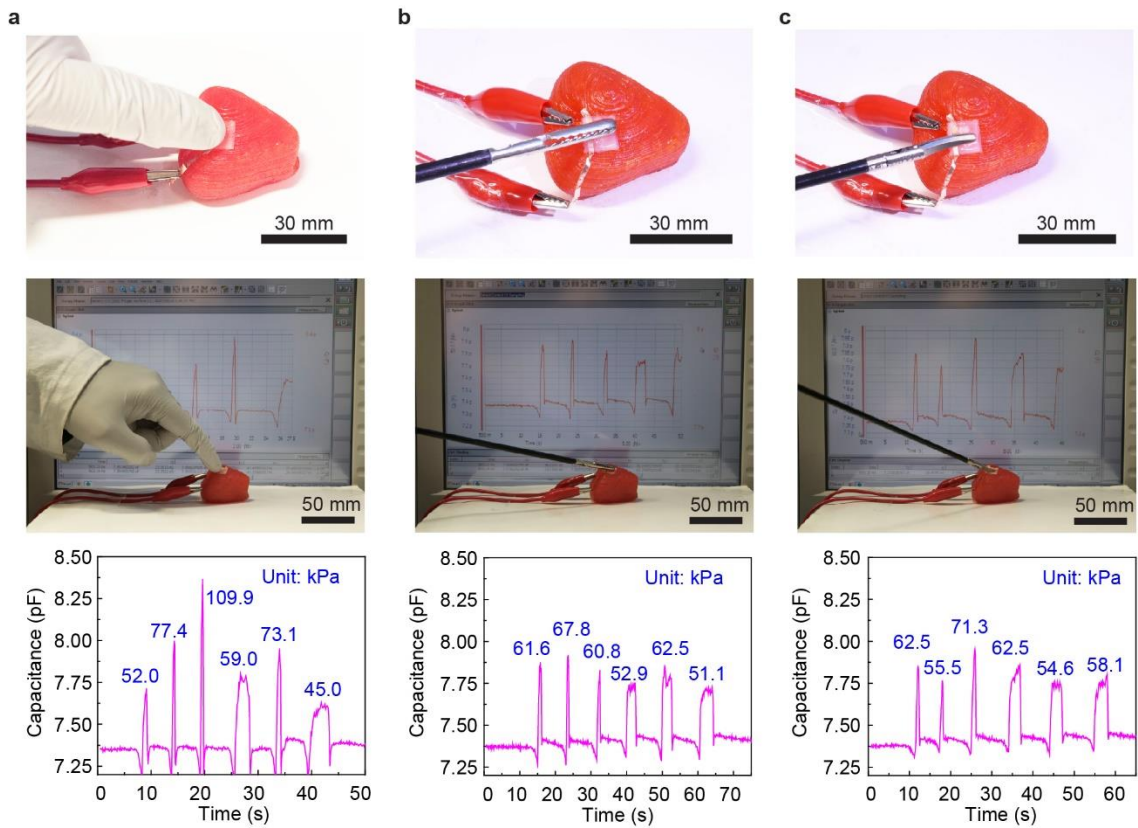


Figure 3.13. Proof-of-concept demonstrations with integration of the soft capacitive sensor on the outer surface of the 3D printed prostate model. Quantitative surgical rehearsal on the 3D printed prostate model upon applying (a) a finger press, (b) a surgical grasper, and (c) surgical scissors, respectively.

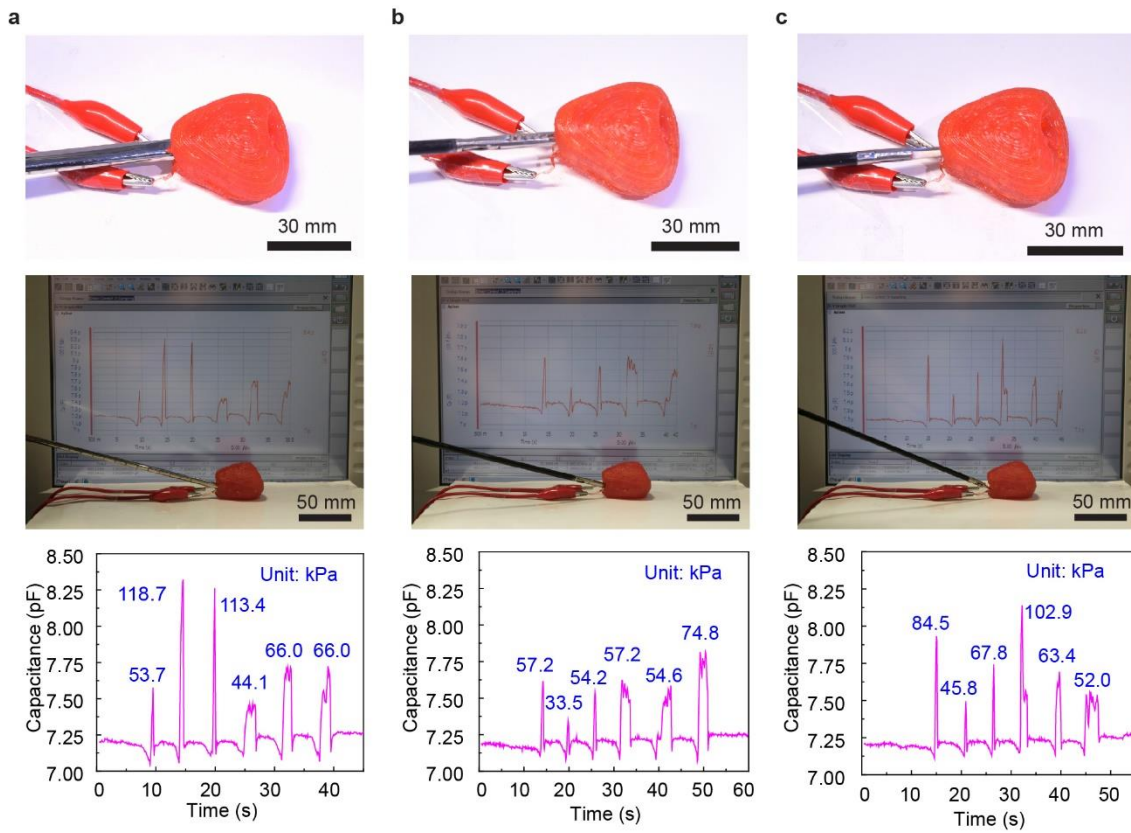


Figure 3.14. Proof-of-concept demonstrations with integration of the soft capacitive sensor on the urethra surface of the 3D printed prostate model. Quantitative surgical rehearsal on the 3D printed prostate model upon applying (a) an endoscope, (b) a surgical grasper, and (c) surgical scissors, respectively.

3.10. Development of Planar Sensor Array

The capability to visualize the pressure distribution and determine the locations with critical pressure values can be an important metric for many application areas. To this end and with the final goal of internal and monolithic integration of the sensor into the 3D printing of tissue-like organ models, we explored the fabrication of a sensor array based on the concepts discussed earlier.

As depicted in Figure 3.15 (a), the design of the 3×3 capacitive pressure sensor array includes two sets of channels (cross section area of ca. $2 \text{ mm} \times 0.480 \text{ mm}$ (width \times height)) which construct the top and bottom electrodes of the device and are separated with a ~ 600

μm -thick dielectric layer. At the crossing junction of these channels, a sensing element with area of $2\text{ mm} \times 2\text{ mm}$ is formed. Each sensing element is identified as “element xy ” where x and y represent the row and the column of the element in the array, respectively (Figure 3.15 (a)). The planar sensor array was 3D printed by using the silicone-based tissue mimicking ink (ratio of bulking to active agent: 0.85) for the device main structure (dielectric and encapsulation layers). After printing and curing of the silicone structure, the channels were filled by injection of an aqueous solution of the ionically-conductive hydrogel, comprising of acrylamide monomer dissolved in an 8 M lithium chloride stock solution with ratio of 15.64:100 (w:v), as well as N,N'-methylenebisacrylamide crosslinking agent and 2-hydroxy-2-methyl-propiophenone photoinitiator with ratios of 0.00064:1 and 0.00543:1 with respect to the weight of acrylamide monomer, respectively. After filling the electrode channels, the device was exposed to a UV system for photopolymerization and curing of the ionic hydrogel (Figure 3.15 (b)). Prior to testing the devices, wires were inserted to the channels to facilitate the electrical connections for testing.

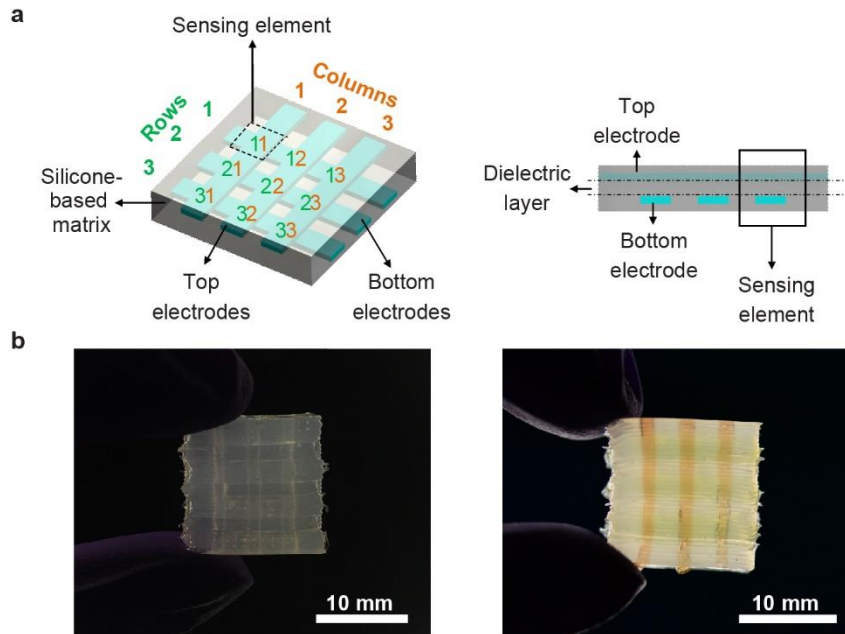


Figure 3.15. Design and structure of the sensor array. (a) Schematic of the 3×3 sensor array design and used notations for identifying the elements. (b) 3D printed sensor array with hollow (left) and filled (right) channels with the ionic hydrogel (orange and green dyes have been added to the ionic hydrogel for visualization of the two channel sets).

To characterize the 3D printed sensor array, first, we calibrated the sensing elements by applying different pressures and measuring the changes in the capacitance of each element using a customized test bar with a rectangular tip with dimensions of $2 \text{ mm} \times 2 \text{ mm}$ (corresponding to the area of sensing elements). A calibration plot was obtained for each of the elements in the sensor array based on the capacitance changes at the applied pressure values (Figure 3.16 (a)). Averaging the results for all the nine sensing elements yielded a cumulative calibration plot for the device with the slope of the linear fit representing the sensitivity of the device (ca. 0.0023 1/kPa) (Figure 3.16 (b)).

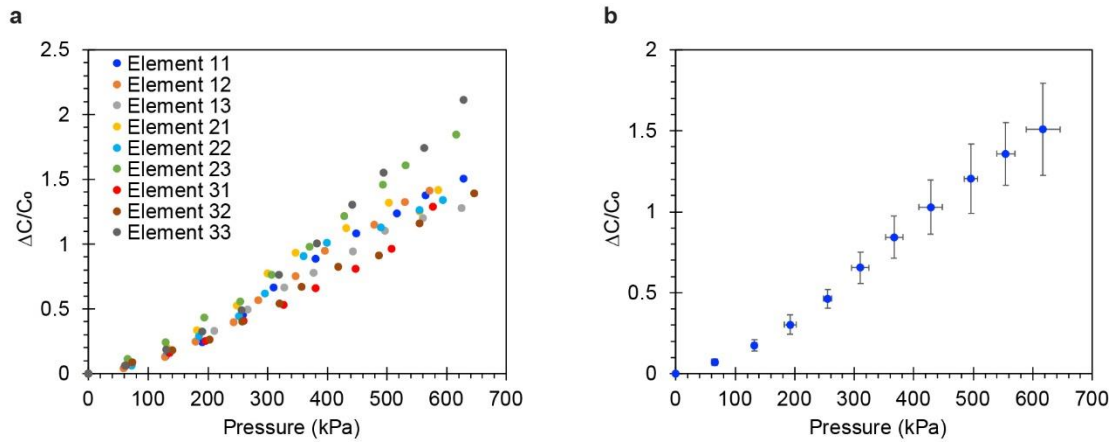


Figure 3.16. Calibration of the sensor array. (a) Calibration data for individual sensing elements in the array. (b) Cumulative calibration plot for the sensor array resulted from averaging the data for the 9 sensing elements.

To investigate the possibility of crosstalk between adjacent elements in the sensor array, we pressed a specified sensing element (for example element 11, element 21, and element 22) and measured the changes in the capacitance of all the nine elements in each case. As it can be seen in Figure 3.17, the obtained heatmaps indicated the corresponding location of the applied pressure with trivial crosstalk between adjacent pixels. Specifically, for cases of pressing on elements 11, 21, and 22, capacitance changes of 55.39%, 71.45%, and 67.46% were obtained for these pressed elements, while the maximum capacitance changes for the eight other elements were 10.69%, 12.00%, and 11.34% in each case, respectively. This verified that this sensor array design can be implemented with minimal interference impact among measured signals from adjacent elements in the array, hence can be used to detect the location of applied pressures.

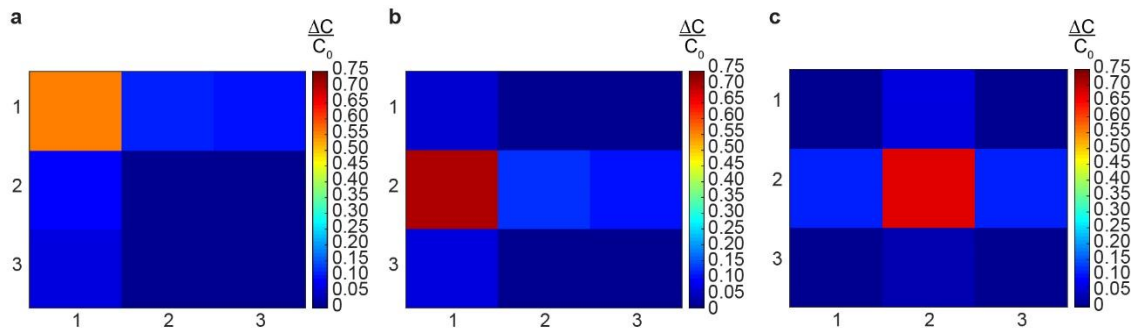


Figure 3.17. Investigating the crosstalk between adjacent elements in the sensor array. Heatmaps of normalized capacitance change obtained while pressing (a) element 11, (b) element 21, and (c) element 22.

Finally, as another demonstration to capture the capability of the sensor array for determining the location of the applied pressure, we used the device in an object detection application. As shown in Figure 3.18, a rectangular-shaped and a cross-shaped object were pressed on the sensor array. The corresponding discrete and continuous heatmaps (which were obtained by linear interpolation) in each case were able to correctly indicate the geometry of the test bar, as well as the location of pressure application.

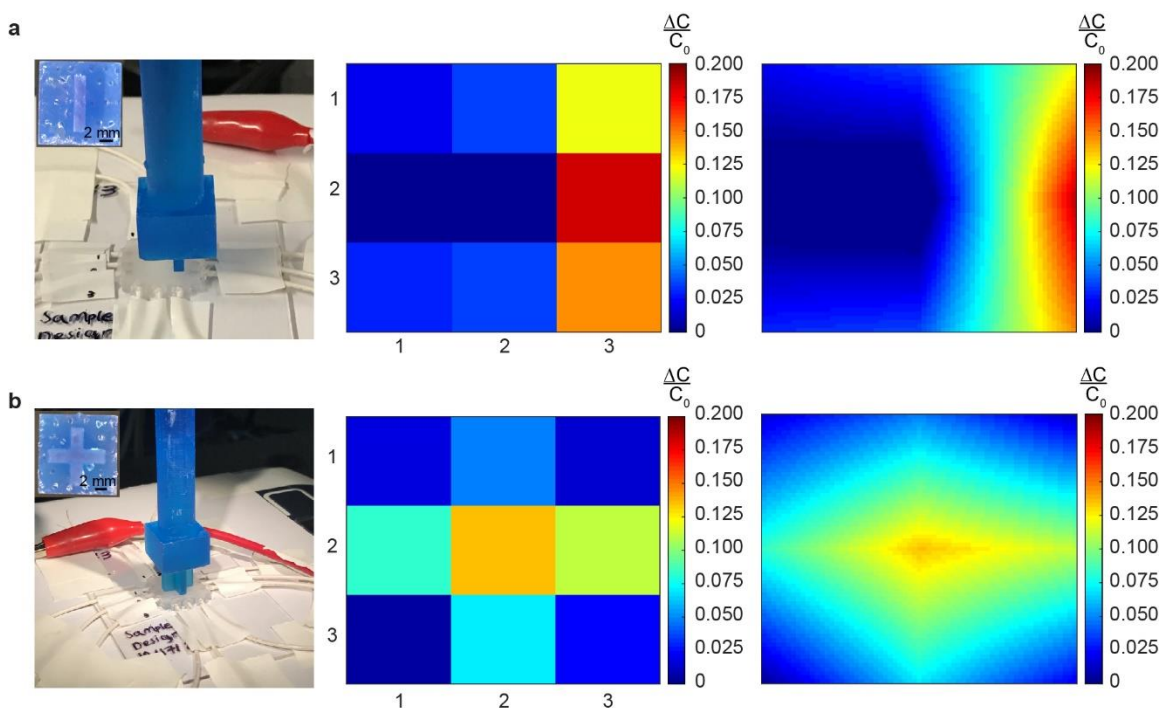


Figure 3.18. Object detection experiments with the 3×3 sensor array. Heatmaps of normalized capacitance change obtained while pressing (a) a rectangular-shaped object on column 3 of the array, and (b) a cross-shaped object centered on the array.

3.11. Conclusion

In this chapter, the design and development of soft electromechanical transducers based on ionic hydrogel-elastomer hybrids have been discussed. Specifically, it was demonstrated that this hybrid material structure can be applied for 3D printing of soft dielectric elastomer actuators that can generate bending modes of motion in response to applied electrical stimuli. This involved the selection and optimization of materials for performance and printability, solving key material integration challenges, and fabrication and characterization of the final devices. Several strategies can be incorporated with the goal of improving the performance of the current devices to achieve higher spatial range and temporal rate of actuation at lower applied electric fields, thus broadening their range of applications in various areas, including but not limited to soft robotics. For instance,

given that the device performance is more sensitive to variations in the thickness of the active DE layer, decreasing the thickness of this layer (for example, via using finer nozzles during the printing process) could enhance the device deflection, but entails a tradeoff via an increase in the probability of dielectric breakdown. Hence, surface modification of the barium titanate nanoparticles could be considered to improve the dielectric properties and electromechanical strength of the DE/BaTiO₃ composites (164). Furthermore, stacking multiple layers of active DE membranes, which is readily achievable using a 3D printing process, can be employed as a method to enhance the device actuation performance (165).

In addition, it was shown that the same strategy can be applied to 3D print a soft capacitive tactile sensor. As a proof-of-concept demonstration, the 3D printed sensor was conformally integrated on the tissue-like prostate model and was used to provide quantitative feedback during handling the organ model with surgical/diagnostic tools. This feedback can be used as an indicator of surgical performance and can provide medical professionals with the ability to quantify and control the pressure ranges they apply to the organ during preoperative rehearsal and training.

Finally, the design, 3D printing, and characterization of a sensor array using the custom-formulated tissue-mimicking ink as the dielectric and encapsulation layer was discussed. In the next chapter, the design and development of this planar sensor array will be translated to an internally-integrated sensor array within the structure of a 3D printed organ model.

Additional details on experimental methods, materials, and other supplementary information for this chapter is provided in Appendix B.

CHAPTER 4[†]

Functional 3D Printed Aortic Root Models with Internal Sensors for Minimally Invasive Applications

[†]The work reported in this chapter is in preparation for publication.

4.1. Introduction

In the coming decades, the world will be facing a shift in demographics and aging of its population. For example, it has been estimated that by the year 2030, the number of adults over the age of 65 years old in the United States alone, will reach 73.1 million, comprising 21% of its total population (166). An aging population results in an increase in the prevalence of cardiovascular diseases, which is the leading cause of death in this age group (167). Non-congenital aortic stenosis (AS) is one of the common cardiovascular conditions in the elderly that affects about 2.7 million adults over the age of 75 in North America (168). AS is associated with the narrowing of the aortic valve as a result of its calcification, which impedes the leaflets full motions, causing an obstruction to the blood flow from the left ventricle to the aorta and ultimately, ventricular dysfunction (169). Given the age of the individuals suffering from AS and the prevalence of comorbidities in this population, some patients are deemed high risk for surgical valve replacement via open heart surgery (169, 170). Transcatheter aortic valve replacement (TAVR) is a minimally invasive procedure aimed at treating this disease by implanting a prosthetic valve within the damaged native valve via a catheter delivery system (169). Like any medical procedure, TAVR can be subject to postoperative complications among which are paravalvular leak and/or conduction disturbances. Paravalvular leak (PVL) is caused by an insufficient seal and presence of gaps between the prosthetic valve frame and the native aortic annulus and leads to regurgitation of blood flow from the aorta to the left ventricle (171). Post-TAVR conduction disturbances can be triggered by the pressure imposed on the critical region below the aortic root in proximity to the atrioventricular (AV) conduction pathway by the

replacement valve frame (Figure 4.1) (172). This critical region is identified as the lower limit of membranous septum where the His bundle emerges into the left bundle branch (Figure 4.1) (172-175). Applied pressure on this region can result in left bundle branch block or atrioventricular block and thus, the need for permanent pacemaker implantation (172-175).

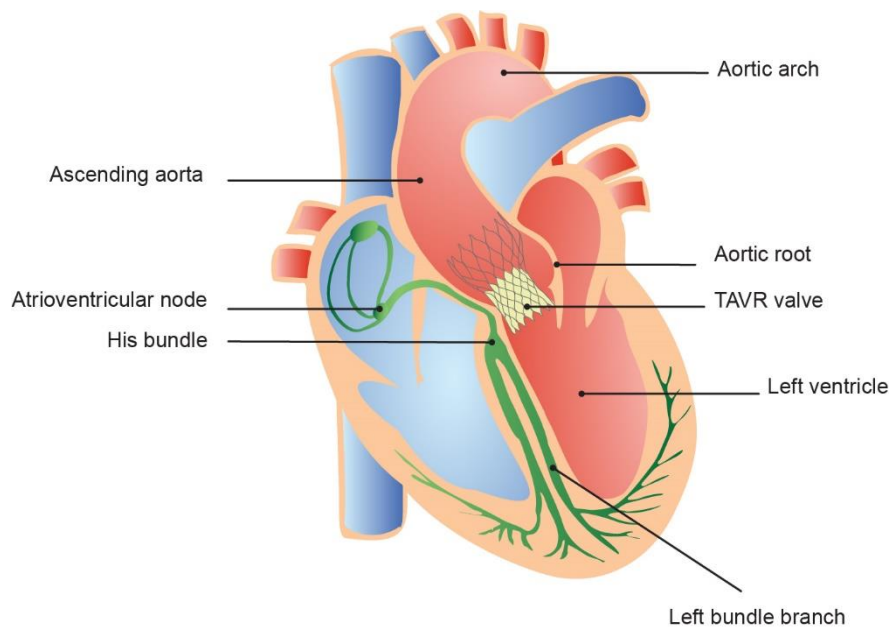


Figure 4.1. Schematic of the heart and its conduction pathway (shown in green) with implanted TAVR prosthesis in the aortic root region.

Several different factors related to a given patient's anatomy, the procedure, and the prosthetic valve can contribute to post-TAVR complications, including membranous septum length, septal wall thickness, calcification patterns, patient-prosthesis size mismatch, implantation depth, mispositioning, and type of the prosthetic valve (172, 175-182). Therefore, the proper selection and optimization of the interplays among these factors based on each patient's unique anatomical features are vital in TAVR planning to mitigate the risk of postoperative complications and mortality.

Compared to surgical aortic valve replacement where surgeons can have direct access to the aortic root anatomy and resect the native calcified valve, the minimally invasive nature of the TAVR can potentially raise the levels of challenge in terms of full visualization of the anatomical features and their interaction with the prosthetic valve (181). Currently, most of the decision-making process in TAVR, which includes choosing the right size, implantation depth, and positioning of the prosthetic valve, occurs based on measurements derived from pre- and intra- procedural imaging; hence it increases the dependency on clinician's experience and skills, and the chance for postoperative complications (181). Alternatively, utilizing 3D printed patient-specific, organ models could significantly enhance the 3D visualizations and augment the understanding on the physical interaction of the prosthetic valve with the patient's native anatomies, therefore improving preprocedural planning (21, 183, 184).

Previous efforts on utilizing 3D printed aortic root models for TAVR were mainly focused on exploring the applications of these models for preprocedural prosthetic fit-testing, evaluation of patients' anatomical features and/or hemodynamic studies for prediction of paravalvular leak (21, 184-188). Most of these previously reported models were 3D printed using a single rubber-like commercial photopolymer for mimicking the tissue components of the aortic root structure (including the left ventricle outflow tract, leaflets and the aorta) and a rigid one for replicating the calcified lesions on the leaflets (21, 184-188).

In this chapter, the concepts and methodologies discussed earlier were combined to develop patient-specific models of the aortic root with internal sensor array tailored for

applications in TAVR, as an example of minimally invasive procedures. Specifically, a customized, multi-material 3D printing process was implemented for fabrication of patient-specific models of the aortic root that are made using three different materials with properties commensurate to: 1) aorta; 2) myocardium and leaflets; and 3) calcified regions. These models can provide a “more realistic” representation of patient’s anatomy for preprocedural planning and decision making on prosthesis and procedure parameters, flow studies, evaluation of patient- and disease-specific hemodynamic parameters, and investigation on the possibility of paravalvular leak occurrence. Furthermore, uniquely here we demonstrate the internal integration of a sensor array within the anatomical structure, which can be used to visualize the contact pressures in the critical region of the aortic root anatomy, thus providing the physicians with a benchtop tool with further understanding of the valve deployment and thus, mitigating some of the risks of post-TAVR conduction abnormalities.

4.2. Material Selection and Model Fabrication

To initiate the 3D printing process, we obtained the computed tomography (CT) scans of the patients’ cardiac anatomy, segmented these images to extract the regions of interest, and then generated the stereolithography (STL) file for the 3D printing process (Figure 4.2). As depicted in Figure 4.3, the models consist of aortic wall, a portion of myocardium, the leaflets, and the calcified regions which were 3D printed simultaneously using customized materials, i.e. those that mimic the mechanical properties of their biological counterparts. Hence, optimizing the formulation of the customized polymeric 3D printing materials was a fundamental step in the fabrication of these aortic root models.

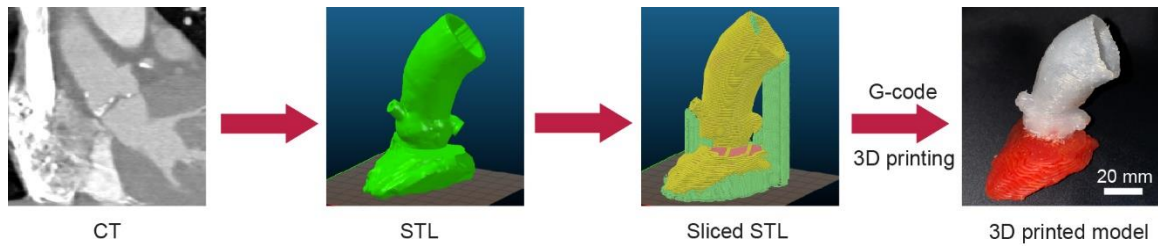


Figure 4.2. Process for generating the G-Code for 3D printing of the patient-specific aortic root model.

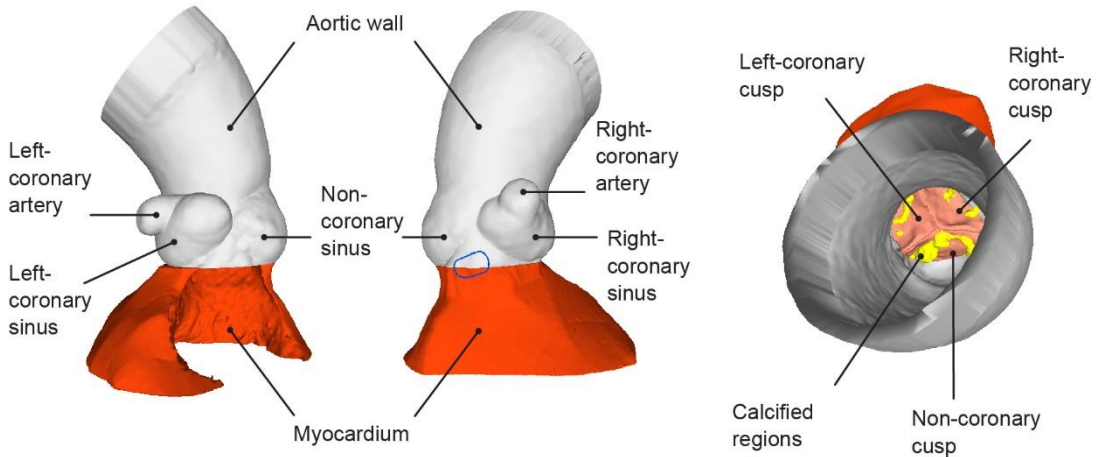


Figure 4.3. Different components of the aortic root model (The calcified regions are shown in yellow and the approximate region of membranous septum is indicated with the blue marking).

We compared the mechanical behaviors of the custom-formulated polymeric materials discussed in Chapter 2 with tissue specimens of human hearts to select proper formulations for mimicking the properties of myocardium and aortic wall. In general, the mechanical properties of the soft tissues can have significant variations depending on different factors, including: the subject, age of the subject, disease state, location/orientation of tissue excision, and the test parameters (189). For the purpose of this study, we compared the stress-strain curves of representative tissue samples from human aortic wall and myocardium to the printed samples of the inks with different formulations. It was observed that at small strain range (0~0.05), the customized polymeric inks 1 and 2 corresponding to formulations with weight ratios of bulking agent to active agent of 1.15 and 0.85 matched

the general trends of stress-strain curves of human myocardium tissue samples 1 and 2, respectively (Figure 4.4 (a)). The Young's moduli (<3% strain) for representative samples of inks 1 (109.3 kPa) and 2 (156.2 kPa) were analogous to myocardium tissue samples 1 (105.3 kPa) and 2 (146.4 kPa). At the same strain range (0~0.05), the customized polymeric inks 3 and 4 with bulking to active weight ratios of 0.70 and 0.25 matched the trends of stress-strain curves of human aortic tissue samples 1 (without calcification) and 2 (with calcification), respectively (Figure 4.4 (b)). The Young's moduli (<3% strain) for representative samples of inks 3 (240.3 kPa) and 4 (493.5 kPa) were analogous to aortic tissue samples 1 (216.1 kPa) and 2 (586.5 kPa). At higher strain ranges, a divergence was observed in the stress-strain curves of polymeric materials compared with tissue specimens, which was more significant for the aortic tissue (Figures 4.4 (a) and (b)). This divergence was mainly due to the strain-stiffening behavior of soft tissue structures as a result of collagen fiber alignments and straightening along the load direction at higher strains (190). Nevertheless, the modulus values of our developed materials and tested myocardium and aortic tissue were in accordance with the range of moduli previously reported for myocardium (12-273 kPa) (191, 192) and aorta (334-1,817 kPa) (193, 194) (Table C.1 in Appendix C).

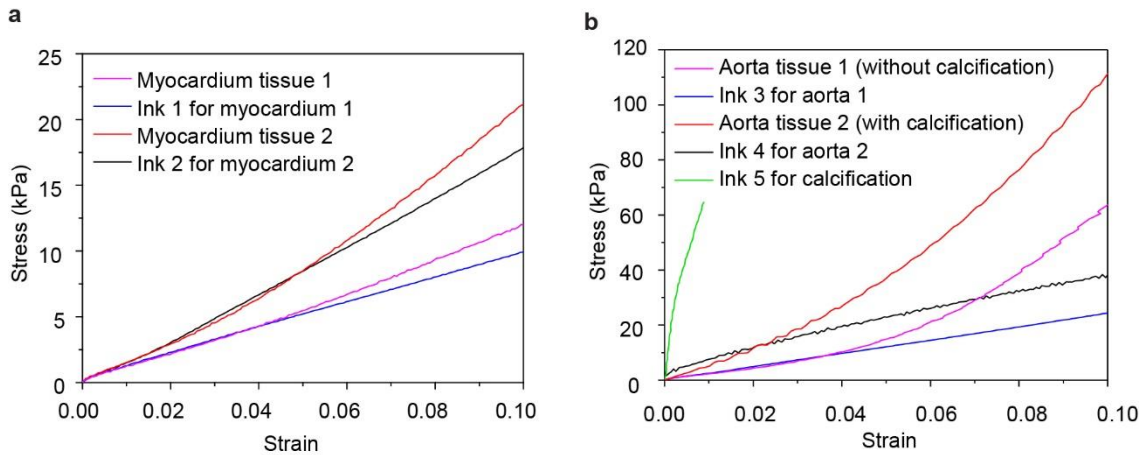


Figure 4.4. Stress-strain plots of custom-formulated polymeric materials and tissue specimens. (a) Stress-strain plots of myocardium tissue specimens and corresponding polymeric materials. (b) Stress-strain plots of aortic tissue specimens and corresponding polymeric materials, as well as the calcification material.

Besides, we used a spackling material (ink 5) for printing the calcified lesions on the leaflets due to its good printability and comparable mechanical properties to aortic valve calcification. This material mainly comprised of calcium carbonate which was verified by the prominent absorption peaks of CO_3^{2-} at $\sim 712 \text{ cm}^{-1}$, $\sim 875 \text{ cm}^{-1}$, and $\sim 1425 \text{ cm}^{-1}$ observed in its FTIR spectra as shown in Figure 4.5 (195). The Young's modulus of the calcification material was estimated as $11.8 \pm 3.1 \text{ MPa}$ (Figure 4.4 (b)), which was close to the reported values of $22.6 \pm 9.2 \text{ MPa}$ for calcified aortic valve regions (196).

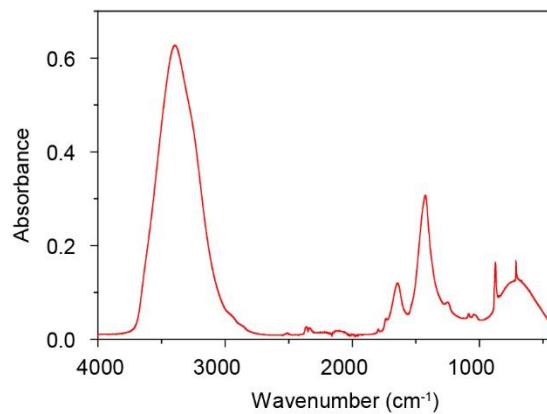


Figure 4.5. FTIR plot of the calcification material.

4.3. Model Fidelity Analyses Compared to Patient's Data

After 3D printing the patient-specific aortic root model, quantitative surface comparisons were conducted to evaluate the anatomic fidelities between the model and the corresponding patient's aortic root anatomy via 3D registration technique (120). The anatomical information of the patient's aortic root was extracted from the CT scans. The corresponding 3D printed aortic root model was also scanned by CT, and then the CT image stack (Figure 4.6 (a)) was utilized to reconstruct an STL model. A calibrated distance map (Figure 4.6 (b)) and a histogram of the calibrated distances (Figure 4.6 (c)) were generated from the overlaid 3D printed structure and the corresponding patient's aortic root geometry as the template. The results indicated that most of the calibrated distance points scatter from -3 to 3 mm, with peaks close to 0 mm (Figures 4.6 (b) and (c)). The fractions of voxels of the 3D printed model within 5 mm, 3 mm, and 1mm of the patient aortic root geometry were found to be 91.3%, 78.9% and 43.6%, respectively.

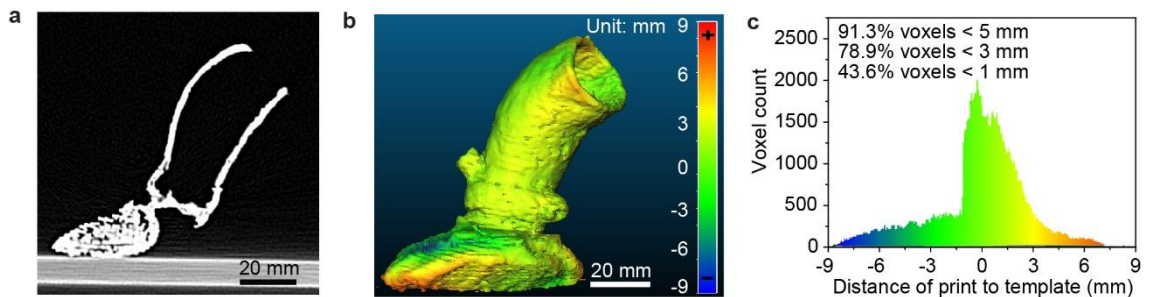


Figure 4.6. Anatomical fidelity analysis of the 3D printed aortic root model with respect to patient's data. (a) CT scan of the 3D printed aortic root model. (b) Calibrated distance map comparing the anatomical fidelity of the 3D printed aortic root model with patient's anatomy. (c) Histogram of the calibrated distances between the surface points of the 3D printed aortic root model and the patient's anatomy.

In addition, the TAVR prosthetic valve was implanted into the model (Figure C.1 in Appendix C) and the outcomes were compared to the patient's postoperative data via CT imaging (Figure 4.7). It was observed that the location of calcifications landing on the

aortic wall in the model after valve implantation, was analogous to that of the patient's postoperative scans (Figure 4.7 (a)). The diameter of the prosthetic valve was also subject to change after implantation in the aortic root, which can be used as another metric for evaluating the fidelity of the 3D printed aortic root model in comparison with patient's anatomy. For this purpose, we evaluated the changes in diameter of the implanted prosthetic valve at 9 different frame node levels. The results showed that the diameter values of the implanted valve in the 3D printed model were close to the patient's corresponding postoperative data at different systolic phases of the cardiac cycle (Figure 4.7 (b)). A maximum difference of 6.5 % (node level 3) and minimum difference of 2.2% (node level 1) between the diameter of implanted valve in the 3D printed model and the average of diameters over the four systolic phases (phases 0, 10, 20, 30) of patient's postoperative data were obtained, hence verifying the fidelity of this 3D printed model compared to the patient's anatomy.

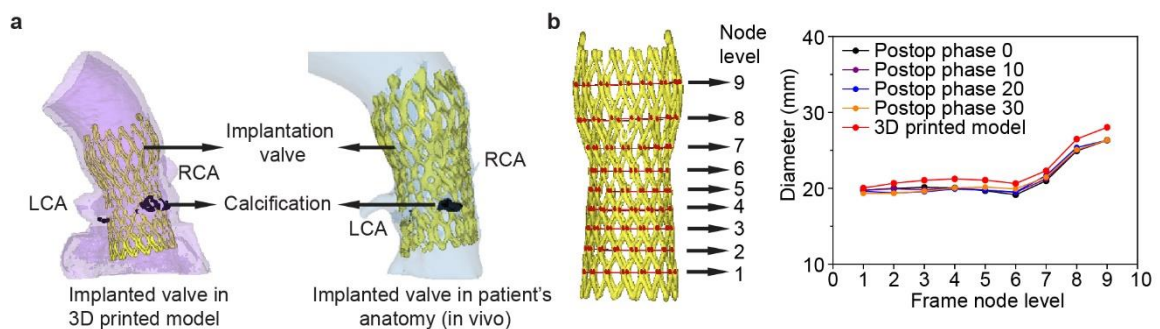


Figure 4.7. Analysis of the deflection of the valve's frame implanted in the 3D printed model and comparison with patient's postoperative data. (a) Comparison of the implanted TAVR prosthesis in the 3D printed model with patient's postoperative data (RCA: right coronary artery, LCA: left coronary artery). (b) Comparison of changes in frame diameters of the implanted valve in the 3D printed model with the patient's postoperative data at 9 different node levels.

4.4. *In Vitro* Hemodynamic Studies

To capture the hemodynamic performances of the 3D printed aortic root models, we evaluated their *in vitro* responses in pulsatile flow cycles. For this purpose, we fabricated two sets of models corresponding to normal and stenotic cases: 1) models that were printed using ink 1 for the myocardium and leaflets (lower modulus), ink 3 for the aortic wall, and did not have calcified regions on the leaflets (Figure 4.8 (a)); and 2) models that were printed using ink 2 for the myocardium and leaflets (higher modulus (197)), ink 4 for the aortic wall, and had calcified regions on the leaflets printed using ink 5 (Figure 4.8 (b)). The 3D printed models were placed in a custom setup. As shown in Figure 4.9, the test setup comprised a pulsatile piston blood pump for simulating cyclic flow (Model 1423, Harvard Apparatus), an endoscopic videoscope (IPLEX FX Model IV8000 IV6C6-13, Olympus) for direct visualization of leaflets movement, a flow probe sensor for measuring the volumetric flow rates (ME 13 PXN inline flow sensor, Transonic), two pressure catheters for monitoring the ventricular and aortic pressures (a balloon pressure catheter (ATTAIN™ venogram balloon catheter 6215-80 cm, Medtronic) and a syringe-based pressure catheter), a fluid reservoir, and an arterial compliance chamber. The height of the arterial compliance chamber in the setup was adjusted to provide the approximate baseline diastolic aortic pressures in different cases of testing. Silicone tubing was used to connect the components to each other, and to the 3D printed aortic root models. To mimic the dynamic viscosity (3.45 mPa s) and density (1060 kg/m³) of blood (198), a solution comprising of water and glycerol with a weight ratio of 6:4 was used as the working fluid in these tests (dynamic viscosity of ca. 3.3 mPa s and density of ca. 1098 kg/m³). The pump

settings were adjusted to provide a rate of 70 beats per minute and an output phase ratio (% systole / % diastole) of 50/50 for all tests. The values of stroke volume were adjusted for different experiments.

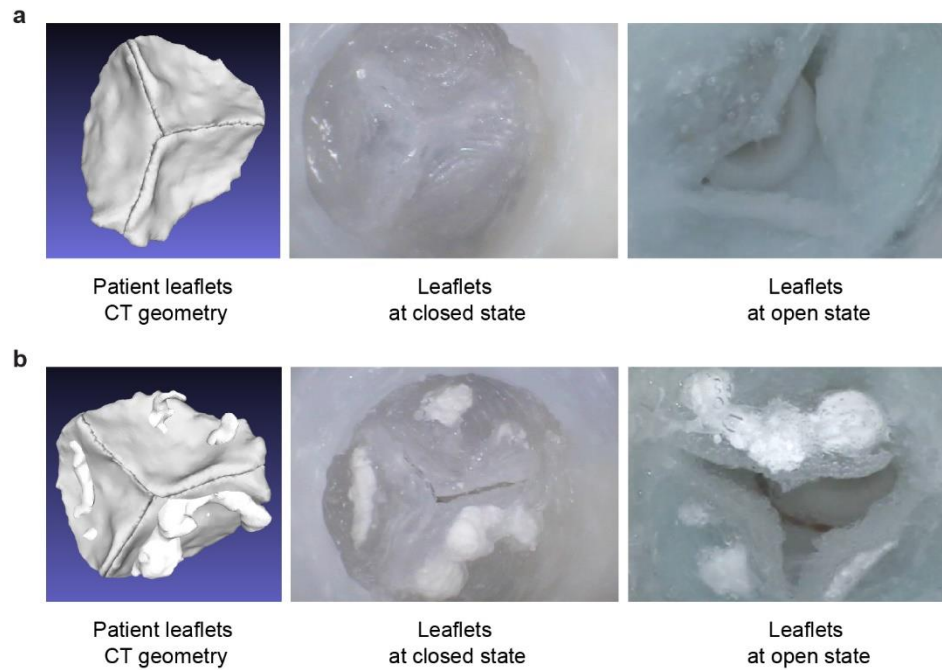


Figure 4.8. Models used for *in vitro* hemodynamic studies. (a) Leaflets of the 3D printed models without calcification (set 1) at open and closed states used for *in vitro* hemodynamic evaluation. (b) Leaflets of the 3D printed models with calcification (set 2) at open and closed states used for *in vitro* hemodynamic evaluation.

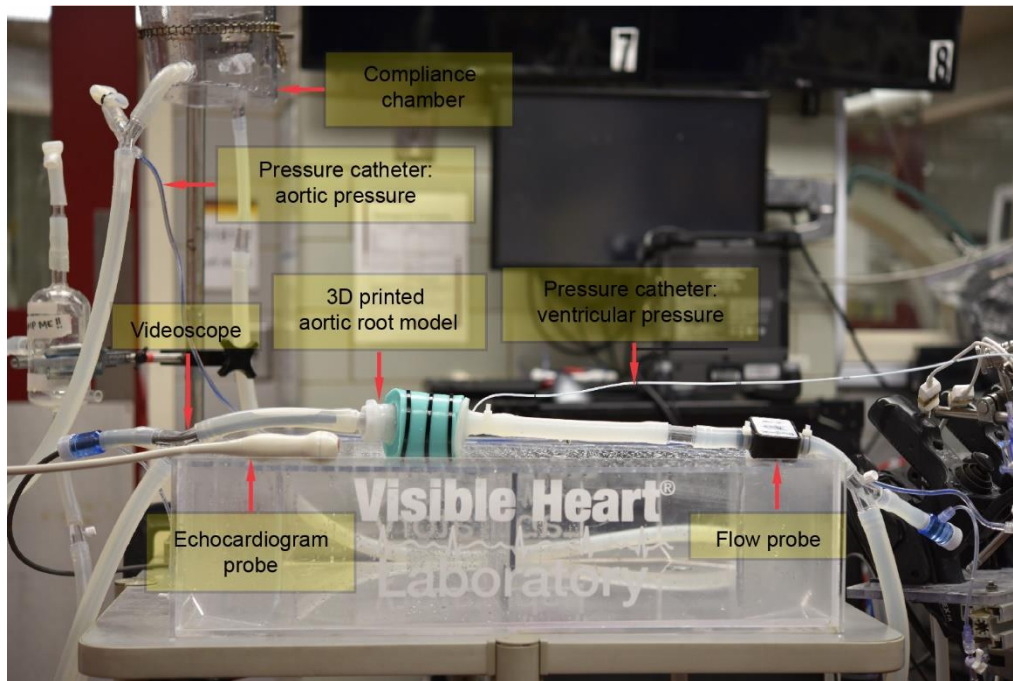


Figure 4.9. Test setup for *in vitro* hemodynamic studies.

In each flow cycle, upon the increase of ventricular pressure to a value greater than the aortic pressure, the aortic valve opened and allowed for ejection of the fluid flow from the ventricle into the aorta (systole phase). Once the ventricular pressure reached a value below the aortic pressure, the aortic valve closed (diastole phase). In the physiological cardiac cycles, the ejection of blood from left ventricle to the aorta results in increases in the aortic pressure. The maximum change in aortic pressure is referred to as the pulse pressure (PP) and is defined as the difference between the maximum aortic pressure in systole and its minimum value in diastole. At a constant stroke volume (SV), the amount of pulse pressure depends on the aortic compliance (C), which is a property of the aorta that allows for its expansion to accommodate the increases in pressure during blood ejection (199). The aortic compliance can be estimated as the ratio of the stroke volume to the pulse pressure ($C \sim SV/PP$) (200). In other words, higher arterial compliance results in smaller values of

pulse pressure at a specific stroke volume. Different factors such as aging, can result in decreasing arterial compliances, mainly due to changes in arterial wall matrix compositions. Specifically, aging has been associated with an increase in collagen content and crosslinking, as well as fragmentation of elastin fibers in the aortic wall, which ultimately lead to arteries with higher stiffnesses and lower compliances in the elderly (167). Given the predominant age group of individuals suffering from aortic stenosis, reduced aortic compliances are a prevalent condition in these patients (201). Hence, the capability to capture the changes in aortic compliance would be valuable for *in vitro* characterizations of transvalvular flows in AS cases with different severity conditions for various implications, including validation of computer flow dynamic models with blood and the development of vascular implants (21, 202). For this purpose, we compared the compliances of the two sets of models by varying the stroke volumes from 15 to 90 ml/stroke and measured the changes in pulse pressures (Figure 4.10). It was observed that the models in set 2 with calcified leaflets exhibited lower compliance and as a result, higher pulse pressure at a given stroke volume compared to the models in set 1. The estimated overall compliances for models in set 1 and 2 were 2.11 ml/mmHg and 0.90 ml/mmHg, respectively, which were close to the values reported for normal cases (1.91 ± 0.76 ml/mmHg) (200) and cases with moderate aortic stenosis and low aortic compliances (0.90 ± 0.17 ml/mmHg) (203).

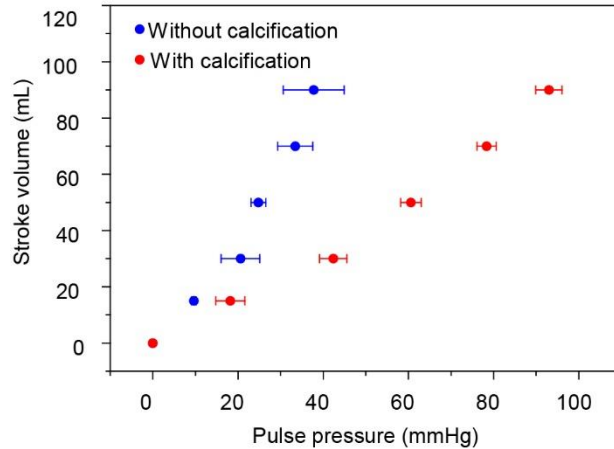


Figure 4.10. Comparison of compliance of models in set 1 and set 2 (without and with calcification, respectively).

Another hemodynamic marker in patients with aortic stenosis is elevated transvalvular pressure gradients between the left ventricle and aortic pressure during systole (204). This is typically caused by valvular obstructions and reduced arterial compliances, which ultimately results in increased left ventricular pressure overloads and dysfunction (201, 205). To this end, we examined the pressure changes in flows across the aortic valve, from the left ventricle region, to the aorta of the 3D printed models with and without calcification. For studying the pressure changes in the model without calcification, stroke volume was set to 70 ml/stroke and the baseline diastolic aortic pressure was adjusted to ~80 mmHg. For the model with calcification, the stroke volume and the baseline diastolic aortic pressure were adjusted to 50 ml/stroke and ~50 mmHg, respectively (206).

These models were able to replicate the expected trends of pressure changes observed in real cases of normal and stenotic valves. Specifically, it was observed that the model without calcifications yielded almost similar values for the ventricular and aortic pressures during the systole phase of the cardiac cycle, due to the free flow of the fluid from the left

ventricle to aorta, yielding an average of 1.23 mmHg peak-to-peak pressure gradient (Figure 4.11 (a)). On the other hand, for the model with calcification, a higher gradient with average value of 76.32 mmHg peak-to-peak pressure gradient was observed from the left ventricle to the aorta (Figure 4.11 (b)), which falls in the range of reported values for peak-to-peak pressure gradients in patients diagnosed with aortic stenosis (207, 208).

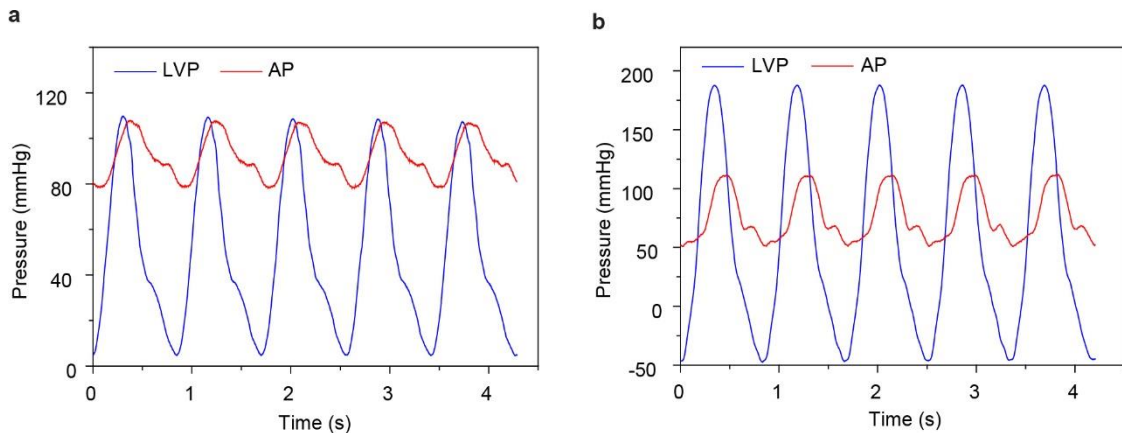


Figure 4.11. Comparison of pressure gradient between left ventricle and aorta in models with and without calcification. (a) Changes in left ventricle pressures (LVPs) and aortic pressures (APs) for model without calcification in consecutive pulsatile flow cycles. (b) Changes in left ventricle pressures (LVPs) and aortic pressures (APs) for model with calcification in consecutive pulsatile flow cycles.

Finally, we implanted a 26 mm EvolutTMR valve (Medtronic) in the aortic root model with calcified leaflets and assessed the appositions of the valve frame with the aortic annulus in order to identify the potential paravalvular leak sites. For this purpose, we selected three regions along the annulus as follows: 1) the region surrounding the commissure between right-coronary cusp (RCC) and non-coronary cusp (NCC); 2) the region surrounding non-coronary cusp; and 3) the region surrounding left-coronary cusp (LCC). We used a videoscope to visualize the appositions of the frame with respect to the model's aortic wall at these three locations, as well as the color Doppler echocardiography to verify PVL occurrences by evaluating the directions and speeds of the fluid flow in the

regions of interest (Figure 4.12). It was observed that an improper seal and existing gaps between the stent frame and the model's aortic wall at regions 1 and 3 resulted in some degrees of PVL at these locations, which were verified by the presence of eccentric jets and their velocities in the corresponding echocardiograms (209). On the other hand, the echocardiogram for region 2 did not indicate the occurrence of PVL, which was in accordance with the fact that no gaps were visually detected in this location.

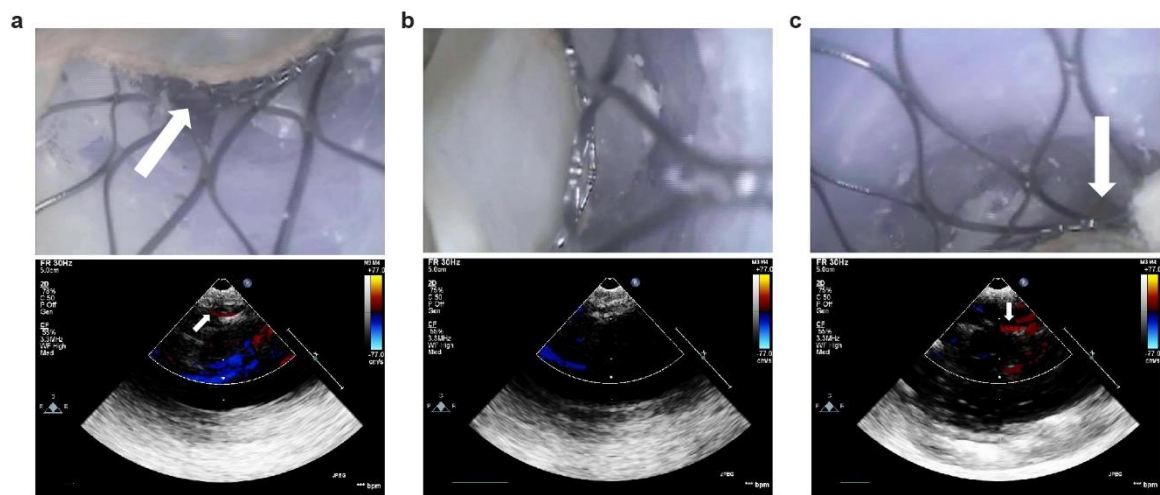


Figure 4.12. Detection of potential paravalvular leak sites (indicated by the white arrows) in the 3D printed aortic root model with implanted valve and corresponding color Doppler echocardiograms in (a) region 1, (b) region 2, and (c) region 3.

4.5. Visualization of Applied Pressures via Internally Integrated Sensor Arrays

In order to quantify the applied pressures on the critical region of the aortic root after prosthetic valve implantation, we designed a 3×3 capacitive pressure sensor array that was internally embedded within the critical landmark of the aortic root models and was in direct contact with the implanted valve. As discussed in Chapter 3.10, each sensing element in the designed array consisted of two layers of polyacrylamide-based ionic hydrogel as the conductive electrodes that were separated with a dielectric layer comprised of the

silicone-based material with a composition that was the same as the one used for the myocardium sections of the models. To transform the planar design of the sensor array to model's geometry and incorporate the device within the model's structure, two sets of horizontal and vertical electrode channels that conformally follow the contour of the anatomy were integrated in the model's design (Figure 4.13).

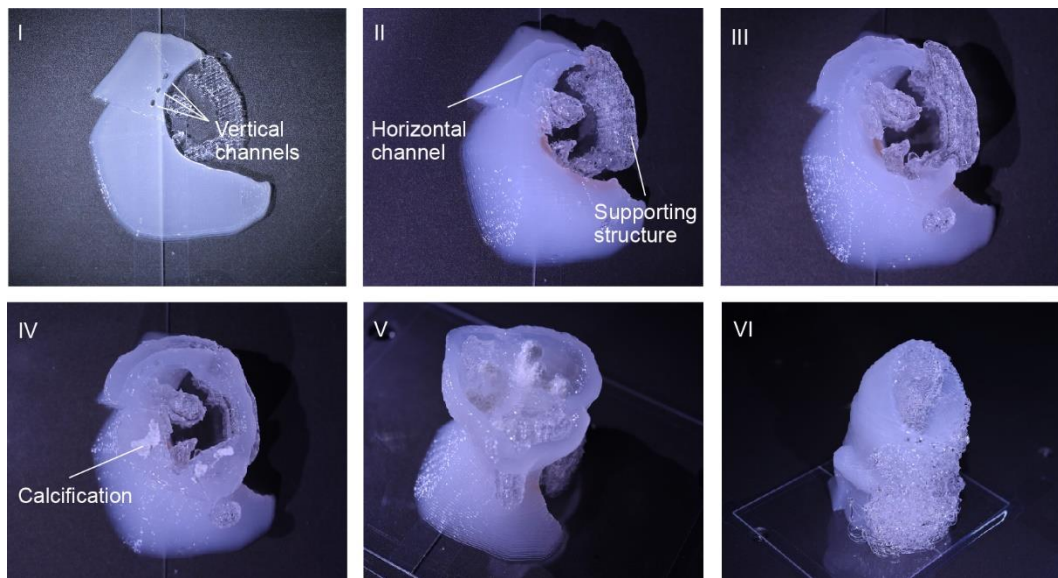


Figure 4.13. Step-by-step 3D printing of the aortic root model with internally integrated sensor array.

After printing and curing of the aortic root models, the horizontal (shown in green in Figure 4.14) and vertical channels (shown in orange in Figure 4.14) were then filled by injection of the aqueous solution of the ionically-conductive hydrogel, followed by UV photopolymerization.

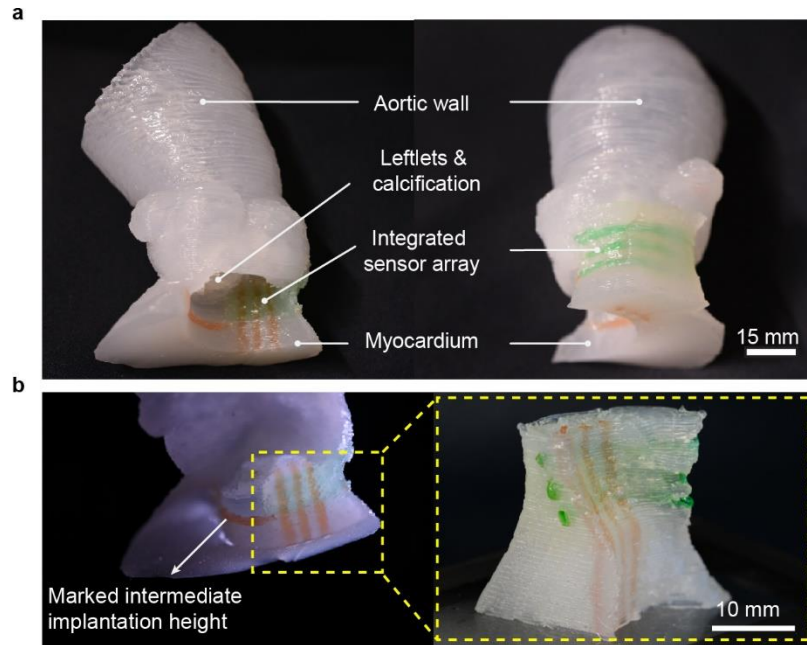


Figure 4.14. Final 3D printed aortic root model with internal sensor array. (a) Full model, (b) The corresponding isolated sensor region.

In order to translate the capacitance changes of the sensing elements to pressure values, the non-planar sensor array embedded within the model was calibrated. For this purpose, the region of the model limited to the 3×3 sensor array was fabricated separately (Figure 4.14 (b)). The calibration was performed by applying different pressures to each of the nine sensing units in the array and measuring the changes in their capacitance individually. The sensor array was fixed on a silicone-based platform (MoldStar 15, SmoothOn) and was mounted on a digital scale (Elec3) in order to record the values of applied forces during calibration (Figure 4.15 (a)). A similar calibration process discussed in Chapter 3.10 was performed. The recorded measurements were analyzed to obtain plots of $\frac{\Delta C}{C_0}$ versus applied pressure, yielding two linear regions for each of the sensing elements based on the range of $\frac{\Delta C}{C_0}$ (Figure 4.15 (b)). To translate the capacitance changes to pressures values, the

calibration equation corresponding to appropriate $\frac{\Delta C}{C_0}$ range of each sensing unit in the array was used (Table C.2 in Appendix C).

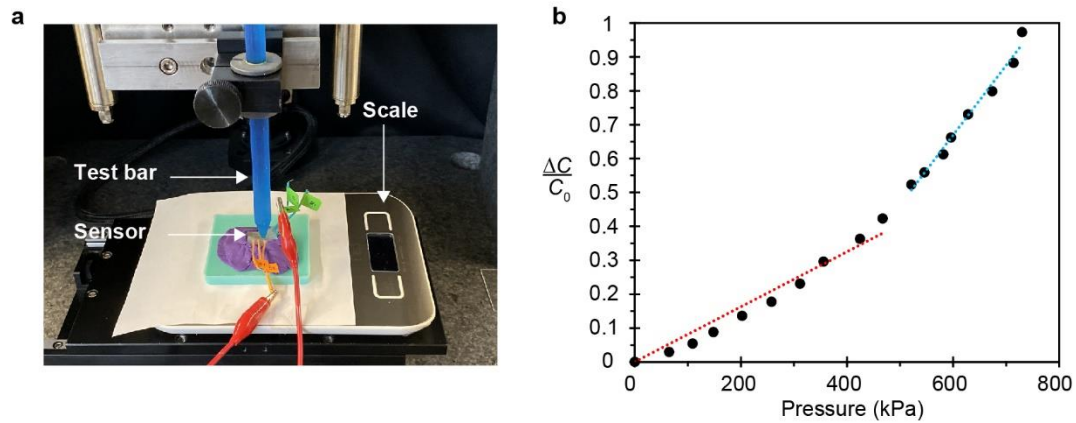


Figure 4.15. Calibration of the sensor array. (a) Test setup. (b) An example of calibration plot for the sensing units indicating the two corresponding linear regions.

The internally integrated sensor array on the model was used to map the pressures caused by the implanted valve on the critical region of the anatomy for different cases of prosthetic valve sizing and implantation depth. For each case, first the values of capacitance change for the sensing elements were obtained (Figure C.2 in Appendix C). Then, the pressure heatmaps were generated by translating the capacitance changes to pressure values by using the corresponding calibration equation for each element. As it can be seen, the resulted pressure maps provided quantitative visualizations of the pressure distributions for each of the cases, which in turn could be utilized to optimize the prostheses implantation heights and alignments within the given anatomy. Specifically, we implanted a 29 mm Evolut™ R valve frame (Medtronic) at 3 different implantation heights (Figures 4.16 (a-c)) that yielded estimated maximum pressure values of ca. 234 kPa, 486 kPa, and 404 kPa corresponding to implantations at a shallow height, intermediate height, and deep height.

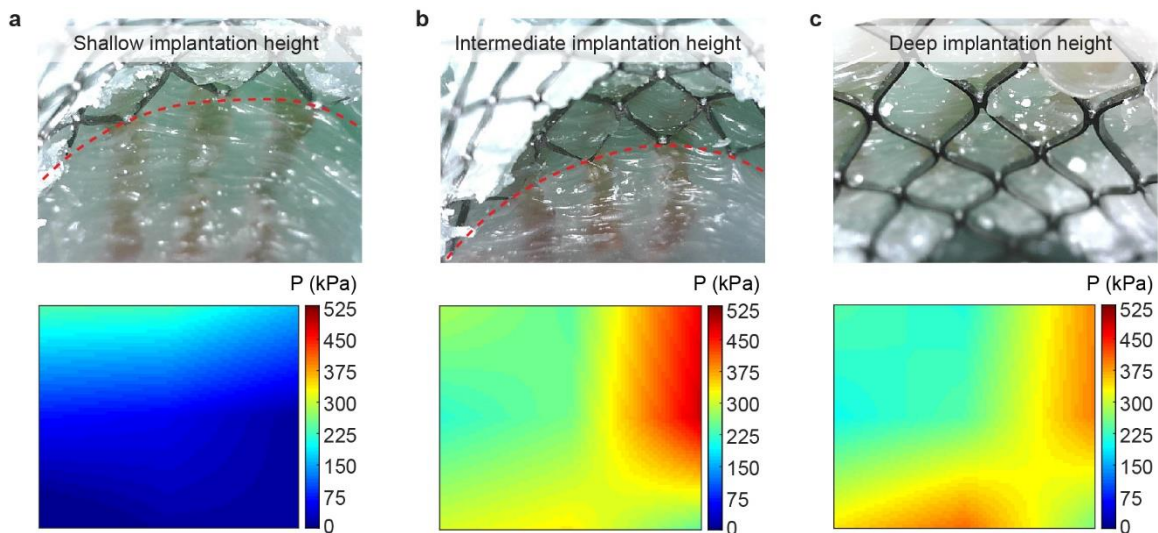


Figure 4.16. Visualization of applied pressures for different cases of valve implantation height. (a) Implantation of the 29 mm EvolutTM R TAVR valve frame at a shallow height. (b) Implantation of the 29 mm EvolutTM R TAVR valve frame at an intermediate height. (c) Implantation of the 29 mm EvolutTM R TAVR valve frame at a deep height.

Similarly, we implanted three different TAVR valves with sizes of 26 mm (Medtronic EvolutTM R, Figure 4.17 (a)), 29 mm (Medtronic EvolutTM R, Figure 4.17 (b)), and 31 mm (Medtronic CoreValveTM, Figure 4.17 (c)). As it can be seen, the resulted pressure maps showed much lower pressure values for the case with 26 mm valve compared to 29 mm and 31 mm, which was verified by the existing gaps between the valve frame and the model's wall in this case. The estimated maximum value of pressure for these cases were ca. 60 kPa, 375 kPa, and 528 kPa, respectively.

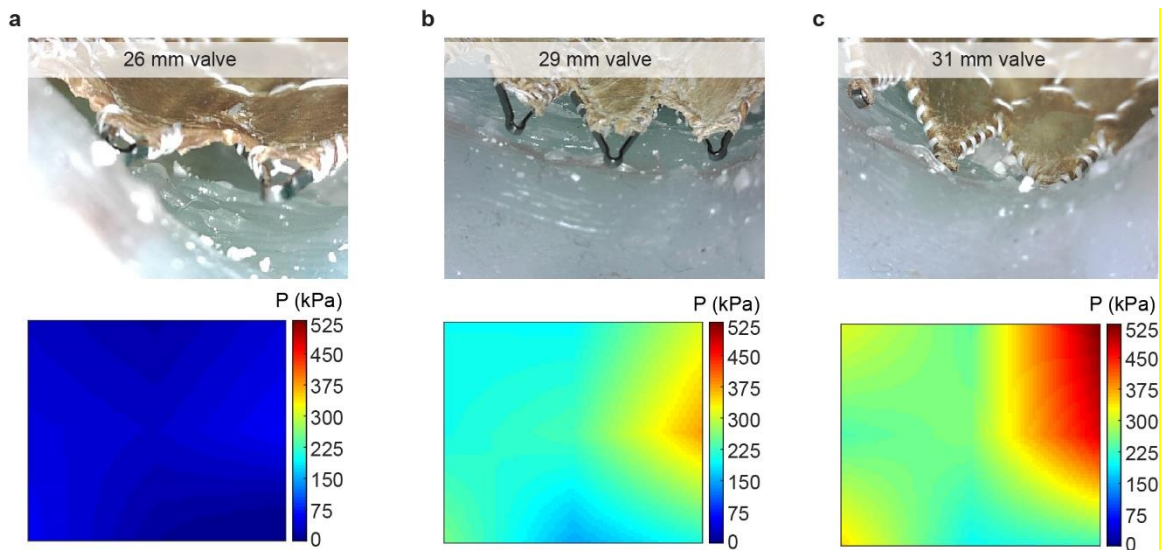


Figure 4.17. Visualization of applied pressures for different cases of valve sizing. (a) Implantation of the 26 mm EvolutTM R TAVR valve at an intermediate height. (b) Implantation of the 29 mm EvolutTM R TAVR valve at an intermediate height. (c) Implantation of the 31 mm CoreValveTM TAVR valve at an intermediate height.

Previous case studies on computational modeling of the applied pressures on the critical region of the aortic root anatomy after prosthetic valve implantation have suggested that conduction abnormalities may occur for maximum contact pressures within 0.43-0.70 MPa for self-expanding CoreValveTM/EvolutTM R valve (Medtronic) (210) and 0.29-0.8 MPa for mechanically expandable Lotus valve (Boston Scientific), with cut-off values of 0.39 MPa and 0.36 MPa, respectively (211). Correlating these values with the pressure readings from the different cases of valve implantations suggests that the patient may experience conduction abnormalities with a valve size of 29 mm or 31 mm positioned at the intermediate implantation height.

4.6. Conclusion

Here, it was uniquely demonstrated that the fabrication of multi-material 3D printed aortic root with internal sensor array are of high research value for different purposes in

TAVR testing applications. We evaluated the efficacy of the models by comparing their geometrical fidelity with patient's postoperative data, as well as their *in vitro* hemodynamic performance in cases with and without calcification. Furthermore, it was demonstrated that the internal sensor array can facilitate the optimization of prosthetic valve selection and placement via mapping the pressure applied on the critical region of the anatomy. These models can be utilized to complement the current clinical practices in TAVR preprocedural planning and facilitate the decision-making processes in various aortic stenosis cases, e.g., those with different levels of disease severities and anatomical intricacies requiring one to carefully select the appropriate type, size, implantation depth, and positioning of the replacement valve. Doing so would aid to alleviate the risks of postoperative complications, as well as gaining a better understanding on how the interplays of these factors might lead to such issues based on each patient's unique anatomical features.

Indeed, the proof of concept demonstrations described here need to be further verified with large-scale, retrospective and prospective clinical studies. Specifically, a large cohort of patients with postoperative heart block should be analyzed both clinically and via computer simulations, to validate the efficacies of utilizing such models for the prediction of potential conduction abnormalities, as well as defining the threshold values for the contact pressures for prediction of conduction disturbances with different types of valve prostheses. Future efforts should also be focused on developing 3D printing materials to better mimic the behaviors of biological tissues, including heterogeneity, anisotropy and strain-stiffening properties at higher strains. This can possibly be achieved by controlling

the orientation of printing pathways (212, 213) or embedding fillers, such as micro-structured fibers (214) into the material system.

In addition, improving the resolutions and sensitivities of the integrated sensor arrays could enhance the localizations of regions with critical contact pressures, thus improving the efficacies of such models in alleviating the risks of post-TAVR conduction abnormalities.

Additional details on experimental methods, materials, and other supplementary information for this chapter is provided in Appendix C.

CHAPTER 5[†]

Conclusions and Future Directions

5.1. Conclusions

This dissertation entailed an investigation at the intersection of soft biomimicking electroactive and tissue-like material systems and electromechanical transducer design coupled with multi-material, extrusion-based 3D printing process, for primary applications in development of patient-specific organ models for preoperative planning and clinical training.

Chapter 1 described the inception of implementing 3D printed patient-specific organ models in medical practices and discussed the two critical limitations of the current 3D printed organ models using commercial-grade materials that served as the main motivations of this work. These two limitations were identified as: (i) the insufficient mimicry of the sense and properties of the biological tissues, and (ii) lacking advanced functionalities to provide quantitative feedback during organ manipulation. Next, an overview of 3D printed organ models using commercial materials and their applications in different medical fields were provided, with an emphasis on 3D printing material systems including rigid-plastic materials, elastomeric (rubber-like) materials, and powder-based materials, such as cellulose/starch and plaster. Finally, the general concept of dielectric elastomers was introduced as the selected transduction technology for development of electromechanical devices in this work.

Chapter 2 presented the work on developing a silicone-based material system with tissue-mimicking properties that can be used for 3D printing of patient-specific organ models. The proposed polymeric material system mainly comprised of an active agent and a bulking agent. It was shown that by adjusting the weight ratios of these two components

in the formulation, the crosslinking density of the material can be modified, and the elastic modulus of the material can be tuned to match the broad range of reported moduli for the soft tissues. For instance, changing the weight ratio of the bulking to active agent from 0 to 2.05 resulted in a decrease in Young's modulus from 677.6 ± 28.8 kPa to 37.5 ± 1.9 kPa. Different characterization of the proposed material system showed the favorable rheological properties of the formulations for the 3D printing process, as well as their stability in the test environments. As a proof of concept demonstration, a patient-specific prostate model was 3D printed using a material formulation that was optimized to mimic the static and dynamic mechanical behavior of tested specimens of human prostate tissue. The anatomical fidelity between the 3D printed prostate model and its corresponding patient prostate was confirmed via a quantitative analysis and 3D registration techniques. For the purpose of demonstrating the applications of such models and the advantage of their tissue-like tactile sensation during diagnostic and surgical interventions, the 3D printed prostate model was used for endoscopy and suturing practices.

Chapter 3 discussed the design and development of soft electromechanical transducers based on ionic hydrogel-elastomer hybrids. It was demonstrated that this hybrid material structure can be applied for 3D printing of soft dielectric elastomer actuators that can generate bending modes of motion in response to applied electrical stimuli. This involved the selection and optimization of materials for performance and printability, solving key material integration challenges, and fabrication and characterization of the final devices. Specifically, the performance of the soft actuators was characterized in response to applied (i) ramp-up electrical input; (ii) cyclic electrical loading; and (iii) payload tip masses. A

maximum vertical tip displacement of 9.78 ± 2.52 mm at 5.44 kV was achieved from the tested devices. Furthermore, the nonlinear actuation behavior of the unimorph DEA was modeled using analytical energetic formulation and a finite element method (FEM). Moreover, it was shown that the same strategy can be applied to 3D print a soft capacitive tactile sensor. The 3D printed sensor was characterized and was conformally integrated on the tissue-like prostate model for the purpose of obtaining quantitative feedback during handling the organ model with surgical/diagnostic tools. This feedback can be used as an indicator of surgical performance and can provide medical professionals with the ability to quantify and control the ranges of pressure they apply to the organ during preoperative rehearsal and training. Finally, the design, 3D printing, and characterization of sensor arrays using the custom-formulated tissue-mimicking ink as the dielectric and encapsulation layers were discussed with the end goal of their direct, monolithic integration into organ models for providing quantitative feedback during targeted surgical interventions.

Finally, Chapter 4 presented the combination of the previous concepts for multi-material 3D printing of patient-specific aortic root models with internally-integrated sensor arrays that can be used for different purposes in transcatheter aortic valve replacement applications. The models were 3D printed using the customized materials with mechanical properties commensurate to those of different components of the aortic root, including the aortic wall, the myocardium and leaflets, as well as the calcified regions. Therefore, the 3D printed models represented the anatomical features of the patient, as well as the mechanical properties of the corresponding tissues. In addition, to verify the anatomical fidelity of the

3D printed model with respect to patient's organ, a prosthetic valve was implanted into the 3D printed aortic root model. The evaluations of changes in diameter of the implant in the model yielded analogous values to those of patient's postoperative data. The models were also used in *in vitro* hemodynamic studies to evaluate the flow properties in models with and without calcification, as well as for predictions of paravalvular leak. Furthermore, the internally integrated sensor array on the model was used to map the pressure caused by the implanted valve on the critical region of the anatomy for different cases of prosthetic valve sizing and implantation depth. Hence, the internal sensor array can facilitate the optimization of prosthetic valve selection and placement and can pave the path for mitigating the risk of postoperative complications, as well as gaining a better understanding on how these factors could lead to such issues based on each patient's unique anatomical features.

5.2. Future Directions

We perceive that the outcomes of this work will build a platform for future innovations in advanced manufacturing of smart organ models and nature-mimicking robotic systems. Particularly, the concepts outlined here were applied for 3D printing aortic root models with internal sensor for TAVR applications as an example to demonstrate the implication of such models for minimally invasive surgeries. On a broader scope, such patient-specific models can be designed with targeted functionalities for variety of minimally invasive procedures, including but not limited to endovascular coiling, sialoendoscopy, and coronary angioplasty and/or stenting. Such models could be implemented as surgical guides to address the limited accesses inherent to these types of procedures by providing

realistic, 3D visualizations of the organs of interest and targeted quantitative feedback for the specified surgical intervention; hence, ultimately enhancing the preoperational planning and alleviating the risk of intra- and post-operative complications of associated therapies. In addition, these sensing models could serve as a benchtop platform for the development of next-generation prostheses and medical devices.

Moreover, the observed electromechanical performance suggests the promise of 3D printing hydrogel-elastomer hybrids as soft actuators and sensors, thus paving the path for 3D printing self-sensing, soft biomimicking systems with complex geometries and functionalities that harness the dual sensing/actuation capabilities of dielectric elastomers. This self-sensing capability could be employed for closed-loop feedback control of soft systems without the need for additional optical or electromechanical sensors (215-218) and could be of particular interest for mimicking the proprioception abilities of natural muscle, enabled by strain-sensitive neurons that provide a sense of spatial position and motion (215).

In addition, such capability can contribute to the incorporation of advanced dynamic functionalities into the organ models, such as pulsations of heart or the functions of heart's valves. The use of real-to-life organ models embedded with actuation and sensing feedback could have a significant impact on further enhancing these matters and defining a new paradigm in future of personalized medicine. On a long-term basis, the outcomes of this work could contribute to the incorporation of cell-seeded structures into the dynamic organ models, thus even aiding in setting the stage for bionic organs.

Furthermore, the application of the 3D printed soft actuator and sensors could go well beyond their incorporation in organ models discussed in this study. The dual sensing/actuation capabilities of dielectric elastomers can be harnessed for freeform fabrication of untethered, self-sensing mechanical systems and nature mimicking soft robots with implications for artificial life and programmable matter; mechanically-driven morphogenesis; smart prosthesis; and dynamic skins, tactile displays, and wearable electronics.

Bibliography

1. H. Owen, Early Use of Simulation in Medical Education. *Simulation in Healthcare* **7**, 102-116 (2012).
2. G. Meller, A Typology of Simulators for Medical Education. *Journal of Digital Imaging* **10**, 194-196 (1997).
3. I. Badash, K. Burtt, C. A. Solorzano, J. N. Carey, Innovations in Surgery Simulation: A Review of Past, Current and Future Techniques. *Annals of Translational Medicine* **4**, 453 (2016).
4. B. Zevin, R. Aggarwal, T. P. Grantcharov, Surgical Simulation in 2013: Why Is It Still Not the Standard in Surgical Training? *Journal of the American College of Surgeons* **218**, 294-301 (2014).
5. M. A. Makary, M. Daniel, Medical Error-the Third Leading Cause of Death in the US. *BMJ* **353**, i2139 (2016).
6. W. T. Mehtsun, A. M. Ibrahim, M. Diener-West, P. J. Pronovost, M. A. Makary, Surgical Never Events in the United States. *Surgery* **153**, 465-472 (2013).
7. S. Mottl-Link, M. Hubler, T. Kuhne, U. Rietdorf, J. J. Krueger, B. Schnackenburg, R. De Simone, F. Berger, A. Juraszek, H. P. Meinzer, M. Karck, R. Hetzer, I. Wolf, Physical Models Aiding in Complex Congenital Heart Surgery. *The Annals of Thoracic Surgery* **86**, 273-277 (2008).
8. R. Dankowski, A. Baszko, M. Sutherland, L. Firek, P. Kalmucki, K. Wroblewska, A. Szyszka, A. Groothuis, T. Siminiak, 3d Heart Model Printing for Preparation of Percutaneous Structural Interventions: Description of the Technology and Case Report. *Kardiologia Polska* **72**, 546-551 (2014).
9. A. McWilliams, Global Markets for 3d Printing. *Rep. IAS102B*. BCC Research, Wellesley, MA, (2016). <https://www.bccresearch.com/market-research/instrumentation-and-sensors/3d-printing-global-markets-report-ias102b.html>.
10. J. C. Bernhard, S. Isotani, T. Matsugasumi, V. Duddalwar, A. J. Hung, E. Suer, E. Baco, R. Satkunasivam, H. Djaladat, C. Metcalfe, B. Hu, K. Wong, D. Park, M. Nguyen, D. Hwang, S. T. Bazargani, A. L. de Castro Abreu, M. Aron, O. Ukimura, I. S. Gill, Personalized 3d Printed Model of Kidney and Tumor Anatomy: A Useful Tool for Patient Education. *World Journal of Urology* **34**, 337-345 (2016).
11. T. Niikura, M. Sugimoto, S. Y. Lee, Y. Sakai, K. Nishida, R. Kuroda, M. Kurosaka, Tactile Surgical Navigation System for Complex Acetabular Fracture Surgery. *Orthopedics* **37**, 237-242 (2014).
12. L. Xu, S. R. Gutbrod, A. P. Bonifas, Y. Su, M. S. Sulkin, N. Lu, H. J. Chung, K. I. Jang, Z. Liu, M. Ying, C. Lu, R. C. Webb, J. S. Kim, J. I. Laughner, H. Cheng, Y. Liu, A. Ameen, J. W. Jeong, G. T. Kim, Y. Huang, I. R. Efimov, J. A. Rogers, 3d Multifunctional Integumentary Membranes for Spatiotemporal Cardiac Measurements and Stimulation across the Entire Epicardium. *Nature Communications* **5**, 3329 (2014).
13. F. Rengier, A. Mehndiratta, H. von Tengg-Kobligk, C. M. Zechmann, R. Unterhinninghofen, H. U. Kauczor, F. L. Giesel, 3d Printing Based on Imaging

- Data: Review of Medical Applications. *International Journal of Computer Assisted Radiology and Surgery* **5**, 335-341 (2010).
14. G. Wurm, B. Tomancok, P. Pogady, K. Holl, J. Trenkler, Cerebrovascular Stereolithographic Biomodeling for Aneurysm Surgery. Technical Note. *Journal of Neurosurgery* **100**, 139-145 (2004).
 15. D. Mitsouras, P. Liacouras, A. Imanzadeh, A. A. Giannopoulos, T. Cai, K. K. Kumamaru, E. George, N. Wake, E. J. Caterson, B. Pomahac, V. B. Ho, G. T. Grant, F. J. Rybicki, Medical 3d Printing for the Radiologist. *Radiographics* **35**, 1965-1988 (2015).
 16. A. A. Giannopoulos, D. Mitsouras, S. J. Yoo, P. P. Liu, Y. S. Chatzizisis, F. J. Rybicki, Applications of 3d Printing in Cardiovascular Diseases. *Nature Reviews Cardiology* **13**, 701-718 (2016).
 17. B. C. Gross, J. L. Erkal, S. Y. Lockwood, C. Chen, D. M. Spence, Evaluation of 3d Printing and Its Potential Impact on Biotechnology and the Chemical Sciences. *Analytical Chemistry* **86**, 3240-3253 (2014).
 18. Z. X. Low, Y. T. Chua, B. M. Ray, D. Mattia, I. S. Metcalfe, D. A. Patterson, Perspective on 3d Printing of Separation Membranes and Comparison to Related Unconventional Fabrication Techniques. *Journal of Membrane Science* **523**, 596-613 (2017).
 19. G. Gómez-Ciriza, T. Hussain, T. Gómez-Cía, I. Valverde, Potential of 3d-Printed Models in Planning Structural Interventional Procedures. *Interventional Cardiology* **7**, 345-352 (2015).
 20. A. Marro, T. Bandukwala, W. Mak, Three-Dimensional Printing and Medical Imaging: A Review of the Methods and Applications. *Current Problems in Diagnostic Radiology* **45**, 2-9 (2016).
 21. M. Vukicevic, B. Mosadegh, J. K. Min, S. H. Little, Cardiac 3d Printing and Its Future Directions. *JACC: Cardiovascular Imaging* **10**, 171-184 (2017).
 22. Z. Sun, S. Y. Lee, A Systematic Review of 3-D Printing in Cardiovascular and Cerebrovascular Diseases. *Anatolian Journal of Cardiology* **17**, 423-435 (2017).
 23. R. J. Young, P. A. Lovell, *Introduction to Polymers*. (CRC Press, Boca Raton, FL, USA, ed. 3rd, 2011).
 24. K. M. Farooqi, C. G. Lengua, A. D. Weinberg, J. C. Nielsen, J. Sanz, Blood Pool Segmentation Results in Superior Virtual Cardiac Models Than Myocardial Segmentation for 3d Printing. *Pediatric Cardiology* **37**, 1028-1036 (2016).
 25. K. M. Farooqi, O. Saeed, A. Zaidi, J. Sanz, J. C. Nielsen, D. T. Hsu, U. P. Jorde, 3d Printing to Guide Ventricular Assist Device Placement in Adults with Congenital Heart Disease and Heart Failure. *JACC: Heart Failure* **4**, 301-311 (2016).
 26. S. Schievano, F. Migliavacca, L. Coats, S. Khambadkone, M. Carminati, N. Wilson, J. E. Deanfield, P. Bonhoeffer, A. M. Taylor, Percutaneous Pulmonary Valve Implantation Based on Rapid Prototyping of Right Ventricular Outflow Tract and Pulmonary Trunk from MR Data. *Radiology* **242**, 490-497 (2007).

27. N. Wake, H. Chandarana, W. C. Huang, S. S. Taneja, A. B. Rosenkrantz, Application of Anatomically Accurate, Patient-Specific 3d Printed Models from MRI Data in Urological Oncology. *Clinical Radiology* **71**, 610-614 (2016).
28. M. Kusaka, M. Sugimoto, N. Fukami, H. Sasaki, M. Takenaka, T. Anraku, T. Ito, T. Kenmochi, R. Shiroki, K. Hoshinaga, Initial Experience with a Tailor-Made Simulation and Navigation Program Using a 3-D Printer Model of Kidney Transplantation Surgery. *Transplantation Proceedings* **47**, 596-599 (2015).
29. Y. Komai, M. Sugimoto, N. Gotohda, N. Matsubara, T. Kobayashi, Y. Sakai, Y. Shiga, N. Saito, Patient-Specific 3-Dimensional Printed Kidney Designed for "4d" Surgical Navigation: A Novel Aid to Facilitate Minimally Invasive Off-Clamp Partial Nephrectomy in Complex Tumor Cases. *Urology* **91**, 226-233 (2016).
30. J. R. Anderson, W. L. Thompson, A. K. Alkattan, O. Diaz, R. Klucznik, Y. J. Zhang, G. W. Britz, R. G. Grossman, C. Karmonik, Three-Dimensional Printing of Anatomically Accurate, Patient Specific Intracranial Aneurysm Models. *Journal of Neurointerventional Surgery* **8**, 517-520 (2016).
31. B. O. Ermano, A. C. Opolski, M. Olandoski, J. A. Foggiatto, L. F. Kubrusly, U. A. Dietz, C. Zini, M. M. M. A. Marinho, A. G. Leal, R. Ramina, Rapid Prototyping of Three-Dimensional Biomodels as an Adjuvant in the Surgical Planning for Intracranial Aneurysms. *Acta Cirurgica Brasileira* **28**, 756-761 (2013).
32. N. N. Zein, I. A. Hanouneh, P. D. Bishop, M. Samaan, B. Eghtesad, C. Quintini, C. Miller, L. Yerian, R. Klatte, Three-Dimensional Print of a Liver for Preoperative Planning in Living Donor Liver Transplantation. *Liver Transplantation* **19**, 1304-1310 (2013).
33. R. Souzaki, Y. Kinoshita, S. Ieiri, M. Hayashida, Y. Koga, K. Shirabe, T. Hara, Y. Maehara, M. Hashizume, T. Taguchi, Three-Dimensional Liver Model Based on Preoperative Ct Images as a Tool to Assist in Surgical Planning for Hepatoblastoma in a Child. *Pediatric Surgery International* **31**, 593-596 (2015).
34. M. J. Loadman, *Analysis of Rubber and Rubber-Like Polymers*. (Springer Netherlands, 2012).
35. S. J. Yoo, T. Spray, E. H. Austin, 3rd, T. J. Yun, G. S. van Arsdell, Hands-on Surgical Training of Congenital Heart Surgery Using 3-Dimensional Print Models. *The Journal of Thoracic and Cardiovascular Surgery* **153**, 1530-1540 (2017).
36. L. Kiraly, M. Tofeig, N. K. Jha, H. Talo, Three-Dimensional Printed Prototypes Refine the Anatomy of Post-Modified Norwood-1 Complex Aortic Arch Obstruction and Allow Presurgical Simulation of the Repair. *Interactive Cardiovascular and Thoracic Surgery* **22**, 238-240 (2016).
37. I. Shiraishi, M. Yamagishi, K. Hamaoka, M. Fukuzawa, T. Yagihara, Simulative Operation on Congenital Heart Disease Using Rubber-Like Urethane Stereolithographic Biomodels Based on 3d Datasets of Multislice Computed Tomography. *European Journal of Cardio-Thoracic Surgery* **37**, 302-306 (2010).
38. D. H. Yang, J. W. Kang, N. Kim, J. K. Song, J. W. Lee, T. H. Lim, Myocardial 3-Dimensional Printing for Septal Myectomy Guidance in a Patient with Obstructive Hypertrophic Cardiomyopathy. *Circulation* **132**, 300-301 (2015).

39. T. Kimura, A. Morita, K. Nishimura, H. Aiyama, H. Itoh, S. Fukaya, S. Sora, C. Ochiai, Simulation of and Training for Cerebral Aneurysm Clipping with 3-Dimensional Models. *Neurosurgery* **65**, 719-726 (2009).
40. I. S. Khan, P. D. Kelly, R. J. Singer, Prototyping of Cerebral Vasculature Physical Models. *Surg Neurol Int* **5**, 11 (2014).
41. G. Wurm, M. Lehner, B. Tomancok, R. Kleiser, K. Nussbaumer, Cerebrovascular Biomodeling for Aneurysm Surgery: Simulation-Based Training by Means of Rapid Prototyping Technologies. *Surgical Innovation* **18**, 294-306 (2011).
42. S. Bustamante, S. Bose, P. Bishop, R. Klatter, F. Norris, Novel Application of Rapid Prototyping for Simulation of Bronchoscopic Anatomy. *Journal of Cardiothoracic and Vascular Anesthesia* **28**, 1122-1125 (2014).
43. S. N. Kurenov, C. Ionita, D. Sammons, T. L. Demmy, Three-Dimensional Printing to Facilitate Anatomic Study, Device Development, Simulation, and Planning in Thoracic Surgery. *The Journal of Thoracic and Cardiovascular Surgery* **149**, 973-979 (2015).
44. D. Schmauss, S. Haeberle, C. Hagl, R. Sodian, Three-Dimensional Printing in Cardiac Surgery and Interventional Cardiology: A Single-Centre Experience. *European Journal of Cardio-Thoracic Surgery* **47**, 1044-1052 (2015).
45. K. Kondo, N. Harada, H. Masuda, N. Sugo, S. Terazono, S. Okonogi, Y. Sakaeyama, Y. Fuchinoue, S. Ando, D. Fukushima, J. Nomoto, M. Nemoto, A Neurosurgical Simulation of Skull Base Tumors Using a 3d Printed Rapid Prototyping Model Containing Mesh Structures. *Acta Neurochirurgica* **158**, 1213-1219 (2016).
46. M. Oishi, M. Fukuda, N. Yajima, K. Yoshida, M. Takahashi, T. Hiraishi, T. Takao, A. Saito, Y. Fujii, Interactive Presurgical Simulation Applying Advanced 3d Imaging and Modeling Techniques for Skull Base and Deep Tumors. *Journal of Neurosurgery* **119**, 94-105 (2013).
47. J. U. Lind, T. A. Busbee, A. D. Valentine, F. S. Pasqualini, H. Yuan, M. Yadid, S. J. Park, A. Kotikian, A. P. Nesmith, P. H. Campbell, J. J. Vlassak, J. A. Lewis, K. K. Parker, Instrumented Cardiac Microphysiological Devices Via Multimaterial Three-Dimensional Printing. *Nature Materials* **16**, 303-308 (2017).
48. Y. S. Zhang, J. Aleman, S. R. Shin, T. Kilic, D. Kim, S. A. Mousavi Shaegh, S. Massa, R. Riahi, S. Chae, N. Hu, H. Avci, W. Zhang, A. Silvestri, A. Sanati Nezhad, A. Manbohi, F. De Ferrari, A. Polini, G. Calzone, N. Shaikh, P. Alerasool, E. Budina, J. Kang, N. Bhise, J. Ribas, A. Pourmand, A. Skardal, T. Shupe, C. E. Bishop, M. R. Dokmeci, A. Atala, A. Khademhosseini, Multisensor-Integrated Organs-on-Chips Platform for Automated and Continual in Situ Monitoring of Organoid Behaviors. *Proceedings of the National Academy of Sciences* **114**, E2293-E2302 (2017).
49. W.-H. Yeo, R. C. Webb, W. Lee, S. Jung, J. A. Rogers, Bio-Integrated Electronics and Sensor Systems, in *SPIE's Micro-and Nanotechnology Sensors, Systems, and Applications V* (Vol. 8725). (International Society for Optics and Photonics, 2013), p. 87251I.

50. Y. H. Zhang, R. C. Webb, H. Y. Luo, Y. G. Xue, J. Kurniawan, N. H. Cho, S. Krishnan, Y. H. Li, Y. G. Huang, J. A. Rogers, Theoretical and Experimental Studies of Epidermal Heat Flux Sensors for Measurements of Core Body Temperature. *Advanced Healthcare Materials* **5**, 119-127 (2016).
51. S. Z. Guo, K. Qiu, F. Meng, S. H. Park, M. C. McAlpine, 3d Printed Stretchable Tactile Sensors. *Advanced Materials* **29**, 1701218 (2017).
52. M. S. Mannoor, H. Tao, J. D. Clayton, A. Sengupta, D. L. Kaplan, R. R. Naik, N. Verma, F. G. Omenetto, M. C. McAlpine, Graphene-Based Wireless Bacteria Detection on Tooth Enamel. *Nature Communications* **3**, 763 (2012).
53. C. Dagdeviren, B. D. Yang, Y. Su, P. L. Tran, P. Joe, E. Anderson, J. Xia, V. Doraiswamy, B. Dehdashti, X. Feng, B. Lu, R. Poston, Z. Khalpey, R. Ghaffari, Y. Huang, M. J. Slepian, J. A. Rogers, Conformal Piezoelectric Energy Harvesting and Storage from Motions of the Heart, Lung, and Diaphragm. *Proceedings of the National Academy of Sciences* **111**, 1927-1932 (2014).
54. B. Lu, Y. Chen, D. Ou, H. Chen, L. Diao, W. Zhang, J. Zheng, W. Ma, L. Sun, X. Feng, Ultra-Flexible Piezoelectric Devices Integrated with Heart to Harvest the Biomechanical Energy. *Scientific Reports* **5**, 16065 (2015).
55. S. Laufer, K. Rasske, L. Stopfer, C. Kurzynski, T. Abbott, M. Platner, J. Towles, C. M. Pugh, Fabric Force Sensors for the Clinical Breast Examination Simulator. *Studies in Health Technology and Informatics* **220**, 193-198 (2016).
56. L. H. Poniatowski, J. S. Wolf, Jr., S. Y. Nakada, T. E. Reihsen, F. Sainfort, R. M. Sweet, Validity and Acceptability of a High-Fidelity Physical Simulation Model for Training of Laparoscopic Pyeloplasty. *Journal of Endourology* **28**, 393-398 (2014).
57. F. Carpi, R. Kornbluh, P. Sommer-Larsen, G. Alici, Electroactive Polymer Actuators as Artificial Muscles: Are They Ready for Bioinspired Applications? *Bioinspiration & Biomimetics* **6**, 045006 (2011).
58. D. Trivedi, C. D. Rahn, W. M. Kier, I. D. Walker, Soft Robotics: Biological Inspiration, State of the Art, and Future Research. *Applied Bionics and Biomechanics* **5**, 99-117 (2008).
59. R. D. Kornbluh, R. Pelrine, Q. Pei, R. Heydt, S. Stanford, S. Oh, J. Eckerle, Electroelastomers: Applications of Dielectric Elastomer Transducers for Actuation, Generation, and Smart Structures, in *SPIE's Smart Structures and Materials 2002: Industrial and Commercial Applications of Smart Structures Technologies* (Vol. 4698). (International Society for Optics and Photonics, 2002), pp. 254-270.
60. R. Pelrine, R. D. Kornbluh, Q. Pei, S. Stanford, S. Oh, J. Eckerle, R. J. Full, M. A. Rosenthal, K. Meijer, Dielectric Elastomer Artificial Muscle Actuators: Toward Biomimetic Motion, in *SPIE's Smart Structures and Materials 2002: Electroactive Polymer Actuators and Devices (EAPAD)* (Vol. 4695). (International Society for Optics and Photonics, 2002), pp. 126-137.
61. R. Kornbluh, R. Pelrine, High-Performance Acrylic and Silicone Elastomers, in *Dielectric Elastomers as Electromechanical Transducers: Fundamentals, Materials, Devices, Models and Applications of an Emerging Electroactive Polymer Technology*, 33-42 (Elsevier, 2008).

62. S. Chiba, Dielectric Elastomers, in *Soft Actuators: Materials, Modeling, Applications, and Future Perspectives*, K. Asaka, H. Okuzaki, Eds., 183-195 (Springer Japan, Tokyo, 2014).
63. L. Romasanta, M. Lopez-Manchado, R. Verdejo, Increasing the Performance of Dielectric Elastomer Actuators: A Review from the Materials Perspective. *Progress in Polymer Science* **51**, 188-211 (2015).
64. R. Kornbluh, Fundamental Configurations for Dielectric Elastomer Actuators, in *Dielectric Elastomers as Electromechanical Transducers: Fundamentals, Materials, Devices, Models and Applications of an Emerging Electroactive Polymer Technology*, 79-90 (Elsevier, 2008).
65. F. Carpi, D. De Rossi, R. Kornbluh, R. E. Pelrine, P. Sommer-Larsen, *Dielectric Elastomers as Electromechanical Transducers: Fundamentals, Materials, Devices, Models and Applications of an Emerging Electroactive Polymer Technology*. (Elsevier, 2008).
66. W. Li, B. Belmont, J. M. Greve, A. B. Manders, B. C. Downey, X. Zhang, Z. Xu, D. Guo, A. Shih, Polyvinyl Chloride as a Multimodal Tissue-Mimicking Material with Tuned Mechanical and Medical Imaging Properties. *Medical Physics* **43**, 5577-5592 (2016).
67. M. O. Culjat, D. Goldenberg, P. Tewari, R. S. Singh, A Review of Tissue Substitutes for Ultrasound Imaging. *Ultrasound in Medicine & Biology* **36**, 861-873 (2010).
68. M. Lazebnik, E. L. Madsen, G. R. Frank, S. C. Hagness, Tissue-Mimicking Phantom Materials for Narrowband and Ultrawideband Microwave Applications. *Physics in Medicine & Biology* **50**, 4245-4258 (2005).
69. A. I. Farrer, H. Odeen, J. de Bever, B. Coats, D. L. Parker, A. Payne, D. A. Christensen, Characterization and Evaluation of Tissue-Mimicking Gelatin Phantoms for Use with MRgFUS. *Journal of Therapeutic Ultrasound* **3**, 9 (2015).
70. P. Brzozowski, K. I. Penev, F. M. Martinez, T. J. Scholl, K. Mequanint, Gellan Gum-Based Gels with Tunable Relaxation Properties for MRI Phantoms. *Magnetic Resonance Imaging* **57**, 40-49 (2019).
71. S. Langeland, J. D'Hooge, T. Claessens, P. Claus, P. Verdonck, P. Suetens, G. R. Sutherland, B. Bijnens, RF-Based Two-Dimensional Cardiac Strain Estimation: A Validation Study in a Tissue-Mimicking Phantom. *IEEE transactions on ultrasonics, ferroelectrics, and frequency control* **51**, 1537-1546 (2004).
72. M. Belohlavek, V. B. Bartleson, M. E. Zobitz, Real-Time Strain Rate Imaging: Validation of Peak Compression and Expansion Rates by a Tissue-Mimicking Phantom. *Echocardiography* **18**, 565-571 (2001).
73. M. McDonald, S. Lochhead, R. Chopra, M. J. Bronskill, Multi-Modality Tissue-Mimicking Phantom for Thermal Therapy. *Physics in Medicine & Biology* **49**, 2767-2778 (2004).
74. Y. Yuan, C. Wyatt, P. Maccarini, P. Stauffer, O. Craciunescu, J. Macfall, M. Dewhirst, S. K. Das, A Heterogeneous Human Tissue Mimicking Phantom for RF Heating and MRI Thermal Monitoring Verification. *Physics in Medicine & Biology* **57**, 2021-2037 (2012).

75. F. Adams, T. Qiu, A. Mark, B. Fritz, L. Kramer, D. Schlager, U. Wetterauer, A. Miernik, P. Fischer, Soft 3d-Printed Phantom of the Human Kidney with Collecting System. *Annals of Biomedical Engineering* **45**, 963-972 (2017).
76. R. Öpik, A. Hunt, A. Ristolainen, P. M. Aubin, M. Kruusmaa, Development of High Fidelity Liver and Kidney Phantom Organs for Use with Robotic Surgical Systems, in *2012 4th IEEE RAS & EMBS International Conference on Biomedical Robotics and Biomechatronics (BioRob)*. (IEEE, 2012), pp. 425-430.
77. J. R. Cook, R. R. Bouchard, S. Y. Emelianov, Tissue-Mimicking Phantoms for Photoacoustic and Ultrasonic Imaging. *Biomedical Optics Express* **2**, 3193-3206 (2011).
78. S. Inglis, K. V. Ramnarine, J. N. Plevris, W. N. McDicken, An Anthropomorphic Tissue-Mimicking Phantom of the Oesophagus for Endoscopic Ultrasound. *Ultrasound in Medicine & Biology* **32**, 249-259 (2006).
79. R. G. Holt, R. A. Roy, Measurements of Bubble-Enhanced Heating from Focused, MHz-Frequency Ultrasound in a Tissue-Mimicking Material. *Ultrasound in Medicine & Biology* **27**, 1399-1412 (2001).
80. E. L. Madsen, J. A. Zagzebski, R. A. Banjavie, R. E. Jutila, Tissue Mimicking Materials for Ultrasound Phantoms. *Medical Physics* **5**, 391-394 (1978).
81. M. Baba, K. Matsumoto, N. Yamasaki, H. Shindo, H. Yano, M. Matsumoto, R. Otsubo, M. John Lawn, N. Matsuo, I. Yamamoto, S. Hidaka, T. Nagayasu, Development of a Tailored Thyroid Gland Phantom for Fine-Needle Aspiration Cytology by Three-Dimensional Printing. *Journal of Surgical Education* **74**, 1039-1046 (2017).
82. K. L. Lurie, G. T. Smith, S. A. Khan, J. C. Liao, A. K. Ellerbee, Three-Dimensional, Distendable Bladder Phantom for Optical Coherence Tomography and White Light Cystoscopy. *Journal of Biomedical Optics* **19**, 36009 (2014).
83. S. Shen, H. Wang, Y. Xue, L. Yuan, X. Zhou, Z. Zhao, E. Dong, B. Liu, W. Liu, B. Cromeens, B. Adler, G. Besner, R. X. Xu, Freeform Fabrication of Tissue-Simulating Phantom for Potential Use of Surgical Planning in Conjoined Twins Separation Surgery. *Scientific Reports* **7**, 11048 (2017).
84. B. Wang, B. Stender, T. Long, Z. Zhang, A. Schlaefer, An Approach to Validate Ultrasound Surface Segmentation of the Heart. *Biomedical Engineering/Biomedizinische Technik* **58**, (2013).
85. S. J. Chen, P. Hellier, M. Marchal, J. Y. Gauvrit, R. Carpentier, X. Morandi, D. L. Collins, An Anthropomorphic Polyvinyl Alcohol Brain Phantom Based on Colin27 for Use in Multimodal Imaging. *Medical Physics* **39**, 554-561 (2012).
86. N. Kadoya, Y. Miyasaka, Y. Nakajima, Y. Kuroda, K. Ito, M. Chiba, K. Sato, S. Dobashi, T. Yamamoto, N. Takahashi, Evaluation of Deformable Image Registration between External Beam Radiotherapy and HDR Brachytherapy for Cervical Cancer with a 3d-Printed Deformable Pelvis Phantom. *Medical Physics* **44**, 1445-1455 (2017).
87. A. E. Forte, S. Galvan, F. Manieri, F. R. Y. Baena, D. Dini, A Composite Hydrogel for Brain Tissue Phantoms. *Materials & Design* **112**, 227-238 (2016).

88. K. Knox, C. W. Kerber, S. A. Singel, M. J. Bailey, S. G. Imbesi, Stereolithographic Vascular Replicas from CT Scans: Choosing Treatment Strategies, Teaching, and Research from Live Patient Scan Data. *American Journal of Neuroradiology* **26**, 1428-1431 (2005).
89. L. Allard, G. Soulez, B. Chayer, Z. Qin, D. Roy, G. Cloutier, A Multimodality Vascular Imaging Phantom of an Abdominal Aortic Aneurysm with a Visible Thrombus. *Medical Physics* **40**, 063701 (2013).
90. C. C. Ploch, C. Mansi, J. Jayamohan, E. Kuhl, Using 3d Printing to Create Personalized Brain Models for Neurosurgical Training and Preoperative Planning. *World Neurosurgery* **90**, 668-674 (2016).
91. M. Kalejs, L. K. von Segesser, Rapid Prototyping of Compliant Human Aortic Roots for Assessment of Valved Stents. *Interactive Cardiovascular and Thoracic Surgery* **8**, 182-186 (2009).
92. N. Stein, T. Saathoff, S.-T. Antoni, A. Schlaefer, Creating 3d Gelatin Phantoms for Experimental Evaluation in Biomedicine. *Current Directions in Biomedical Engineering* **1**, 331-334 (2015).
93. B. W. Pogue, M. S. Patterson, Review of Tissue Simulating Phantoms for Optical Spectroscopy, Imaging and Dosimetry. *Journal of Biomedical Optics* **11**, 041102 (2006).
94. M. K. Chmarra, R. Hansen, R. Marvik, T. Lango, Multimodal Phantom of Liver Tissue. *PLoS One* **8**, e64180 (2013).
95. M. Czerner, L. A. Fasce, J. F. Martucci, R. Ruseckaite, P. M. Frontini, Deformation and Fracture Behavior of Physical Gelatin Gel Systems. *Food Hydrocolloids* **60**, 299-307 (2016).
96. M. Czerner, J. F. Martucci, L. A. Fasce, R. A. Ruseckaite, P. M. Frontini, Mechanical and Fracture Behavior of Gelatin Gels, in *13th International Conference on Fracture* (2013).
97. L. Xie, M. Jiang, X. G. Dong, X. Bai, J. Tong, J. Zhou, Controlled Mechanical and Swelling Properties of Poly(Vinyl Alcohol)/Sodium Alginate Blend Hydrogels Prepared by Freeze-Thaw Followed by Ca²⁺ Crosslinking. *Journal of Applied Polymer Science* **124**, 823-831 (2012).
98. J. A. Lewis, Novel Inks for Direct-Write Assembly of 3-D Periodic Structures. *Material Matters* **3**, 4-7 (2008).
99. J. A. Lewis, Direct Ink Writing of 3d Functional Materials. *Advanced Functional Materials* **16**, 2193-2204 (2006).
100. P. Abdel-Sayed, M. Kalejs, L. K. von Segesser, A New Training Set-up for Trans-Apical Aortic Valve Replacement. *Interactive Cardiovascular and Thoracic Surgery* **8**, 599-601 (2009).
101. F. C. von Rundstedt, J. M. Scovell, S. Agrawal, J. Zaneveld, R. E. Link, Utility of Patient-Specific Silicone Renal Models for Planning and Rehearsal of Complex Tumour Resections Prior to Robot-Assisted Laparoscopic Partial Nephrectomy. *BJU International* **119**, 598-604 (2017).

102. J. Liu, H. Zheng, P. S. Poh, H.-G. Machens, A. F. Schilling, Hydrogels for Engineering of Perfusable Vascular Networks. *International Journal of Molecular Sciences* **16**, 15997-16016 (2015).
103. G. A. Schuster, T. G. Schuster, The Relative Amount of Epithelium, Muscle, Connective Tissue and Lumen in Prostatic Hyperplasia as a Function of the Mass of Tissue Resected. *Journal of Urology* **161**, 1168-1173 (1999).
104. P. A. Huijing, Muscle as a Collagen Fiber Reinforced Composite: A Review of Force Transmission in Muscle and Whole Limb. *Journal of Biomechanics* **32**, 329-345 (1999).
105. J. T. Muth, D. M. Vogt, R. L. Truby, Y. Mengüç, D. B. Kolesky, R. J. Wood, J. A. Lewis, Embedded 3d Printing of Strain Sensors within Highly Stretchable Elastomers. *Advanced Materials* **26**, 6307-6312 (2014).
106. B. Wang, A. Borazjani, M. Tahai, A. L. Curry, D. T. Simionescu, J. Guan, F. To, S. H. Elder, J. Liao, Fabrication of Cardiac Patch with Decellularized Porcine Myocardial Scaffold and Bone Marrow Mononuclear Cells. *Journal of Biomedical Materials Research Part A* **94**, 1100-1110 (2010).
107. N. Poornejad, T. S. Frost, D. R. Scott, B. B. Elton, P. R. Reynolds, B. L. Roeder, A. D. Cook, Freezing/Thawing without Cryoprotectant Damages Native but Not Decellularized Porcine Renal Tissue. *Organogenesis* **11**, 30-45 (2015).
108. Ninjabot Technical Specifications for Ninjabot® 3d Printing Filament, <https://ninjabot.com/wp-content/uploads/2016/05/Ninjabot-TDS.pdf>.
109. Ninjabot Technical Specification for Semiflex™ 3d Printing Filament, <https://ninjabot.com/wp-content/uploads/2016/05/SemiFlex-TDS.pdf>.
110. Polymaker Technical Data Sheet for Polyflex™ 3d Printing Filament, https://www.lulzbot.com/sites/default/files/PolyFlex_TDS-v1.pdf.
111. K. Baeck, P. Lopes, G. Biglino, C. Capelli, P. Verschueren, in *3rd Joint Workshop on New Technologies for Computer Robot Assisted Surgery*. (Verona, Italy, 2013).
112. Objet Geometries Inc. Technical Data Sheet for Fullcure®930 Tangoplus, <http://www.intechrp.com/wp-content/uploads/2012/09/TangoFamily.pdf>.
113. Stratasys Polyjet Materials Technical Data Sheet, http://usglobalimages.stratasys.com/Main/Files/Material_Spec_Sheets/MSS_PJ_PJMaterialsDataSheet.pdf?v=635785205440671440.
114. B. M. Tymrak, M. Kreiger, J. M. Pearce, Mechanical Properties of Components Fabricated with Open-Source 3-D Printers under Realistic Environmental Conditions. *Materials & Design* **58**, 242-246 (2014).
115. S. Hassanipour-Azgomi, A. Mohammadian-Hafshejani, M. Ghoncheh, F. Towhidi, S. Jamehshorani, H. Salehiniya, Incidence and Mortality of Prostate Cancer and Their Relationship with the Human Development Index Worldwide. *Prostate International* **4**, 118-124 (2016).
116. P. N. Wells, H.-D. Liang, Medical Ultrasound: Imaging of Soft Tissue Strain and Elasticity. *Journal of the Royal Society Interface* **8**, 1521-1549 (2011).
117. T. A. Krouskop, T. M. Wheeler, F. Kallel, B. S. Garra, T. Hall, Elastic Moduli of Breast and Prostate Tissues under Compression. *Ultrasonic Imaging* **20**, 260-274 (1998).

118. R. J. Dewall, T. Varghese, M. A. Kliewer, J. M. Harter, E. M. Hartenbach, Compression-Dependent Viscoelastic Behavior of Human Cervix Tissue. *Ultrasonic Imaging* **32**, 214-228 (2010).
119. M. Zhang, P. Nigwekar, B. Castaneda, K. Hoyt, J. V. Joseph, A. di Sant'Agnese, E. M. Messing, J. G. Strang, D. J. Rubens, K. J. Parker, Quantitative Characterization of Viscoelastic Properties of Human Prostate Correlated with Histology. *Ultrasound in Medicine & Biology* **34**, 1033-1042 (2008).
120. W. Shui, M. Zhou, S. Chen, Z. Pan, Q. Deng, Y. Yao, H. Pan, T. He, X. Wang, The Production of Digital and Printed Resources from Multiple Modalities Using Visualization and Three-Dimensional Printing Techniques. *International Journal of Computer Assisted Radiology and Surgery* **12**, 13-23 (2017).
121. M. Antonietti, P. Fratzl, Biomimetic Principles in Polymer and Material Science. *Macromolecular Chemistry and Physics* **211**, 166-170 (2010).
122. S. Quinn, W. Gaughran, Bionics-an Inspiration for Intelligent Manufacturing and Engineering. *Robotics and Computer-Integrated Manufacturing* **26**, 616-621 (2010).
123. D. Rus, M. T. Tolley, Design, Fabrication and Control of Soft Robots. *Nature* **521**, 467-475 (2015).
124. C. Majidi, Soft Robotics: A Perspective-Current Trends and Prospects for the Future. *Soft Robotics* **1**, 5-11 (2014).
125. S. Kim, C. Laschi, B. Trimmer, Soft Robotics: A Bioinspired Evolution in Robotics. *Trends in Biotechnology* **31**, 287-294 (2013).
126. J. T. Bauman, in *Fatigue, Stress, and Strain of Rubber Components: Guide for Design Engineers*. (Carl Hanser Verlag GmbH Co KG, 2012), pp. 9-18.
127. R. A. Shanks, I. Kong, in *Advances in Elastomers I: Blends and Interpenetrating Networks*, P. M. Visakh, S. Thomas, A. K. Chandra, A. P. Mathew, Eds. (Springer Berlin Heidelberg, Berlin, Heidelberg, 2013), pp. 11-45.
128. C. Keplinger, J.-Y. Sun, C. C. Foo, P. Rothemund, G. M. Whitesides, Z. Suo, Stretchable, Transparent, Ionic Conductors. *Science* **341**, 984-987 (2013).
129. H. Yuk, T. Zhang, G. A. Parada, X. Liu, X. Zhao, Skin-Inspired Hydrogel-Elastomer Hybrids with Robust Interfaces and Functional Microstructures. *Nature Communications* **7**, 12028 (2016).
130. J. Y. Sun, C. Keplinger, G. M. Whitesides, Z. Suo, Ionic Skin. *Advanced Materials* **26**, 7608-7614 (2014).
131. S. S. Robinson, K. W. O'Brien, H. Zhaob, B. N. Peele, C. M. Larson, B. C. Mac Murray, I. M. Van Meerbeek, S. N. Dunham, R. F. Shepherd, Integrated Soft Sensors and Elastomeric Actuators for Tactile Machines with Kinesthetic Sense. *Extreme Mechanics Letters* **5**, 47-53 (2015).
132. K. Tian, J. Bae, S. E. Bakarich, C. Yang, R. D. Gately, G. M. Spinks, M. In Het Panhuis, Z. Suo, J. J. Vlassak, 3d Printing of Transparent and Conductive Heterogeneous Hydrogel-Elastomer Systems. *Advanced Materials* **29**, 1604827 (2017).

133. Z. Lei, Q. Wang, S. Sun, W. Zhu, P. Wu, A Bioinspired Mineral Hydrogel as a Self-Healable, Mechanically Adaptable Ionic Skin for Highly Sensitive Pressure Sensing. *Advanced Materials* **29**, (2017).
134. B. H. Chen, Y. Y. Bai, F. Xiang, J. Y. Sun, Y. M. Chen, H. Wang, J. X. Zhou, Z. G. Suo, Stretchable and Transparent Hydrogels as Soft Conductors for Dielectric Elastomer Actuators. *Journal of Polymer Science Part B: Polymer Physics* **52**, 1055-1060 (2014).
135. K. Parida, V. Kumar, W. Jiangxin, V. Bhavanasi, R. Bendi, P. S. Lee, Highly Transparent, Stretchable, and Self-Healing Ionic-Skin Triboelectric Nanogenerators for Energy Harvesting and Touch Applications. *Advanced Materials* **29**, (2017).
136. C. Larson, B. Peele, S. Li, S. Robinson, M. Totaro, L. Beccai, B. Mazzolai, R. Shepherd, Highly Stretchable Electroluminescent Skin for Optical Signaling and Tactile Sensing. *Science* **351**, 1071-1074 (2016).
137. C. H. Yang, B. Chen, J. Zhou, Y. M. Chen, Z. Suo, Electroluminescence of Giant Stretchability. *Advanced Materials* **28**, 4480-4484 (2016).
138. C. H. Yang, B. H. Chen, J. J. Lu, J. H. Yang, J. X. Zhou, Y. M. Chen, Z. G. Suo, Ionic Cable. *Extreme Mechanics Letters* **3**, 59-65 (2015).
139. M. Wehner, R. L. Truby, D. J. Fitzgerald, B. Mosadegh, G. M. Whitesides, J. A. Lewis, R. J. Wood, An Integrated Design and Fabrication Strategy for Entirely Soft, Autonomous Robots. *Nature* **536**, 451-455 (2016).
140. G. K. Lau, S. C. K. Goh, L. L. Shiau, Dielectric Elastomer Unimorph Using Flexible Electrodes of Electrolessly Deposited (Eld) Silver. *Sensors and Actuators A: Physical* **169**, 234-241 (2011).
141. Y. Y. Bai, B. H. Chen, F. Xiang, J. X. Zhou, H. Wang, Z. G. Suo, Transparent Hydrogel with Enhanced Water Retention Capacity by Introducing Highly Hydratable Salt. *Applied Physics Letters* **105**, 151903 (2014).
142. S. Michel, X. Q. Q. Zhang, M. Wissler, C. Lowe, G. Kovacs, A Comparison between Silicone and Acrylic Elastomers as Dielectric Materials in Electroactive Polymer Actuators. *Polymer International* **59**, 391-399 (2010).
143. M. Vijatović, J. Bobić, B. Stojanović, History and Challenges of Barium Titanate: Part II. *Science of Sintering* **40**, 235-244 (2008).
144. L. Jiang, A. Betts, D. Kennedy, S. Jerrams, The Fabrication of Dielectric Elastomers from Silicone Rubber and Barium Titanate: Employing Equi-Biaxial Pre-Stretch to Achieve Large Deformations. *Journal of Materials Science* **50**, 7930-7938 (2015).
145. A. Bele, M. Cazacu, G. Stiubianu, S. Vlad, Silicone-Barium Titanate Composites with Increased Electromechanical Sensitivity. The Effects of the Filler Morphology. *RSC Advances* **4**, 58522-58529 (2014).
146. L. Cai, S. Zhang, J. Miao, Z. Yu, C. Wang, Fully Printed Stretchable Thin-Film Transistors and Integrated Logic Circuits. *ACS Nano* **10**, 11459-11468 (2016).
147. C. Guo, M. Fuji, Effect of Silicone Coupling Agent on Dielectric Properties of Barium Titanate/Silicone Elastomer Composites. *Advanced Powder Technology* **27**, 1162-1172 (2016).

148. D. Bodas, C. Khan-Malek, Hydrophilization and Hydrophobic Recovery of PDMS by Oxygen Plasma and Chemical Treatment—an SEM Investigation. *Sensors and Actuators B: Chemical* **123**, 368-373 (2007).
149. J. Zhou, D. A. Khodakov, A. V. Ellis, N. H. Voelcker, Surface Modification for PDMS-Based Microfluidic Devices. *Electrophoresis* **33**, 89-104 (2012).
150. S. Hu, X. Ren, M. Bachman, C. E. Sims, G. P. Li, N. L. Allbritton, Surface-Directed, Graft Polymerization within Microfluidic Channels. *Analytical Chemistry* **76**, 1865-1870 (2004).
151. M. H. Schneider, H. Willaime, Y. Tran, F. Rezgui, P. Tabeling, Wettability Patterning by UV-Initiated Graft Polymerization of Poly(Acrylic Acid) in Closed Microfluidic Systems of Complex Geometry. *Analytical Chemistry* **82**, 8848-8855 (2010).
152. M. H. Schneider, Y. Tran, P. Tabeling, Benzophenone Absorption and Diffusion in Poly(Dimethylsiloxane) and Its Role in Graft Photo-Polymerization for Surface Modification. *Langmuir* **27**, 1232-1240 (2011).
153. A. Nayfeh, P. Pai, *Linear and Nonlinear Structural Mechanics*. (Jon Wiley & Sons, 2004).
154. I. Chopra, J. Sirohi, *Smart Structures Theory*. (Cambridge University Press, 2013), vol. 35.
155. E. Habtour, D. P. Cole, S. C. Stanton, R. Sridharan, A. Dasgupta, Damage Precursor Detection for Structures Subjected to Rotational Base Vibration. *International Journal of Non-Linear Mechanics* **82**, 49-58 (2016).
156. K. Kadooka, H. Imamura, M. Taya, Experimentally Verified Model of Viscoelastic Behavior of Multilayer Unimorph Dielectric Elastomer Actuators. *Smart Materials and Structures* **25**, 105028 (2016).
157. J. Sirohi, I. Chopra, Fundamental Understanding of Piezoelectric Strain Sensors. *Journal of Intelligent Material Systems and Structures* **11**, 246-257 (2000).
158. A. Labuschagne, N. F. J. van Rensburg, A. J. van der Merwe, Comparison of Linear Beam Theories. *Mathematical and Computer Modelling* **49**, 20-30 (2009).
159. R. J. Wood, E. Steltz, R. S. Fearing, Optimal Energy Density Piezoelectric Bending Actuators. *Sensors and Actuators A: Physical* **119**, 476-488 (2005).
160. M. Duduta, R. J. Wood, D. R. Clarke, Multilayer Dielectric Elastomers for Fast, Programmable Actuation without Prestretch. *Advanced Materials* **28**, 8058-8063 (2016).
161. G. Y. Gu, U. Gupta, J. Zhu, L. M. Zhu, X. Y. Zhu, Modeling of Viscoelastic Electromechanical Behavior in a Soft Dielectric Elastomer Actuator. *IEEE Transactions on Robotics* **33**, 1263-1271 (2017).
162. J. S. Zhang, J. Ru, H. L. Chen, D. C. Li, J. Lu, Viscoelastic Creep and Relaxation of Dielectric Elastomers Characterized by a Kelvin-Voigt-Maxwell Model. *Applied Physics Letters* **110**, 044104 (2017).
163. A. York, J. Dunn, S. Seelecke, Experimental Characterization of the Hysteretic and Rate-Dependent Electromechanical Behavior of Dielectric Electro-Active Polymer Actuators. *Smart Materials and Structures* **19**, 094014 (2010).

164. L. Jiang, A. Betts, D. Kennedy, S. Jerrams, Improving the Electromechanical Performance of Dielectric Elastomers Using Silicone Rubber and Dopamine Coated Barium Titanate. *Materials & Design* **85**, 733-742 (2015).
165. O. A. Araromi, S. C. Burgess, A Finite Element Approach for Modelling Multilayer Unimorph Dielectric Elastomer Actuators with Inhomogeneous Layer Geometry. *Smart Materials and Structures* **21**, 032001 (2012).
166. J. Vespa, D. M. Armstrong, L. Medina, *Demographic Turning Points for the United States: Population Projections for 2020 to 2060*. (US Department of Commerce, Economics and Statistics Administration, US, 2018).
167. J. L. Fleg, J. Strait, Age-Associated Changes in Cardiovascular Structure and Function: A Fertile Milieu for Future Disease. *Heart Failure Reviews* **17**, 545-554 (2012).
168. R. L. Osnabrugge, D. Mylotte, S. J. Head, N. M. Van Mieghem, V. T. Nkomo, C. M. LeReun, A. J. Bogers, N. Piazza, A. P. Kappetein, Aortic Stenosis in the Elderly: Disease Prevalence and Number of Candidates for Transcatheter Aortic Valve Replacement: A Meta-Analysis and Modeling Study. *Journal of the American College of Cardiology* **62**, 1002-1012 (2013).
169. B. R. Lindman, M.-A. Clavel, P. Mathieu, B. Iung, P. Lancellotti, C. M. Otto, P. Pibarot, Calcific Aortic Stenosis. *Nature Reviews Disease Primers* **2**, 16006 (2016).
170. N. Bhatia, S. S. Basra, A. H. Skolnick, N. K. Wenger, Aortic Valve Disease in the Older Adult. *Journal of Geriatric Cardiology: JGC* **13**, 941 (2016).
171. M. Eleid, Interventional Management of Paravalvular Leak. *Heart* **104**, 1797-1802 (2018).
172. J. J. Bax, V. Delgado, V. Bapat, H. Baumgartner, J. P. Collet, R. Erbel, C. Hamm, A. P. Kappetein, J. Leipsic, M. B. Leon, Open Issues in Transcatheter Aortic Valve Implantation. Part 2: Procedural Issues and Outcomes after Transcatheter Aortic Valve Implantation. *European Heart Journal* **35**, 2639-2654 (2014).
173. M. Y. Lee, S. C. Yeshwant, S. Chava, D. L. Lustgarten, Mechanisms of Heart Block after Transcatheter Aortic Valve Replacement—Cardiac Anatomy, Clinical Predictors and Mechanical Factors That Contribute to Permanent Pacemaker Implantation. *Arrhythmia & Electrophysiology Review* **4**, 81 (2015).
174. N. Piazza, P. de Jaegere, C. Schultz, A. E. Becker, P. W. Serruys, R. H. Anderson, Anatomy of the Aortic Valvar Complex and Its Implications for Transcatheter Implantation of the Aortic Valve. *Circulation: Cardiovascular Interventions* **1**, 74-81 (2008).
175. B. A. Oestreich, M. Mbai, S. Gurevich, P. S. Nijjar, S. Adabag, S. Bertog, R. Kelly, S. Garcia, Computed Tomography (CT) Assessment of the Membranous Septal Anatomy Prior to Transcatheter Aortic Valve Replacement (TAVR) with the Balloon-Expandable Sapien 3 Valve. *Cardiovascular Revascularization Medicine* **19**, 626-631 (2018).
176. A. Hamdan, V. Guetta, R. Klempfner, E. Konen, E. Raanani, M. Glikson, O. Goitein, A. Segev, I. Barbash, P. Fefer, Inverse Relationship between Membranous Septal Length and the Risk of Atrioventricular Block in Patients Undergoing

- Transcatheter Aortic Valve Implantation. *JACC: Cardiovascular Interventions* **8**, 1218-1228 (2015).
177. R.-J. Nuis, N. M. Van Mieghem, C. J. Schultz, A. Tzikas, R. M. Van der Boon, A.-M. Maugeness, J. Cheng, N. Piazza, R. T. Van Domburg, P. W. Serruys, Timing and Potential Mechanisms of New Conduction Abnormalities During the Implantation of the Medtronic Corevalve System in Patients with Aortic Stenosis. *European Heart Journal* **32**, 2067-2074 (2011).
 178. B. Fujita, M. Kütting, M. Seiffert, S. Scholtz, S. Egron, E. Prashovikj, J. Börgermann, T. Schäfer, W. Scholtz, R. Preuss, Calcium Distribution Patterns of the Aortic Valve as a Risk Factor for the Need of Permanent Pacemaker Implantation after Transcatheter Aortic Valve Implantation. *European Journal of Echocardiography* **17**, 1385-1393 (2016).
 179. G. C. Siontis, P. Jüni, T. Pilgrim, S. Stortecky, L. Büllsfeld, B. Meier, P. Wenaweser, S. Windecker, Predictors of Permanent Pacemaker Implantation in Patients with Severe Aortic Stenosis Undergoing TAVR: A Meta-Analysis. *Journal of the American College of Cardiology* **64**, 129-140 (2014).
 180. J. G. Almeida, S. M. Ferreira, P. Fonseca, T. Dias, C. Guerreiro, A. R. Barbosa, P. Teixeira, M. Carvalho, W. Ferreira, N. D. Ferreira, Association between Implantation Depth Assessed by Computed Tomography and New-Onset Conduction Disturbances after Transcatheter Aortic Valve Implantation. *Journal of Cardiovascular Computed Tomography* **11**, 332-337 (2017).
 181. S. Lerakis, S. S. Hayek, P. S. Douglas, Paravalvular Aortic Leak after Transcatheter Aortic Valve Replacement: Current Knowledge. *Circulation* **127**, 397-407 (2013).
 182. J.-M. Sinning, C. Hammerstingl, M. Vasa-Nicotera, V. Adenauer, S. J. L. Cachiguango, A.-C. Scheer, S. Hausen, A. Sedaghat, A. Ghanem, C. Müller, Aortic Regurgitation Index Defines Severity of Peri-Prosthetic Regurgitation and Predicts Outcome in Patients after Transcatheter Aortic Valve Implantation. *Journal of the American College of Cardiology* **59**, 1134-1141 (2012).
 183. K. Qiu, G. Haghiashtiani, M. C. McAlpine, 3d Printed Organ Models for Surgical Applications. *Annual Review of Analytical Chemistry* **11**, 287-306 (2018).
 184. M. Vukicevic, D. P. Vekilov, J. K. Grande-Allen, S. H. Little, Patient-Specific 3d Valve Modeling for Structural Intervention. *Structural Heart* **1**, 236-248 (2017).
 185. A. Hosny, J. D. Dilley, T. Kelil, M. Mathur, M. N. Dean, J. C. Weaver, B. Ripley, Pre-Procedural Fit-Testing of TAVR Valves Using Parametric Modeling and 3d Printing. *Journal of Cardiovascular Computed Tomography* **13**, 21-30 (2019).
 186. Z. Qian, K. Wang, S. Liu, X. Zhou, V. Rajagopal, C. Meduri, J. R. Kauten, Y.-H. Chang, C. Wu, C. Zhang, Quantitative Prediction of Paravalvular Leak in Transcatheter Aortic Valve Replacement Based on Tissue-Mimicking 3d Printing. *JACC: Cardiovascular Imaging* **10**, 719-731 (2017).
 187. D. Maragiannis, M. S. Jackson, S. R. Igo, R. C. Schutt, P. Connell, J. Grande-Allen, C. M. Barker, S. M. Chang, M. J. Reardon, W. A. Zoghbi, Replicating Patient-Specific Severe Aortic Valve Stenosis with Functional 3d Modeling. *Circulation: Cardiovascular Imaging* **8**, e003626 (2015).

188. B. Ripley, T. Kelil, M. K. Cheezum, A. Goncalves, M. F. Di Carli, F. J. Rybicki, M. Steigner, D. Mitsouras, R. Blankstein, 3d Printing Based on Cardiac CT Assists Anatomic Visualization Prior to Transcatheter Aortic Valve Replacement. *Journal of Cardiovascular Computed Tomography* **10**, 28-36 (2016).
189. A. Hasan, K. Ragaert, W. Swieszkowski, Š. Selimović, A. Paul, G. Camci-Unal, M. R. Mofrad, A. Khademhosseini, Biomechanical Properties of Native and Tissue Engineered Heart Valve Constructs. *Journal of Biomechanics* **47**, 1949-1963 (2014).
190. G. A. Holzapfel, Biomechanics of Soft Tissue. *The Handbook of Materials Behavior Models* **3**, 1049-1063 (2001).
191. S. Ramadan, N. Paul, H. E. Naguib, Standardized Static and Dynamic Evaluation of Myocardial Tissue Properties. *Biomedical Materials* **12**, 025013 (2017).
192. B. Wang, A. Borazjani, M. Tahai, A. L. de Jongh Curry, D. T. Simionescu, J. Guan, F. To, S. H. Elder, J. Liao, Fabrication of Cardiac Patch with Decellularized Porcine Myocardial Scaffold and Bone Marrow Mononuclear Cells. *Journal of Biomedical Materials Research Part A* **94**, 1100-1110 (2010).
193. K. J. Grande-Allen, R. P. Cochran, P. G. Reinhall, K. S. Kunzelman, Mechanisms of Aortic Valve Incompetence: Finite-Element Modeling of Marfan Syndrome. *The Journal of Thoracic and Cardiovascular Surgery* **122**, 946-954 (2001).
194. P. S. Robinson, S. L. Johnson, M. C. Evans, V. H. Barocas, R. T. Tranquillo, Functional Tissue-Engineered Valves from Cell-Remodeled Fibrin with Commissural Alignment of Cell-Produced Collagen. *Tissue Engineering Part A* **14**, 83-95 (2008).
195. A. S. Kamba, M. Ismail, T. A. T. Ibrahim, Z. A. B. Zakaria, Synthesis and Characterisation of Calcium Carbonate Aragonite Nanocrystals from Cockle Shell Powder (*Anadara Granosa*). *Journal of Nanomaterials* **2013**, 5 (2013).
196. A. Hamdan, V. Guetta, E. Konen, O. Goitein, A. Segev, E. Raanani, D. Spiegelstein, I. Hay, E. Di Segni, M. Eldar, Deformation Dynamics and Mechanical Properties of the Aortic Annulus by 4-Dimensional Computed Tomography: Insights into the Functional Anatomy of the Aortic Valve Complex and Implications for Transcatheter Aortic Valve Therapy. *Journal of the American College of Cardiology* **59**, 119-127 (2012).
197. W. M. Yarbrough, R. Mukherjee, J. S. Ikonomidis, M. R. Zile, F. G. Spinale, Myocardial Remodeling with Aortic Stenosis and after Aortic Valve Replacement: Mechanisms and Future Prognostic Implications. *The Journal of Thoracic and Cardiovascular Surgery* **143**, 656-664 (2012).
198. P. R. Vijayaratnam, C. C. O'Brien, J. A. Reizes, T. J. Barber, E. R. Edelman, The Impact of Blood Rheology on Drug Transport in Stented Arteries: Steady Simulations. *PloS One* **10**, e0128178 (2015).
199. T. G. Papaioannou, A. D. Protogerou, N. Stergiopoulos, O. Vardoulis, C. Stefanadis, M. Safar, J. Blacher, Total Arterial Compliance Estimated by a Novel Method and All-Cause Mortality in the Elderly: The Proteger Study. *Age* **36**, 9661 (2014).
200. D. Chemla, J.-L. Hébert, C. Coirault, K. Zamani, I. Suard, P. Colin, Y. Lecarpentier, Total Arterial Compliance Estimated by Stroke Volume-to-Aortic

- Pulse Pressure Ratio in Humans. *American Journal of Physiology: Heart and Circulatory Physiology* **274**, H500-H505 (1998).
201. M. Roşca, J. Magne, A. Călin, B. A. Popescu, L. A. Pierard, P. Lancellotti, Impact of Aortic Stiffness on Left Ventricular Function and B-Type Natriuretic Peptide Release in Severe Aortic Stenosis. *European Journal of Echocardiography* **12**, 850-856 (2011).
 202. S. G. Yazdi, P. Geoghegan, P. Docherty, M. Jermy, A. Khanafer, A Review of Arterial Phantom Fabrication Methods for Flow Measurement Using Piv Techniques. *Annals of Biomedical Engineering* **46**, 1697-1721 (2018).
 203. M. Briand, J. G. Dumesnil, L. Kadem, A. G. Tongue, R. Rieu, D. Garcia, P. Pibarot, Reduced Systemic Arterial Compliance Impacts Significantly on Left Ventricular Afterload and Function in Aortic Stenosis: Implications for Diagnosis and Treatment. *Journal of the American College of Cardiology* **46**, 291-298 (2005).
 204. H. Baumgartner, J. Hung, J. Bermejo, J. B. Chambers, A. Evangelista, B. P. Griffin, B. Iung, C. M. Otto, P. A. Pellikka, M. Quiñones, Echocardiographic Assessment of Valve Stenosis: EAE/ASE Recommendations for Clinical Practice. *Journal of the American Society of Echocardiography* **22**, 1-23 (2009).
 205. B. A. Carabello, W. J. Paulus, Aortic Stenosis. *The Lancet* **373**, 956-966 (2009).
 206. H. Sabbah, P. Stein, Effect of Aortic Stenosis on Coronary Flow Dynamics: Studies in an in-Vitro Pulse Duplicating System. *Journal of Biomechanical Engineering* **104**, 221-225 (1982).
 207. A.-H. Hakki, A. S. Iskandrian, C. E. Bemis, D. Kimbiris, G. S. Mintz, B. L. Segal, C. Brice, A Simplified Valve Formula for the Calculation of Stenotic Cardiac Valve Areas. *Circulation* **63**, 1050-1055 (1981).
 208. Y. Zhang, H. Ihlen, S. Nitter-Hauge, Estimation of the Peak-to-Peak Pressure Gradient in Aortic Stenosis by Doppler Echocardiography. *International Journal of Cardiology* **10**, 197-212 (1986).
 209. M. F. Eleid, A. K. Cabalka, J. F. Malouf, S. Sanon, D. J. Hagler, C. S. Rihal, Techniques and Outcomes for the Treatment of Paravalvular Leak. *Circulation: Cardiovascular Interventions* **8**, e001945 (2015).
 210. G. Rocatello, N. El Faquir, G. De Santis, F. Iannaccone, J. Bosmans, O. De Backer, L. Sondergaard, P. Segers, M. De Beule, P. de Jaegere, Patient-Specific Computer Simulation to Elucidate the Role of Contact Pressure in the Development of New Conduction Abnormalities after Catheter-Based Implantation of a Self-Expanding Aortic Valve. *Circulation: Cardiovascular Interventions* **11**, e005344 (2018).
 211. G. Rocatello, N. El Faquir, O. de Backer, M. J. Swaans, A. Latib, L. Vicentini, P. Segers, M. De Beule, P. de Jaegere, P. Mortier, The Impact of Size and Position of a Mechanical Expandable Transcatheter Aortic Valve: Novel Insights through Computational Modelling and Simulation. *Journal of Cardiovascular Translational Research* **12**, 435-446 (2019).
 212. B. N. Johnson, K. Z. Lancaster, G. Zhen, J. He, M. K. Gupta, Y. L. Kong, E. A. Engel, K. D. Krick, A. Ju, F. Meng, L. W. Enquist, X. Jia, M. C. McAlpine, 3d Printed Anatomical Nerve Regeneration Pathways. *Advanced Functional Materials* **25**, 6205-6217 (2015).

213. R. Zou, Y. Xia, S. Y. Liu, P. Hu, W. B. Hou, Q. Y. Hu, C. L. Shan, Isotropic and Anisotropic Elasticity and Yielding of 3d Printed Material. *Composites Part B-Engineering* **99**, 506-513 (2016).
214. K. Wang, Y. Zhao, Y.-H. Chang, Z. Qian, C. Zhang, B. Wang, M. A. Vannan, M.-J. Wang, Controlling the Mechanical Behavior of Dual-Material 3d Printed Meta-Materials for Patient-Specific Tissue-Mimicking Phantoms. *Materials & Design* **90**, 704-712 (2016).
215. T. A. Gisby, B. M. O'Brien, I. A. Anderson, Self Sensing Feedback for Dielectric Elastomer Actuators. *Applied Physics Letters* **102**, 193703 (2013).
216. S. Rosset, B. M. O'Brien, T. Gisby, D. Xu, H. R. Shea, I. A. Anderson, Self-Sensing Dielectric Elastomer Actuators in Closed-Loop Operation. *Smart Materials and Structures* **22**, 104018 (2013).
217. G. Rizzello, D. Naso, A. York, S. Seelecke, Closed Loop Control of Dielectric Elastomer Actuators Based on Self-Sensing Displacement Feedback. *Smart Materials and Structures* **25**, 035034 (2016).
218. T. Hoffstadt, J. Maas, Self-Sensing Control for Soft-Material Actuators Based on Dielectric Elastomers. *Frontiers in Robotics and AI* **6**, 133 (2019).

APPENDIX A

Supplementary Information for Chapter 2

A.1. 3D Printing Materials Formulation and Preparation

The material system mainly consists of silicone sealant (RTV silicone sealant SI 595 CL, Loctite) and silicone grease (LP20, Trident). For ink preparation, the active agent and bulking agent were mixed at specified weight ratios via a planetary centrifugal mixer (ARE-310, Thinky) at 2000 rpm for 6 minutes to form the customized polymeric inks with different properties. The prepared weight ratios of bulking agent to active agent for preliminary investigations were 0, 0.25, 0.4, 0.55, 0.70, 0.85, 1.00, 1.15, 1.3, 1.45, 1.75, and 2.05 to achieve different values of Young's modulus and stress-strain properties.

A.2. Mechanical Characterization of the Customized Polymeric Materials

For performing the compression tests, the polymeric materials with different formulations were printed into cylindrical samples with dimensions of ca. 8 mm × 5 mm (diameter × height). The tests were carried out using a mechanical analyzer (RSA-G2, TA Instruments) with an 8 mm parallel plate geometry and at a constant linear rate of ca. 0.0355 s⁻¹.

A.3. Sol-Gel and Stability Tests of the Customized Polymeric Materials in Hexane, Glycerol-Water, and Air

For analyzing the sol-gel fraction of the customized polymeric materials, rectangular samples were 3D printed with dimensions of 15 mm × 15 mm × 1.2 mm (length × width × height) using different ink formulations (weight ratios of bulking agent to active agent of 0, 0.25, 0.55, 0.85, 1.15, 1.45, and 1.75). First, the samples were weighed to obtain their initial dry weight (m_0) and then, were immersed in hexane solvent or glycerol-water solution with a volume ratio of 0.65:1.23 in glass vials. The glass vials containing the

samples immersed in the test solvent were placed on an orbital shaker (VWR, Model 3500) and were maintained at room temperature and ~250 rpm. At time intervals of 24, 48, 72 and 96 hours after immersion, the solid content of the samples were extracted from the test solution using a filter paper (P5 Grade, 09-801B, Fisher Scientific) to obtain potential residues. For samples immersed in water/glycerol, an additional rinsing step with distilled water was performed after removal from the solution. Next, these obtained samples were dried and their dry weights were measured. The measured weights were regarded as the weight of the crosslinked portion of the materials at each time interval (m_i). The weight losses ($\Delta m = m_i - m_0$) and the ratios of weight loss to initial weight of the samples ($\Delta m/m_0$) were then determined at each time interval as an indicator of the stability of the materials in each test solution. Similar measurements were performed by obtaining the weight changes of the samples in ambient air over the course of 96 hours in order to determine the stability of the polymeric materials in air.

A.4. Rheological Characterization of the Customized Polymeric Inks

Rheological characterization of the customized polymeric inks and their main constituents were performed on a magnetic bearing rheometer (AR-G2, TA Instruments) with a steel plate (25 mm diameter) Smart Swap geometry at 25 °C. Viscometry experiments were conducted via a logarithmic sweep of shear rate at 0.1-1000 s⁻¹ range with a 500 μm gap between the Smart Swap geometry and the lower geometry. Oscillatory rheometry experiments were conducted via a logarithmic sweep of oscillation shear stress at 0.1-1000 Pa range and frequency of 1 Hz with a 500 μm gap between the Smart Swap geometry and the lower geometry.

A.5. Mechanical Characterization of Prostate Tissue and Customized Polymeric Inks

The human prostate was collected immediately following radical prostatectomy. The tissue was cut into approximately 8 mm × 5 mm (diameter × height) cylindrical samples with flat surfaces via a surgical punch biopsy instrument with a circular hollow blade (8 mm diameter) for static and dynamic compression tests. The customized polymeric inks were 3D printed into cylindrical samples with similar dimensions as the tissue samples for comparison. Both static and dynamic compression tests were carried out using a mechanical analyzer (RSA-G2, TA Instruments). The static compression tests were conducted for up to 0.20 strain at a rate of 0.1 s⁻¹. The dynamic compression tests were conducted at frequencies of 0.1-20 Hz and at strains of 0.05, 0.10, and 0.20.

A.6. 3D Printing of Patient-Specific Prostate Model

The MRI image pack (1 mm resolution) of a patient's prostate was edited via Vitrea[®] software to form the corresponding STL model. The STL model was then sliced via Slic3r open source software to generate G-code for printing using a custom-built 3D printing system (AGS 1000, Aerotech) with two independent z-axis heads. After preparation of the customized polymeric ink with the required formulation, the ink (10 g) was mixed with 1% (w/v) red coloring agent (Procyinyl Red GS, ICI America Inc.) in dichloromethane (DCM) (0.5 mL) at 20:1 (w/v) ratio via the mixer at 2,000 rpm for 10 mins. DCM solvent was removed from the customized polymeric ink via vacuum before use. Trivial amount of the thickening agent was added in some of the trials, if the viscosity of the precursor needed to be elevated to achieve proper printability.

The customized polymeric ink and supporting ink (Loctite SI 595TM CL) were deposited from two dispensing apparatuses controlled by two high precision dispensers (Ultimus V, Nordson EFD) through nozzles with 610 μm inner diameter (20 GA GP.023X.25, Nordson EFD) and 500 μm layer height. The supporting ink was removed after the model was fully cured at ambient temperature in air.

A.7. 3D Registration for Investigating the Anatomical Fidelity

First, MRI imaging of the 3D printed prostate model was carried out using an MRI system (9.4 Tesla), while the model was placed in a 31 cm bore (Magnex Scientific). The field of view (FOV) was set to 5 mm \times 5 mm \times 5 mm. The number of scans and views were set to 200 and 128,000, respectively.

Next, a STL file of the printed prostate was obtained from the MRI image stack using the Mimics software package. 3D registration of the STL files between the 3D printed prostate model and the patient prostate model was achieved using CloudCompare open source software. CloudCompare was also used to obtain a distance map and a histogram of the distances of the corresponding points on the surface for the overlaid 3D models, using a comparison of 3×10^5 data points on the surface in 40 iterations. The arbitrary distance scale generated by CloudCompare was calibrated to mm scale and the root-mean-square (RMS) value for the histogram was obtained (0.45 mm). By comparing the RMS value of the calibrated distances with the highest dimension of the patient's prostate model (22.33 mm), the error in the printing process was obtained (0.02). The quantitative fidelity (98%) was calculated by deducting the error value in printing from 100%.

A.8. Endoscopy and Suturing Practices on the 3D Printed Prostate Model

The endoscopy system consisted of an endoscope (Gyrus ACMI), an LED light source (L9000, Stryker), an endoscopic camera (1288 HD 3-Chip, Stryker), an HD information management system (SDC Ultra, Stryker), a high flow insufflator (40L, Stryker) and an HDTV surgical display (WiSe™, Stryker). The endoscope was inserted into the urethra of the model and the endoscopic view was observed from the surgical display for the application. Suturing was conducted on the surface of the 3D printed prostate model with the aid of a surgeon and by utilizing a surgical needle for penetration and surgical thread (ETHICON 3-0 PERMA-HAND SILK) for suturing.

APPENDIX **B**

Supplementary Information for Chapter 3

B.1. Materials Preparation for 3D Printing

In order to prepare the ionic hydrogel ink, individual solutions of lithium chloride (Sigma-Aldrich) and acrylamide monomer (Sigma-Aldrich) in ultrapure water (Millipore) were prepared and combined along with the addition of ethylene glycol (Fisher Chemical). These components were magnetically stirred to obtain a homogeneous solution. At this point, polyacrylamide (Sigma-Aldrich) was added to the solution followed by an overnight magnetic stirring at 60 °C at 1200 rpm. Then, a solution of N, N'-methylenebisacrylamide (Sigma-Aldrich) in ultrapure water and Irgacure 1173 (BASF) was added to the composition and magnetically stirred for an additional 2 hours. The final ionic hydrogel ink was de-foamed using a planetary centrifugal mixer (Thinky ARE-310) at 2200 rpm prior to printing.

The dielectric layer ink for the DEA was prepared by mixing barium titanate nanoparticles (<100 nm-cubic, Sigma-Aldrich) in the Wacker SEMICOSIL® 912 base using a planetary centrifugal mixer (Thinky ARE-310) at 2000 rpm for 15 mins. Then, the silicone sealant (Loctite® 5039™ Nuva-Sil®) and the UV catalyst (Wacker ELASTOSIL® CAT UV) were added to the composition and mixed for an additional 10 minutes. Due to the relatively fast curing rate of this composition, this ink was printed immediately after preparation.

The composition of the DE used in fabrication of the sensing unit comprised of the silicone sealant (Loctite® 5039™ Nuva-Sil®) and the two-part silicone elastomer (Wacker SEMICOSIL® 912 as the base and ELASTOSIL® CAT UV as the catalyst with a 10:1 mixing ratio) at a 3:2 weight ratio

B.2. 3D Printing of DEAs

The 3D printing system comprised a 3-axis robotic dispenser (F5200, Fisnar) coupled with a pneumatic fluid dispensing system (Ultimus V, Nordson EFD) which allowed for adjustment of the deposition pressure. In addition, a camera unit was incorporated into the 3D printing system to facilitate the adjustment of the z-offset between the syringe tip and the printing substrate (glass slides, typically), as well as visualization of the printing process. A UV system (OmniCure Model S1500, Excelitas Technologies) with wavelength range of 320-500 nm was also mounted on the printer platform to enable the post-deposition crosslinking and curing of the ink materials. The synthesized individual material precursors were loaded into separate syringes, attached to the micro-nozzle tips (Nordson EFD), and mounted on the robotic gantry. The device fabrication involved the layer-by-layer deposition of the different material layers. The inner diameter of the dispensing tips, the printing pressure, and speed for each of the materials are summarized in Table B.1. In order to enhance the surface uniformity, the passive and dielectric layers were exposed to UV light ($\sim 75 \text{ mW/cm}^2$ and $\sim 65 \text{ mW/cm}^2$, respectively) after the complete deposition of individual layers of each of these materials. Prior to deposition of each hydrogel layer, the underlying silicone-based surface was treated with aliquots of 10 wt.% benzophenone (Sigma-Aldrich) solution in acetone ($\sim 80 \mu\text{l}$). After the absorption of benzophenone, the surface of silicone was dried using nitrogen gas and the subsequent hydrogel layer was printed while the entire structure was exposed to UV light ($\sim 5 \text{ mW/cm}^2$). In addition, the hydrogel electrodes were printed with 2 mm offset from each of the sides of the underlying layer to prevent the possibility of connection, and thus, shorting of the device. After

printing the bottom hydrogel layer and prior to printing the main dielectric elastomer (DE) layer, the offset between the sides of the hydrogel and the underlying passive layer was filled with the DE ink to facilitate the printing of the main DE layer. Finally, in order to enable the testing of the devices, copper tape was utilized as electric contact leads. The bottom contact lead was inserted during the printing process and prior to the deposition of the bottom hydrogel electrode, and the top contact lead was attached to the top hydrogel layer after printing the device using a small amount of silver paste to secure the attachment.

Table B.1. Printing parameters for different inks used in fabrication of DEAs.

| Material | Nozzle Inner Diameter | Pressure | Printing Speed |
|----------------|-----------------------|-----------------|----------------|
| Passive Layer | 330 μm | ~ 1.56 MPa | 5 mm/s |
| DE Layer | 410 μm | ~ 490 kPa | 4 mm/s |
| Ionic Hydrogel | 250 μm | ~ 33 kPa | 2 mm/s |

B.3. Materials Mechanical Characterization

Uniaxial tensile tests were performed on 3D printed rectangular specimens for each of the materials with approximate dimensions of $35 \times 5 \times 1$ mm³ (length \times width \times height, as printed) using TA Instruments RSA-G2 Extensional DMA Rheometer. The stress-strain curves were constructed for each material using three specimens at a rate of 0.5 mm/s.

B.4. Materials Rheological Characterization

Rheological characterization of material precursors (uncured state) were performed using a TA Instruments DHR-3 rotational rheometer. The hydrogel precursor was tested using a cone (40 mm, 2°) and plate geometry, while the silicone/BaTiO₃ precursor was tested using a parallel plate geometry (25 mm, 500 μm gap) due to its higher viscosity. Viscometry tests were performed from shear rates of 10^{-1} s⁻¹ to 10^3 s⁻¹, and oscillatory

rheometry tests were performed at a frequency of 1 Hz and oscillatory stresses of 10^{-1} Pa to 10^4 Pa.

B.5. Shear Rate Calculation During Extrusion

The shear rates experienced by the inks at the deposition nozzle walls during extrusion ($\dot{\gamma}$) can be estimated as follows (1):

$$\dot{\gamma} = \left(\frac{3n + 1}{4n}\right) \frac{8V}{D} \quad \text{Eq. 1}$$

where, n is the power-law index, which can be obtained by performing a power fit to the experimental data of viscosity (η) versus shear rate ($\dot{\gamma}$) ($\eta = K \dot{\gamma}^{n-1}$, with K denoting the flow consistency index). The calculated n values were 0.366 and 0.53 for the DE and ionic hydrogel inks, respectively. In addition, V and D represent the printing speed and the diameter of the deposition nozzle, respectively. Those values are listed in Table B.1 for each material system.

B.6. Materials Electrical Characterization

Dielectric characterization for silicone/BaTiO₃ was conducted using 3D printed circular samples with thicknesses of ~0.9 mm and diameters of 15 mm. An Agilent 16451B dielectric test fixture (electrode B, diameter=5 mm) coupled with an Agilent 4284A precision LCR meter were utilized to measure the dielectric constants of five samples. The obtained dielectric constant values were used in finite element method (FEM) and analytical models (Table B.2).

The resistance of hydrogel electrodes was measured using a Keithley 4200-SCS. The measurements were performed for five 3D printed rectangular specimens with effective

dimensions of $10 \times 5 \times 1 \text{ mm}^3$ (length \times width \times height). Copper leads were attached to the hydrogel samples using high purity silver paint to reduce contact resistance. Loading/unloading cycles for strains up to 100% were applied to the samples at a rate of 1.5 mm/min using a Deben microtensile tester and the change in resistance was monitored with changing strain. Specifically, a 2-point probe method was used to measure the electrical resistance via applying a current sweep (1-10 μA) and recording the voltage difference at every 10% strain increment.

B.7. DEA Testing

The setup used for applying high voltage to the DEAs comprised of an SMU (source measurement unit, Keithley 2450, Tektronix), a high voltage (HV) transformer (Q101-5, XP EMCO), and a voltage divider circuit (Figure B.1). The SMU provided the input voltage which was converted to the high voltage level required for actuating the device via the HV transformer. To achieve full-load configuration, the HV transformer was placed in series with a total of 200 M Ω resistors. This configuration produced an output voltage linearly proportional to the input, which improved the accuracy and controllability of the output voltage. In addition, the voltage divider circuit located at the output port of the setup enabled the attenuation and monitoring of the actuation voltage via a digital storage oscilloscope (TDS 2012C, Tektronix) and a digital multimeter (DMM) integrated in the setup ($V_{Read,DMM} \sim \frac{V_{HV}}{695.8}$).

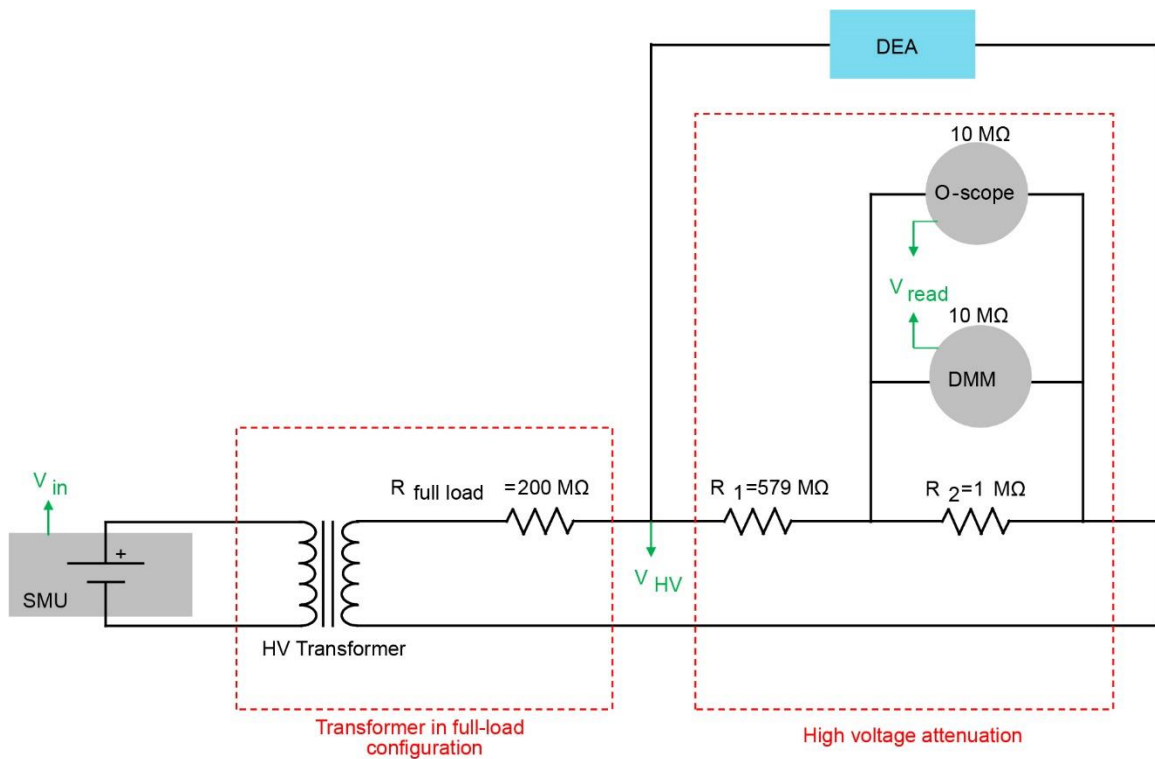


Figure B.1. Circuit setup for high voltage application and testing of DEAs.

B.8. DEA Actuation Video Analysis

During the DEA testing, the device actuation was recorded visually using a video camera (Nikon D750). The tip displacement of the device in each video was calculated using the “auto-tracker” tool in the Tracker video analysis and modeling software (<https://physlets.org/tracker>). For this purpose, a template and a key frame was created on the device tip at its initial position. The device tip was marked with a red color during experiments to facilitate this process. During the analysis, the auto-tracker tool scanned throughout the video frames for the best match to the selected template and yielded data on the changes in the position of the device tip over time. This data on the tip displacement versus time was then synced with separate recordings of the time stamps of the applied

voltage to obtain the device actuation performance in terms of tip displacement versus applied voltage.

B.9. Analytical Model for DEA

Materials model:

To account for the material nonlinearities, the stress-strain of each material was modeled using the Neo-Hookean (reduced polynomial) strain energy density (2):

$$S = C_{10}(I_1 - 3) = \frac{E_o}{6}(I_1 - 3) \quad \text{Eq. 2}$$

where, C_{10} is a constant correlated with the material elastic modulus at the initial stretch, E_o , obtained from the stress-strain experimental data. I_1 represents the first invariant of the right Cauchy-Green deformation tensor. The material response was assumed to be incompressible and isothermal, hence, $\lambda_1\lambda_2\lambda_3 = 1$, where λ_i denote the principle stretches in the 1-2-3 directions and can be expressed as follows for uniaxial deformation:

$$\lambda = \lambda_1 = \frac{l}{l_0}, \lambda_2 = \lambda_3 = \sqrt{\frac{l_0}{l}} \quad \text{Eq. 3}$$

where l_0 and l denote the initial length and the length at the stretched state, respectively.

Therefore, I_1 can be defined as:

$$I_1 = \lambda_1^2 + \lambda_2^2 + \lambda_3^2 = \lambda^2 + \frac{2}{\lambda} \quad \text{Eq. 4}$$

Substituting into the strain energy density yields:

$$S = C_{10}(\lambda^2 + 2\lambda^{-1} - 3) \quad \text{Eq. 5}$$

The uniaxial nominal stress can be obtained by differentiating S , with respect to λ , as follows:

$$\sigma = \frac{\partial S}{\partial \lambda} = 2C_{10}(\lambda - \lambda^{-2}) = \frac{E_o}{3}(\lambda - \lambda^{-2}) \quad \text{Eq. 6}$$

Stretch ratio can be related to the engineering strain using $\varepsilon = \lambda - 1$. Substituting this relationship into Eq. 6, the stress-strain correlation based on the Neo-Hookean material model can be obtained. Using $\sigma = E \varepsilon$, one can solve for the change in the elastic modulus as a function of the stretch:

$$E = \frac{E_o}{3} \frac{\lambda - \lambda^{-2}}{\lambda - 1} = 2C_{10} \frac{\lambda - \lambda^{-2}}{\lambda - 1} \quad \text{Eq. 7}$$

The experimental uniaxial tension test data was entered into Abaqus. The C_{10} values for the hydrogel, dielectric layer, and passive layer were then calculated using the Abaqus built-in least squares method to perform the Neo-Hookean material model fit of the experimental stress-strain data.

Kinematic development:

The device was modeled as a cantilever beam with a free length L (Figure B.2), which experienced a hyperelastic displacement of its centroid in response to an applied electrical field, and body and external forces. The device bending deflection with respect to the x and z axes from the base of the beam to point, s , and time, t , can be described in terms of an axial displacement along x -direction, $u(s, t)$, a transverse displacement along z -direction, $w(s, t)$, and a rotational angle, θ .

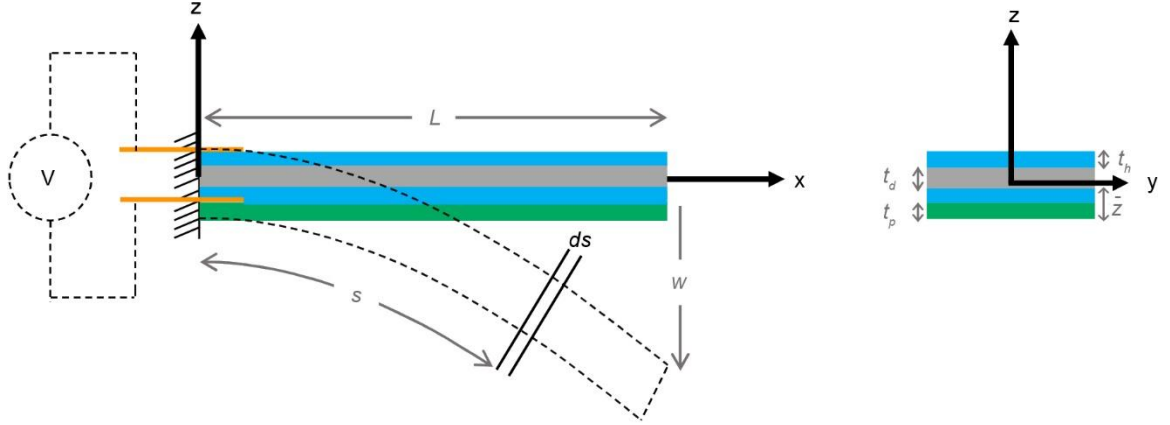


Figure B.2. General schematic of the beam-like device and notations used in the modeling (left), and cross section of the device (right) in which t_p , t_d , and t_h represent the thickness of passive, dielectric, and hydrogel electrode layers, respectively.

Performing a Taylor expansion up to cubic nonlinearities, the device kinematics can be expressed as follows:

$$u = -\frac{1}{2} \int_0^L w'^2 ds \quad \text{Eq. 8}$$

$$\theta \approx w' + \frac{1}{6} w'^3 \quad \text{Eq. 9}$$

$$u' \approx -\frac{1}{2} w'^2 \quad \text{Eq. 10}$$

The axial strain in the dielectric layer is ε_{11} :

$$\varepsilon_{11} = u' - z \kappa \quad \text{Eq. 11}$$

where z is the distance in the vertical direction from the neutral axis, \bar{z} . The normalized curvature due to bending is κ , which is defined as (3):

$$\kappa = \theta' = w'' + \frac{1}{2} w'' w'^2 \quad \text{Eq. 12}$$

The Rayleigh-Ritz method:

The Rayleigh-Ritz method was employed in which an assumed solution was directly substituted into the energy expressions. Mathematically, w can be expressed as a summation of functions from a complete, orthogonal, sufficiently differentiable function set. The advantage of this approach is that each function needs to satisfy only the kinematic boundary conditions. The approximate solutions were assumed in the form:

$$w(x) = q\psi(x) \quad \text{Eq. 13}$$

where the trial functions, ψ , are known independent comparison functions to denote the mode shapes (curvature due to deflection) of the beam and q represents the generalized coordinates.

Substantial numbers of adequate mode shape functions are available in the open literature. The following mode shape was selected for its generalized applicability to beam-like structures with various boundary conditions (4):

$$\psi(x) = A[\cos \beta x - \cosh \beta x + C(\sin \beta x - \sinh \beta x)] \quad \text{Eq. 14}$$

where,

$$C = \frac{\sin \beta L - \sinh \beta L + \beta L \bar{M}(\cos \beta L - \cosh \beta L)}{\cos \beta L + \cosh \beta L - \beta L \bar{M}(\sin \beta L - \sinh \beta L)}$$

The modal amplitude constant, A , and the applied external mass ratio, \bar{M} (if applicable), are the byproduct of normalizing the eigenfunction by the distributive mass of the device. The eigenvalue, β , is obtained numerically using MATLAB.

Constitutive modeling:

The constitutive relation for the entire DEA system was modeled similar to piezoelectric devices (5). Generally, the constitutive relation of a DEA can be expressed as follows (6):

$$\begin{bmatrix} \mathbf{D} \\ \boldsymbol{\epsilon} \end{bmatrix} = \begin{bmatrix} e^\sigma & d^d \\ d^c & s^{\mathbb{E}} \end{bmatrix} \begin{bmatrix} \mathbb{E} \\ \boldsymbol{\sigma} \end{bmatrix} \quad \text{Eq. 15}$$

where electric displacement, strain, applied electric field and stress vectors are denoted by vectors D , ϵ , \mathbb{E} , and σ , respectively. The dielectric layer material constants include the dielectric permittivity at a constant stress σ (e^σ), the electric displacement per unit stress at a given electric field (d^d), strain per unit electric field at a known stress (d^c), and the elastic compliance at a constant electric field \mathbb{E} ($s^{\mathbb{E}}$). It should be noted that d^c and d^d are numerically identical (6).

Using 1-axis and 2-axis notations to represent the planar directions (x-direction and y-direction, respectively), and the 3-axis to denote the direction along the thickness of the device (z-direction), the axial stress (σ_{11}) in the DE layer – which includes the contribution of the electromechanical strain (Λ) and axial strain (ϵ) – can be simplified as:

$$\sigma_{11} = E_{11}[\epsilon_{11} - \Lambda] \quad \text{Eq. 16}$$

where, E_{11} represents the elastic modulus of the DE layer (obtained from Eq. 7). The electromechanical strain, Λ , of the DE layer with thickness t_d in response to applied voltage V can be defined as (5, 7):

$$\Lambda = d_{31} \left(\frac{V}{t_d} \right) = \nu \frac{\epsilon_o \epsilon_r}{E_{11}} \left(\frac{V}{t_d} \right)^2 \quad \text{Eq. 17}$$

The Poisson ratio, vacuum permittivity, and relative dielectric permittivity are ν , ϵ_o , and ϵ_r , respectively.

Energy Method Mathematical Formulation:

The potential energy of the DEA with length L and cross section area A can be expressed as follows (7):

$$P = \frac{1}{2} \int_0^L \int_0^A E(z)(u' - z\kappa - \Lambda)^2 d\alpha ds \quad \text{Eq. 18}$$

$$P = \frac{1}{2} \int_0^L [\epsilon_o \quad \kappa] \begin{bmatrix} EA & EI_c \\ EI_c & EI_b \end{bmatrix} \begin{bmatrix} \epsilon_o \\ \kappa \end{bmatrix} ds - \int_0^L [F_\Lambda \quad M_\Lambda] \begin{bmatrix} \epsilon_o \\ \kappa \end{bmatrix} ds \quad \text{Eq. 19}$$

where, A , I_c , and I_b are the cross-section area, coupling inertia, and bending inertia of the device, respectively.

After expansion, the potential energy becomes:

$$\begin{aligned} P = & \frac{1}{2} \int_0^L EAu'^2 ds + \frac{1}{2} \int_0^L EI_b(w''^2 + w''^2 w'^2) ds + \frac{1}{2} \int_0^L EA\Lambda^2 ds \\ & + \int_0^L EI_c u' \left(w'' + \frac{1}{2} w'' w'^2 \right) ds - \int_0^L F_\Lambda u' ds \\ & - \int_0^L M_\Lambda \left(w'' + \frac{1}{2} w'' w'^2 \right) ds \end{aligned} \quad \text{Eq. 20}$$

where:

$$EA = \int_0^A E(z) d\alpha, EI_c = - \int_0^A E(z) z d\alpha, EI_b = \int_0^A E(z) z^2 d\alpha$$

$$F_\Lambda = \int_0^A E(z)\Lambda d\alpha, M_\Lambda = - \int_0^A E(z)\Lambda z d\alpha$$

After substituting the assumed solution:

$$\begin{aligned} P = & \frac{1}{2} \left(\int_0^L EA \psi_1'^2 ds \right) q_1^2 + \frac{1}{2} \left(\int_0^L EI_b \psi_2''^2 ds \right) q_2^2 + \frac{1}{2} \left(\int_0^L EI_b \psi_2''^2 \psi_2'^2 ds \right) q_2^4 \\ & + \frac{1}{2} \int_0^L EA \Lambda^2 ds + \left(\int_0^L EI_c \psi_1' \psi_2'' ds \right) q_1 q_2 \\ & + \frac{1}{2} \left(\int_0^L EI_c \psi_1' \psi_2'' \psi_2'^2 ds \right) q_1 q_2^3 - \left(\int_0^L F_\Lambda \psi_1' ds \right) q_1 \\ & - \left(\int_0^L M_\Lambda \psi_2'' ds \right) q_2 - \frac{1}{2} \left(\int_0^L M_\Lambda \psi_2'' \psi_2'^2 ds \right) q_2^3 \end{aligned} \quad \text{Eq. 21}$$

The Euler-Lagrangian method was then applied to the Lagrangian, $L = T - P$, as follows:

$$\frac{\partial}{\partial t} \left(\frac{\partial L}{\partial \dot{q}_i} \right) - \frac{\partial L}{\partial q_i} = Q \quad \text{Eq. 22}$$

For a static condition and after substituting P into the above formulation, the Euler-Lagrangian equation becomes:

$$k_{le} q_1 + k_{lc} q_2 + k_{nc} q_2^3 = Q_{1,int} + Q_{1,ext} \quad \text{Eq. 23}$$

$$k_{lc} q_1 + k_{lb} q_2 + 3k_{nc} q_1 q_2^2 + k_{nb} q_2^3 - k_{n\Lambda} q_2^2 = Q_{2,int} + Q_{i,ext} \quad \text{Eq. 24}$$

where:

$$k_{le} = EA \int_0^L \psi_1'^2 ds, k_{lb} = EI_b \int_0^L \psi_2''^2 ds, k_{lc} = EI_c \int_0^L \psi_1' \psi_2'' ds$$

$$k_{n\Lambda} = \frac{3}{2} M_\Lambda \int_0^L \psi_2'' \psi_2'^2 ds, k_{nb} = 2EI_b \int_0^L \psi_2''^2 \psi_2'^2 ds, k_{nc} = \frac{1}{2} EI_c \int_0^L \psi_1' \psi_2'' \psi_2'^2 ds$$

$$Q_{1,int} = F_{\Lambda} \int_0^L \psi_1' ds, Q_{2,int} = M_{\Lambda} \int_0^L \psi_2'' ds$$

where k_{le} , k_{lb} , and k_{lc} represent the linear kinematic stiffness coefficient due to extension, bending, and electromechanical coupling, respectively. $k_{n\Lambda}$, k_{nb} , and k_{nc} denote the nonlinear coefficients due to electrical straining, kinematic bending stiffness, and electromechanical coupling, respectively. The generalized internal, Q_{int} , and external, Q_{ext} , forces are due to the electrical potential and external load, respectively. Since k_{lc} and k_{nc} are numerically negligible, the governing equations become:

$$k_{le}q_1 = Q_{1,int} \tag{Eq. 25}$$

$$k_{lb}q_2 + k_{nb}q_2^3 - k_{n\Lambda}q_2^2 = Q_{2,int} + Q_{i,ext} \tag{Eq. 26}$$

The blocking force is (7):

$$F_{bl} = \Lambda EA \tag{Eq. 27}$$

B.10. Finite Element Method (FEM) for Characterization of DEA Performance

A two-dimensional FEM model of the DEA was developed using Abaqus. The material parameters were extracted from the stress-strain test data using the Abaqus built-in strain energy potential function for the hydrogel and passive layers. The Neo-Hookean model appeared to provide a reasonable fit to the uniaxial stress-strain data with an assumed Poisson ratio for the volumetric response of 0.5. Since Abaqus does not provide constitutive models for hyperelastic dielectric materials, we used the Abaqus isotropic elastic model for piezoelectric materials to model the DE layer, but both d_{31} and E for each electric potential increment were updated based on the interpolations from the stress-strain

data for the DE along with values obtained from the analytical model with the compensation factor that closely matched the experimental results. A Poisson ratio of 0.495 was used for the DE material based on the allowable Poisson ratio in the Abaqus code for the dielectric layer (8). The hydrogel electrodes and passive layer were meshed using 8-node, biquadratic, hybrid plane strain elements with reduced integration (CPE8RH). The dielectric layer was meshed using 8-node, biquadratic, piezoelectric plane strain elements with reduced integration (CPE8RE). Perfect bonding between the layers was assumed; thus, surface-based tie constraints at the interfaces were implemented. The electrical potentials for the layers were coupled to the electrical potentials of the nodes of the supporting structure using linear constraint equations.

The electrical boundary conditions were imposed to the top and the bottom of the dielectric layer, where the bottom electrical voltage was set equal to zero, signifying electrical grounding. The experimental measurements of the voltage input to actuate the device were applied to the top electrical boundary condition. Fixed boundary conditions were applied to the nodes located in the end of the passive layer (7 mm) to emulate the device attachment to the rigid glass substrate during the experiments. Finally, experimental cases with an applied tip mass to the DEA were simulated by adding the effect of gravity and a concentrated force at the tip of the device - with a value corresponding to the applied mass - to the FEM. The remainder of the device parameters used for FEM and analytical model are listed in Table B.2.

Table B.2. FEM and analytical model parameters used in modeling DEA performance.

| Parameter Description | Value |
|---|------------------------|
| Passive layer-Total length | 30 mm |
| Passive layer-Free length | 23 mm |
| Passive layer-Width | 10 mm |
| Passive layer-Thickness | 313 μm |
| Passive layer-Density | 998 kg/m^3 |
| Passive layer-Poisson ratio | 0.5 |
| Passive layer- C_{10} (Neo-Hookean model coefficient) | 62114.34 |
| Hydrogel electrodes-Total length | 26 mm |
| Hydrogel electrodes-Free length | 21 mm |
| Hydrogel electrodes-Width | 6 mm |
| Hydrogel electrode#1-Thickness | 458 μm |
| Hydrogel electrode#2-Thickness | 304 μm |
| Hydrogel electrodes-Density | 1197.5 kg/m^3 |
| Hydrogel electrodes-Poisson Ratio | 0.5 |
| Hydrogel electrodes- C_{10} (Neo-Hookean model coefficient) | 1721.81 |
| DE layer-Total length | 30 mm |
| DE layer-Free length | 23 mm |
| DE layer-Width | 10 mm |
| DE layer-Thickness | 516 μm |
| DE layer-Density | 1127.7 kg/m^3 |
| DE layer-Poisson ratio | 0.495 |
| DE layer- C_{10} (Neo-Hookean model coefficient) | 14041.79 |
| DE layer-Relative Permittivity | 4.16 |
| Device mass | 0.626 g |

References

1. Q.-H. Nguyen, N.-D. Nguyen, Incompressible Non-Newtonian Fluid Flows, in *Continuum Mechanics-Progress in Fundamentals and Engineering Applications*. (InTech, 2012).
2. D. Nicholson, N. Nelson, B. Lin, A. Farinella, Finite Element Analysis of Hyperelastic Components. *Applied Mechanics Reviews* **51**, 301-320 (1998).
3. A. Nayfeh, P. Pai, *Linear and Nonlinear Structural Mechanics*. (Jon Wiley & Sons, 2004).

4. E. Habtour, D. P. Cole, S. C. Stanton, R. Sridharan, A. Dasgupta, Damage Precursor Detection for Structures Subjected to Rotational Base Vibration. *International Journal of Non-Linear Mechanics* **82**, 49-58 (2016).
5. K. Kadooka, H. Imamura, M. Taya, Experimentally Verified Model of Viscoelastic Behavior of Multilayer Unimorph Dielectric Elastomer Actuators. *Smart Materials and Structures* **25**, 105028 (2016).
6. J. Sirohi, I. Chopra, Fundamental Understanding of Piezoelectric Strain Sensors. *Journal of Intelligent Material Systems and Structures* **11**, 246-257 (2000).
7. I. Chopra, J. Sirohi, *Smart Structures Theory*. (Cambridge University Press, 2013), vol. 35.
8. Abaqus User Manual, Abaqus Theory Guide. Version 6.14. USA.: *Dassault Systemes Simulia Corp*, (2014).

APPENDIX C

Supplementary Information for Chapter 4

C.1. 3D Printing Materials Formulation and Preparation

The material system mainly consisted of the previously discussed silicone sealant (RTV sealant, Loctite SI 595 CL) and silicone grease (LP20, Trident) with desired ratios to replicate the properties of tissue of interest. Coloring agent (Procyinyl Red GS, ICI America Inc.) was optionally added into the material system for the purpose of indicating different model sections and/or the prosthetic valve target implantation depth mark. For adding the coloring agent to the material, the customized polymeric ink (10g) was mixed with 1 % (w/v) coloring agent in dichloromethane (DCM) solution (0.5 mL) at a 20:1 w/v ratio via the mixer at 2000 rpm for 6 minutes. For printing the calcified regions, Alex Plus Spackling material (DAP Products, Inc.) was used. In addition, during the printing process, a sacrificial ink was utilized to construct the supporting structures, which comprised the surfactant Pluronic® 127 (Sigma) dissolved in glycerol/DI water solution (1:9 v/v) at a ratio of 40:100 (w/v). After printing and curing of the model, the supporting structure was removed by flushing with cold water.

C.2. Preparation and Characterization of Tissue and Polymer Samples

The human tissue specimens were obtained from both the myocardium and aortic wall regions. The tissue samples for compression tests were cut using a laser cutter (Epilog Helix 24, Epilog Laser) into cylindrical samples. Specifically, the aortic and myocardium tissue specimens had dimensions of ca. 7.1-7.2 mm × 1.5-2.4 mm (diameter × height) and ca. 6.6-6.7 mm × 2.2-3.5 mm (diameter × height), respectively. The samples were mounted on a mechanical analyzer (RSA-G2, TA Instruments) for compression tests using an 8 mm parallel plate geometry at constant linear rates of 0.0355 s⁻¹. It should be noted that a set of

human tissue specimens from a calcified aorta were received as rectangular samples and were tested in tension to obtain the range of modulus for this specific case (Aorta tissue 2 and its corresponding ink 4).

For compression test of the polymeric materials, different formulations were printed into cylindrical samples with dimensions of ca. 8 mm × 5 mm (diameter × height). The tests were carried out using a mechanical analyzer (RSA-G2, TA Instruments) using an 8 mm parallel plate geometry. The test procedure and settings were the same as the tissue characterization for comparison purposes. A summary of the range of elastic moduli obtained at different strains for example specimens of the tissue and polymers is provided in Table C.1.

Table C.1. Estimated elastic modulus of examples of tissue and custom-formulated polymer samples at different strains and comparison with the reported values in literature (ϵ : strain, B/A: weight ratio of bulking agent to active agent in the composition).

| Sample Type | Young's Modulus at $\epsilon < 0.03$ (kPa) | Tangent Modulus at $\epsilon \sim 0.10$ (kPa) | Tangent Modulus at $\epsilon \sim 0.30$ (kPa) | Reported Modulus Values in Literature (kPa) |
|-------------------------|--|---|---|---|
| Human myocardium tissue | 36-146 | 54-267 | 168-732 | 12-273 |
| Human aortic tissue | 56-216 | 112-1,077 | 533-1,097 | 334-1,817 |
| Ink 1 (B/A=1.15) | 113.4 ± 3.7 | 99.1 ± 3.8 | 162.7 ± 17.5 | |
| Ink 2 (B/A=0.85) | 165.8 ± 8.5 | 194.7 ± 20.8 | 213.3 ± 19.0 | |
| Ink 3 (B/A=0.7) | 250.6 ± 9.1 | 260.1 ± 25.4 | 284.0 ± 5.1 | |
| Ink 4 (B/A=0.25) | 455.6 ± 22.5 | 712.7 ± 13.9 | 679.2 ± 24.8 | |

C.3. Fourier Transform Infrared Spectroscopy (FTIR)

Chemical analysis of the spackling material was carried out using an FTIR spectrophotometer (Thermofisher Nicolett iS50) in attenuated total reflection (ATR) mode. Spectra, averaged over 32 scans, were taken in the range of 4,000–400 cm^{-1} wavenumber at a resolution of 4 cm^{-1} .

C.4. Processing of STL Models

The aortic root stereolithographic (STL) models from two patient cases, derived from corresponding CT images, were received from Medtronic Inc. Each STL model consists of aortic wall, myocardium, leaflets and calcified regions. In order to 3D print a part, the STL models were sliced into horizontal layers and converted into G-code, the computer language that dictated the printing pathways as the input for 3D printing process. MeshLab, an open source mesh editing software, was used to divide each STL model into separate components (myocardium, aortic wall, leaflets, and calcifications) to facilitate the assignment of different inks and their corresponding settings for the printing process. Slic3r, an open source slicing software, was used for slicing the models into layers and G-code generation. We imported the full aortic root model into Slic3r, as well as the separate component STL files as modifiers. These modifiers allowed us to assign different inks, print speeds, perimeters, and other printing parameters for specific regions of a given model. When the model was fully configured for printing, Slic3r was used to generate the G-code. Finally, we used a custom MATLAB script to convert the G-code generated from Slic3r into a form compatible with our custom-built 3D printing system for multi-nozzle printing.

C.5. 3D Printing of Aortic Root Models

A custom-built 3D printing system (AGS 1000, Aerotech) with two independent z-axis heads was used for 3D printing of aortic root models. Four inks with different properties, including the ink for aortic wall, the ink for myocardium and leaflets, the ink for calcified region, and the ink for supporting material were utilized in the process and were deposited from four dispensing apparatuses controlled by four high precision dispensers (Ultimus V, Nordson EFD). For fabricating the models used for fidelity analyses and hemodynamic studies, the myocardium section and its corresponding support structure were printed using nozzles with inner diameter of 1.36 mm (15GA GP .054X.25, Nordson EFD) and layer height of 1.2 mm, and the leaflets, aortic wall, calcification and their corresponding supporting structure were printed using nozzles with inner diameter of 0.84 mm (18 GA GP .033X.25, Nordson EFD) and layer height of 0.7 mm. For these cases, the printing speeds for perimeter and infill of the models were set to 20 mm/s and 10 mm/s, respectively. For fabricating the models with integrated sensor, finer nozzles (inner diameter of 0.51 mm, 21 GA GP .020X.25, Nordson EFD) and layer height (0.4 mm) were used for the lower section of the model (myocardium and aortic root including the sinuses, leaflets, and calcification) in order to 3D print the sensor array with a higher resolution. The top part of these models (ascending aorta) were printed using nozzles with inner diameter of 1.36 mm and layer height of 1.2 mm. The printing speed for perimeter and infill of these models were set to 10 mm/s and 8 mm/s, respectively. After printing, the models were left in ambient air for 5-7 days to ensure the complete curing. Once the models were fully cured, the supporting structure was removed via flushing with cold water. For

the purpose of this study, two cases of patient-specific aortic root models were printed, with one being used for fidelity analysis demonstration and one for hemodynamic studies and sensor integration.

C.6. Model Fidelity Analysis

In order to assess the fidelity of the 3D printed structure to the original patient's anatomy, a CT scan was performed on the 3D printed aortic root model. The obtained CT image stack was then segmented and reconstructed to obtain a 3D aortic root model with a stereolithography (STL) format using Mimics software package (Materialize NV). 3D registration of the STL files between the 3D printed aortic root model and the patient aortic root geometry was achieved using CloudCompare® 2.10.2 (www.cloudcompare.org) open source software. CloudCompare was also used to overlay the two 3D models and obtain a distance map along with a histogram of the offset between the patient anatomy as the template, and the 3D printed construct for 3×10^5 voxels in 40 iterations. After registration, the two models were compared using the “cloud to mesh” tool in CloudCompare. The process generated a distance map and a histogram of the distance difference between the points of the 3D printed model and the patient's native aortic root anatomy. The distance scale in CloudCompare was then calibrated to mm. From the histogram of the distances, the print fidelity was determined by the percentile of points that fell between a given error margin.

C.7. Frame Analysis of the Implanted Valve in the 3D Printed Aortic Root Model

A 26 mm Evolut™ PRO valve (Medtronic) was implanted into the 3D printed aortic root model using the EnVeo™ PRO delivery system (Medtronic). The model was also

mounted in a fixture for mimicking the confinement and the surrounding structure of the aortic root in patient's real anatomy (Figure C.1). After performing the CT scans, the aortic root and valve frame were computationally modeled and reconstructed using the Mimics medical image processing software (Materialize NV). A total of 9 frame node marks (representing each frame level of the valve) were marked on the reconstructed aortic model with implanted valve for the purpose of frame deformation analysis and comparison to the corresponding values from patient's postoperative data (Figure C.1).

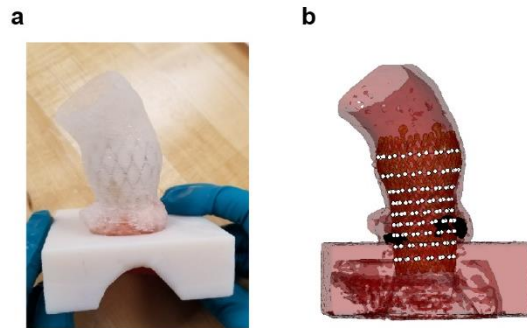


Figure C.1. Implantation of the prosthetic valve in the 3D printed aortic root model. (a) Implanted valve in the 3D printed aortic root model mounted in the fixture. (b) Corresponding scan of the 3D printed model constructed from CT imaging and the marked 9 node levels used for frame analysis.

C.8. Calculation of Parameters for *In Vitro* Hemodynamic Testing

The values of pulse pressure were calculated by subtracting the average systolic aortic pressure and the average diastolic aortic pressure over ten consecutive cycles. The data points and the error bars in the plot correspond to the average and standard deviation of three tested models for each case, respectively. The estimated values of overall compliance correspond to the slope of the linear fit for each case.

The peak-to-peak pressure gradient values were calculated by averaging the difference between the maximum ventricular pressure and the maximum aortic pressure in systole over ten consecutive cycles. If applicable, the readings for left ventricular pressure were

adjusted based on the calibration baseline of the corresponding balloon pressure catheter. The negative values of left ventricular pressure at the beginning of diastole corresponds to the instant when the pulsatile pump stops and most of the fluid is pushed out through the leaflets and into the aorta. At this moment, there is less fluid pressure in the left ventricular, thus the pressure reading in LV is negative.

For the paravalvular leak study, a 26 mm Medtronic Evolut™ R valve was implanted in the model with calcified leaflets. Transthoracic echocardiograms of the 3D printed aortic root model with implanted valve for detection of paravalvular leak sites were obtained from a long-axis view via an ultrasound system (Model iE33, Philips) using a X7-2 pediatric probe.

C.9. Preparation of Models with Internally Integrated Sensor Array

The ionic hydrogel precursor used to create the electrodes of the sensor consisted of acrylamide monomer (A8887, Sigma) dissolved in an 8 M lithium chloride solution (L7026, Sigma) with ratio of 15.64:100 (w:v), as well as N,N'-methylenebisacrylamide crosslinking agent (M7279, Sigma) and 2-hydroxy-2-methyl-propiophenone photoinitiator (405655, Sigma) with ratios of 0.00064:1 and 0.00543:1 with respect to the weight of acrylamide monomer, respectively. For better visualization of the ionic hydrogel in the channels, orange and green dyes were added to the precursor solution (0.5 % v/v). Once the 3D printed models were fully cured, the ionic hydrogel precursor was injected into the channels via a 30 G needle (305128, BD) and was photopolymerized via exposure to a UV system (Omniculture S1500, Excelitas Technologies). For testing purposes and connection of

sensor array to the measurement system, flexible 28 AWG stranded tinned copper wires (BNTECHGO) were inserted into the filled channels of the models.

C.10. Calibration of the Sensor Array

In order to be able to translate the capacitance changes of the sensing elements to pressure values, the sensor arrays were calibrated. For this purpose, the region of the model limited to the 3×3 sensor array was fabricated separately. The calibration was performed by applying different pressures to each of the nine sensing elements in the array and measuring the changes in their capacitance individually. The sensor array was fixed on a silicone-based platform (MoldStar 15, SmoothOn) and was mounted on a digital scale (Elec3) in order to record the values of applied forces during calibration. A custom 3D printed bar (tough resin, Formlabs 2) with a rectangular tip with dimensions of $2 \text{ mm} \times 2 \text{ mm}$ (approximately corresponding to the area of sensing elements) was mounted on a vertical axis of a nanopositioning stage (ANT130-LZS, Aerotech) to apply a press-release cycle to each sensing element of the device. By varying the vertical position of the bar during the calibration process, different values of the applied forces were obtained. The applied pressure values were calculated by dividing the recorded forces by the area of sensing elements before deformation. In addition, the sensor was connected to a characterization system (B1500A, Agilent Technologies) to record the changes in device capacitance at each of the press-release cycles. The recorded measurements were analyzed to obtain plots of $\frac{\Delta C}{C_0}$ versus applied pressure, yielding two linear regions for each of the sensing elements based on the range of $\frac{\Delta C}{C_0}$. To translate the capacitance changes to

pressures values, the calibration equation corresponding to appropriate $\frac{\Delta C}{C_0}$ range of each sensing element in the array was used (Table C.2).

Table C.2. Calibration equations for the 9 sensing elements of the sensor array.

| Sensing Element (row, column) | $\frac{\Delta C}{C_0}$ Range | Calibration Equation |
|----------------------------------|----------------------------------|---|
| Element 11 | $\frac{\Delta C}{C_0} \leq 0.35$ | $P = \left(\frac{\Delta C}{C_0}\right) / 0.0011$ |
| | $\frac{\Delta C}{C_0} > 0.35$ | $P = \left(\frac{\Delta C}{C_0} + 0.5222\right) / 0.0032$ |
| Element 12 | $\frac{\Delta C}{C_0} \leq 0.14$ | $P = \left(\frac{\Delta C}{C_0}\right) / 0.0009$ |
| | $\frac{\Delta C}{C_0} > 0.14$ | $P = \left(\frac{\Delta C}{C_0} + 0.3407\right) / 0.0029$ |
| Element 13 | $\frac{\Delta C}{C_0} \leq 0.45$ | $P = \left(\frac{\Delta C}{C_0}\right) / 0.0008$ |
| | $\frac{\Delta C}{C_0} > 0.45$ | $P = \left(\frac{\Delta C}{C_0} + 0.5656\right) / 0.0021$ |
| Element 21 | $\frac{\Delta C}{C_0} \leq 0.17$ | $P = \left(\frac{\Delta C}{C_0}\right) / 0.0011$ |
| | $\frac{\Delta C}{C_0} > 0.17$ | $P = \left(\frac{\Delta C}{C_0} + 0.9813\right) / 0.006$ |
| Element 22 | $\frac{\Delta C}{C_0} \leq 0.2$ | $P = \left(\frac{\Delta C}{C_0}\right) / 0.0009$ |
| | $\frac{\Delta C}{C_0} > 0.2$ | $P = \left(\frac{\Delta C}{C_0} + 0.4778\right) / 0.0032$ |
| Element 23 | $\frac{\Delta C}{C_0} \leq 0.4$ | $P = \left(\frac{\Delta C}{C_0}\right) / 0.0008$ |
| | $\frac{\Delta C}{C_0} > 0.4$ | $P = \left(\frac{\Delta C}{C_0} + 0.1276\right) / 0.0013$ |
| Element 31 | $\frac{\Delta C}{C_0} \leq 0.07$ | $P = \left(\frac{\Delta C}{C_0}\right) / 0.0004$ |
| | $\frac{\Delta C}{C_0} > 0.07$ | $P = \left(\frac{\Delta C}{C_0} + 0.3474\right) / 0.002$ |
| Element 32 | $\frac{\Delta C}{C_0} \leq 0.45$ | $P = \left(\frac{\Delta C}{C_0}\right) / 0.0009$ |
| | $\frac{\Delta C}{C_0} > 0.45$ | $P = \left(\frac{\Delta C}{C_0} + 0.5949\right) / 0.0024$ |

| | | |
|------------|----------------------------------|---|
| Element 33 | $\frac{\Delta C}{C_0} \leq 0.11$ | $P = \left(\frac{\Delta C}{C_0}\right) / 0.0007$ |
| | $\frac{\Delta C}{C_0} > 0.11$ | $P = \left(\frac{\Delta C}{C_0} + 0.4501\right) / 0.0031$ |

C.11. Testing of Models with Internally Integrated Sensor Array

The 3D printed aortic root models were placed in a custom silicone-based fixture (Mold Star 15, SmoothOn) and were connected to a characterization system (B1500A, Agilent Technologies) to measure the capacitance values. For each case of valve sizing and implantation height, first, the baseline capacitance of the nine sensing elements in the sensor array were recorded (C_0). Then, the prosthetic valve was implanted in the model, followed by measuring the new values of capacitance with the implanted valve (C_i). Finally, the change in capacitance values for the 9 sensing elements were calculated ($\Delta C = C_i - C_0$). The prosthetic valves used in the tests were Medtronic Evolut™ R 26mm, Evolut™ R 29 mm valve and stent frame, and CoreValve™ 31mm. The normalized capacitance changes $\left(\frac{\Delta C}{C_0}\right)$ of the 9 sensing elements for each case of valve sizing and implantation height were then processed using MATLAB to obtain the heatmaps (Figure C.2). The continuous heatmaps were obtained by interpolation and halving the intervals 5 times in each dimension. To translate the capacitance changes to pressures values, the calibration equations corresponding to each sensing element in the array and the $\frac{\Delta C}{C_0}$ range was used (Table C.2).

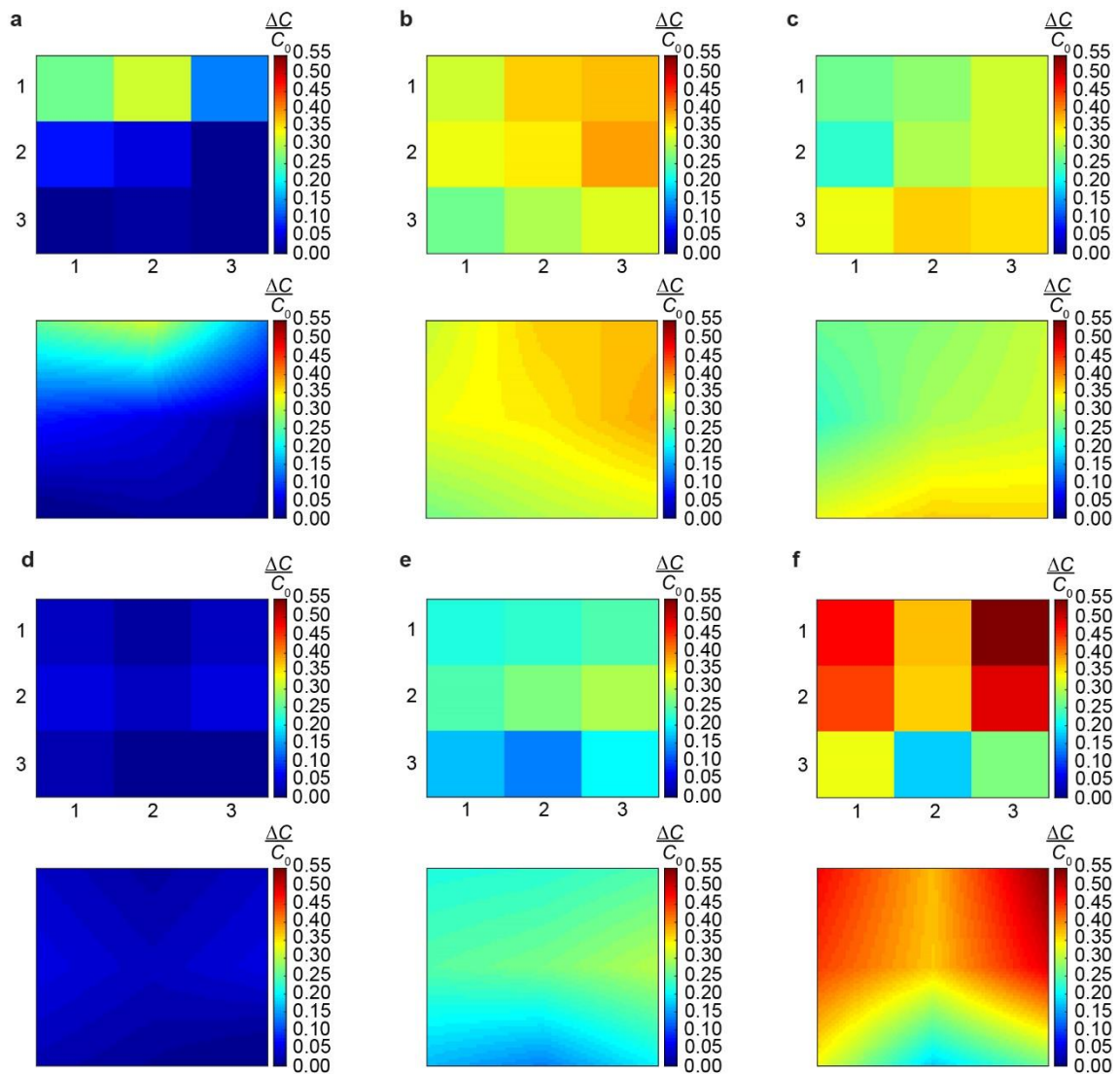


Figure C.2. Heatmaps of normalized capacitance changes for different cases of valve implantation height and sizing. (a) Implantation of the 29 mm Evolut™ R TAVR valve frame at a shallow height. (b) Implantation of the 29 mm Evolut™ R TAVR valve frame at an intermediate height. (c) Implantation of the 29 mm Evolut™ R TAVR valve frame at a deep height. (d) Implantation of the 26 mm Evolut™ R TAVR valve at an intermediate height. (e) Implantation of the 29 mm Evolut™ R TAVR valve at an intermediate height. (f) Implantation of the 31 mm CoreValve™ TAVR valve at an intermediate height. Top plots in each panel represent the 3×3 discrete heatmap for each case; Bottom plots in each panel represent the continuous heatmaps resulted from interpolation and halving the intervals 5 times in each dimension.